Phase diagram for the co-adsorption of O and OH on Pt(100) and Pt(111) as determined by DFT

Thesis submitted for the degree of Master of Science in Engineering in Chemical Engineering

By

Pierre Louis Cilliers
BSc Chemical Engineering (UCT)

Supervisors:

Professor Eric van Steen

Dr Melissa Petersen

September 2017

Centre for Catalysis Research
Department of Chemical Engineering
University of Cape Town
South Africa

DECLARATION

"I know the meaning of plagiarism and declare that all the work in the document, save for that which is properly acknowledged, is my own. This thesis/dissertation has been submitted to the Turnitin module (or equivalent similarity and originality checking software) and I confirm that my supervisor has seen my report and any concerns revealed by such have been resolved with my supervisor."

Signed by candidate

Pierre L. Cilliers

2017/09/28

SYNOPSIS

Methanol is a versatile chemical component which can be used both as a reactant and a high density liquid fuel. Methanol is typically produced in a two-step, thermodynamically demoted, process via synthesis gas. Production of methanol may also be achieved via a low temperature direct methane to methanol conversion. To limit side reactions, it has been postulated that the surface of the catalyst must be saturated. This prompts more research into Pt catalyst surface coverages as a function of reaction conditions. However, O has an observed saturation coverage of 0.50 ML on Pt(111). To overcome this co-adsorption with OH was proposed as a means to reach full coverage. Therefore, this research focused on the obtainable coverages of O and OH on Pt(111) and Pt(100).

To determine the coverages obtainable on Pt(111) and Pt(100), a DFT study was performed utilizing VASP with a GGA-PAW-PBE model using a p(2x2) unit cell. The optimized bulk unit cell resulted in a Pt lattice parameter of 3.976 Å. A 5 layered slab with the top two layers relaxed and a 10 Å vacuum was used. Utilizing this model the preferred adsorption sites for O and OH were found which pertain to a fcc hollow site for O and atop site for OH on Pt(111) and bridge sites for both O and OH on Pt(100). Using these preferred adsorption sites all possible adsorption configurations on Pt(111) and Pt(100) on a p(2x2) cell were tested.

In addition to the preferred sites and adsorption configurations the contributions from translation were investigated for the surface adsorbates prior to the generation of the adsorbate phase diagrams. It was found that, when considering O and OH, adsorbates can be treated as a 2D lattice gas attributing no translation contribution below 400 °C.

Modelling the adsorbates as a 2D lattice gas, the phase diagrams for Pt(111) and Pt(100) where constructed by finding the lowest adsorption energy for an adsorbate configurations at various chemical potentials of O_2 and H_2O. On Pt(111) single adsorbate coverages were preferred with full coverage of OH attainable at O_2 and H_2O chemical potentials of -0.22 eV and -0.60 eV. In contrast, the Pt(100) surface has several co-adsorption coverages available including full coverage with 2O/2OH at the same chemical potentials.

The phase diagrams were then regenerated for dispersion considerations using the PAW-optB88 model. This model was selected over PAW-optPBE due to the increased accuracy when predicting OH adsorption on Pt, which is dominant at higher chemical potentials which can yield 1.00 ML. The dispersion model did not alter which adsorbate configurations yielded the lowest adsorption energies and primarily shifted the conditions required to generate each phase to lower chemical potentials of O_2 and H_2O when compared to PAW-PBE. It should be realized though that the PAW-optB88 model over-predicts the adsorption energy of O and therefore any phase containing purely O adsorbates species should be better approximated by the PAW-PBE phase diagrams.

The results obtained are supportive of a direct methane to methanol synthesis as full coverage could be attainable with 2O/2OH providing an adsorbed O present on Pt(100). To further this research, the adsorption geometries on the surface should be experimentally tested at a chemical potential range of -0.22 eV to -0.80 eV of both O_2 and H_2O. Following this, synthesis research into promoting Pt(100) surface growth could prove beneficial as the reaction would tend to proceed on this surface when considering low temperature (80 – 200 °C) direct methane to methanol synthesis.

ACKNOWLEDGEMENTS

I would like to acknowledge the following individuals and institutions without who this research would not have been possible.

First and foremost, Professor Eric van Steen, your supervision and guidance throughout this study is evident in the quality and quantity of this work. Whether it was chemical potential or the endless discussions regarding the van der Waals detour you continue to both educate and inspire me to achieve. You have remained patient and taken the time to mentor me, time which I often take utilizing your open door policy, perhaps too often. The confidence and mental growth you have instilled in me will last a lifetime and for that I am truly thankful. I entered this research with an interest in research but you have cultivated it into a passion for it.

Dr Melissa Petersen, your knowledge of computational chemistry I have found to be invaluable during this research. Be it self-made nanoparticle diagrams created from magnets or your input when creating the visualization scripts, I can safely say that without your input this research would have taken many more years to interpret. Your guidance and open door policy allowed for great strides in this research. Thank you for all the time you spent answering each and every question in depth, if it weren't for your knowledge I may never have found my missing electron.

To Thobani Gambu, one day I will stop talking about modelling van der Waals in DFT, but when that day comes I suspect the echoes of our conversations will still be bouncing off the walls. You were the first step in my education into computational modelling and continued to educate me over the years. From dispersion functions to solvation energies your passion for research inspired me to continue to rise to the occasion. Thank you for the time you took to answer my questions and support my research while including me in yours.

This research would also not have been possible without the resources and computational facilities given by the University of Cape Town and the Centre for High Performance Computing (CHPC). Nor would this research have been possible without the financial support of the National Research Foundation (NRF) and Sasol. In particular, to the extended Sasol bursary that has seen me through both undergraduate and postgraduate studies.

Finally, to all my friends and family that supported me through this time, you each have influenced the quality of this work. It is no understatement to say that without your support I would not have managed to finish in the time I did.

TABLE OF CONTENTS

LIST OF FIGURES

LIST OF TABLES

LIST OF ABBREVIATIONS

DFT	: Density Functional Theory
DMC	: Dimethyl Carbonate
DMFCs	: Direct Methanol Fuel Cells
EELS	: Electron energy-loss spectroscopy
GGA	: Generalized Gradient Approximation
GS	: Ground State
HFSCF	: Hartree-Fock Self-Consistent Field
LDA	: Local Density Approximations
LEC	: Lowest Energy Configuration
LEED	: Low Energy Electron Diffraction
MAD	: Mean absolute deviation
MAE	: Mean absolute error
ML	: Monolayer
MOR	: Mordenite Framework
MMA	: Methyl Methacrylate
MSE	: Mean signed error
MTBE	: Methyl Tertiary Butyl Ether
optB88	: Optimized B88 model
optPBE	: Optimized Perdew, Burke and Ernzerhof
PAW	: Projected Augmented Wave
PBE	: Perdew, Burke and Ernzerhof
PES	: Potential Energy Surface
PW91	: Perdew-Wang Functional 1991
RMSE	: Root mean squared error
RPBE	: Revised Perdew, Burke and Ernzerhof
SCF	: Self-consistent field
STM	: Scanning Tunnelling Microscopy
TISE	: Time-Independent Schrödinger Equation
VASP	: Vienna *Ab Initio* Simulation Package
ZSM-5	: Zeolite Socony Mobil-5

NOMENCLATURE

α : Static dipole polarization
b : Distance to nearest neighbour
c : Speed of light in a vacuum
C_6^{ij} : Dispersion coefficient for atom pair ij
ΔE_f : Energy of formation
E_{O-Pt} : Energy for a Pt surface with O present
E_{Pt} : Energy for a clean Pt surface
$E_{Pt(1x1)-O}$: Energy for a fully saturated Pt surface with O
E^{elec} : Electronic energy at $T = 0\ K$
E^{vib} : Energy contributions due to vibrations
E^{rot} : Energy contributions due to rotation
E^{trans} : Energy contributions due to translation
E_{KS-DFT} : Self-consistent Kohn-Sham energy
E_{disp} : Empirical dispersion correction
E_{XC} : Exchange correlation energy
E_x^{GGA} : GGA exchange energy
E_c^{LDA} : Local correlation energy
E_c^{nl} : non-local correlation energy
E_x^{LDA} : Exchange energy density
$E_{ads}(T,P)$: Adsorption energy at a certain temperature (T) and total pressure (P)
$F_x(s)$: Enhancement Factor
f_{damp} : Dampening factor
g : Degeneracy number
G_i : Gibbs free energy
$G_{ads}(T)$: The Gibbs free energy of an adsorbate
$\hbar$: Planck's constant
H_i : Enthalpy
I_x : Moment of inertia about axis x
I_p : Ionization potential
k_B : Boltzmann constant
m : Mass of adsorbate
M : Number of identical adsorption sites
Me : Metal atom
N : Number of adsorbates
N_{at} : Total number of atoms present
N_A : Avogadro's number
n_{rot} : Rotational number
R : Ideal gas constant
R_{ij} : Interatomic distance
s_6 : Global scaling factor

S_i : Entropy
μ : Chemical potential
v : Vibrational mode
W_x : Translation barrier in the x axis
θ : Monolayer coverage
ψ : Wave function
σ : Symmetry number per molecule

GLOSSARY

Translation barrier : The energy required for an adsorbate to move to an adjacent site.
S22 dataset : A data collection of weak dimer and common biological molecules.
2D lattice gas : Treating an adsorbate as if stuck in a harmonic oscillation potential increases to infinite potential with increasing displacement.
2D ideal gas : Treating an adsorbates potential as flat except at the edges of the surface where it reaches infinite.
Hindered Translator : Confined between that of 2D lattice gas and 2D ideal gas.

1. INTRODUCTION

1.1 Context

The total energy consumption has risen as the world population continues to rise and countries continue to develop. The end product for most energy intensive raw materials such as oil, natural gas, renewable sources or coal is the production of power and high-energy density liquid fuels. The total energy consumption for each source of energy can be seen in Figure 1-1. Since 1995 the total consumption of the world has risen by over 50 %.

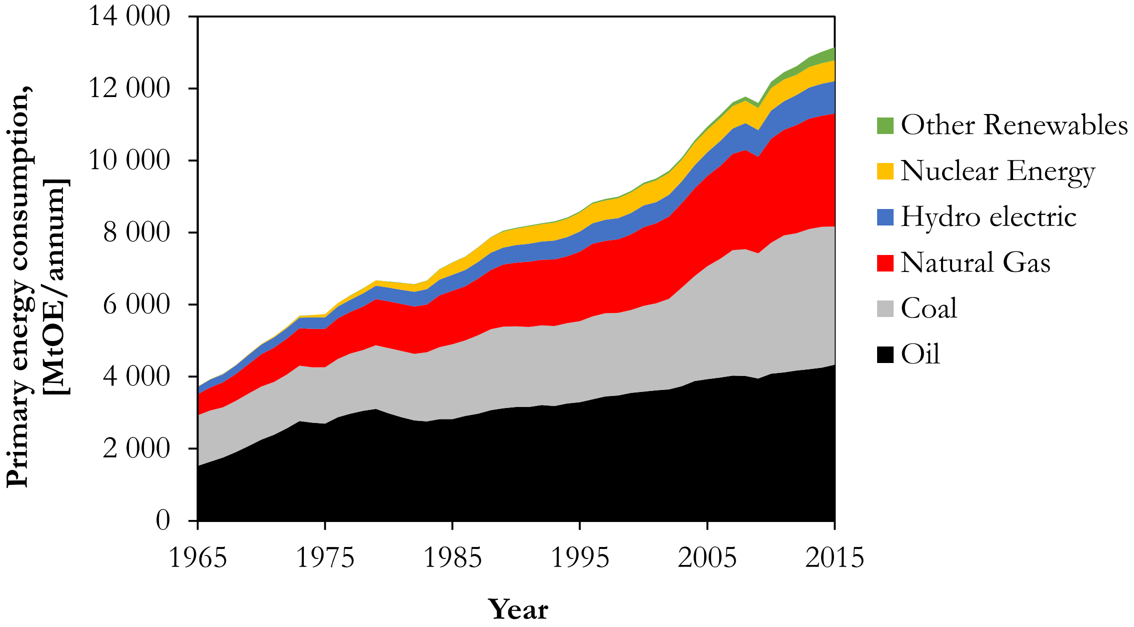

Figure 1-1: Total world energy consumption measured in Million tonnes Oil Equivalent (MtOE) per annum from 1965 to 2015 split according to the major forms of raw material [1].

The environmental impact of using fossil fuels, primarily coal and oil, has been well documented. The relatively low production cost per unit of power from these sources is offset by high carbon dioxide emissions. To counter the associated increases in CO_2 levels there has been a rise in energy production from both green process and carbon neutral cycles. However, renewable energy accounts, at present, for less than 10 % of total energy consumption across the globe and the majority of the world energy supply is still dominated by oil, coal and natural gas [1].

One of the great appeals of these forms of energy is its accessibility. A fuel such as natural gas can be collected and converted into power where needed. This becomes more important when considering the developing world, such as African economies, where infrastructure limits power transportation across the continent. In these locations the energy needs to be produced where it is needed which requires the installation of the appropriate technology and the utilization of the appropriate fuel source for the power generation.

As technology continues to improve, power generation from renewable processes is becoming more appealing, such as the development of the improved polymer tandem solar cells [2]. However, generating the power output for a city using solar technology would require a much higher capital investment than other technologies such as fuel cells. Fuel cell technology maybe a suitable method of power production particularly considering its low physical maintenance cost [3], [4] and may utilize even natural gas or biogas, if it contains no or minute levels of sulphur, as the fuel source. Fuel cell usage may come with reduced maintenance costs [5] compared to current power generation such as coal or gas power generation which require turbines that undergo operation stresses. It can be said that with lower maintenance costs the majority of the operation costs comes from transportation of the fuel. This transportation leads to the next type of energy consumption, high-energy density liquid fuels.

Although there is an increase in renewable power generation, bulk transportation of goods and services will still require liquid fuels. Rail transport, truck hauls and the aviation industry require extensive torque output for raw material and goods transportation which exceeds the current output of small scale electrical motor resulting in a hybrid generator and combustion chamber [6] to make up the power required. In aviation transport alone, the turbine has been designed to function with a high energy combustion to generate the forces required. Redesigning the turbines would require excessive research with aviation authority approval testing before implementation delaying the procedure for several years [7]. This, combined with the forecasted increase in liquid fuel demand from around 95 to 103 million barrels oil per day from 2015 to 2030 [8], implies that the world demand for liquid fuel will remain high for at least the next 15 years.

To determine a possible solution to these demands, it is important to define what classifies a high-energy density liquid fuel. A high-energy density is effectively a large specific energy which implies a large amount of energy released for a relatively small volume or mass of fuel. The appeal of a liquid based fuel arises from the transportation and storage efficiency, requiring far less storage/transportation cost than that of a gas [5]. Typically, high-energy liquid fuels have been dominated by gasoline and diesel but as this fuel source originates from a limited supply of crude oil finding a more flexible source is desired. However, a new fuel source could require remodelling of engines, if the new fuel is incompatible with existing engines. To combat this and ease a transition from one liquid fuel to another it is advisable to find a fuel that could be partially introduced to allow for sufficient time for engine adaptation. One such liquid fuel that fulfils these criteria is methanol.

Commercial engines are able to operate with a gasoline fuel containing up to 15 % methanol addition from as far back as 1973 [9]. There are several other appealing properties that a methanol liquid fuel provides which make it a source worth investigating. Methanol has a higher auto ignition temperature of 467 °C than gasolines (222 °C [5], [9]) but has a relatively low boiling temperature of 64.6 °C [5] which makes it easier and safer to transport while still being able to vaporise for combustion at relatively low temperature. Methanol also contains a high energy density of 19.7 $MJ.kg^{-1}$ which equates to around half the energy density of gasoline of 46.4 $MJ.kg^{-1}$ [5]. This makes methanol an attractive substitute as the variety of sources can offset the energy density difference along with the inherent safer transportation conditions.

1.2 Methanol as a fuel

1.2.1. Applications of methanol

Natural gas converted into methanol is a candidate for energy fuel research for the reasons outlined above. Along with the ease of transport of methanol [9] it can be directly converted to gasoline using the Mobil methane-to-gasoline process [10]. Furthermore methanol is a versatile fuel in itself which can be used as a fuel in direct combustion or in a direct methanol fuel cell power generation [3], [11], [12].

Direct methanol fuel cells (DMFCs) for power production have been a field of interest [3], [4], [12], in which methanol is converted at the cathode [4]:

$$CH_3OH + H_2O \rightarrow CO_2 + 6H^+ + 6e^- \qquad 1\text{-}1$$

The protons then react with the oxygen at the anode to form water:

$$\frac{3}{2}O_2 + 6(H^+ + e^-) \rightarrow 3H_2O \qquad 1\text{-}2$$

The overall reaction across the membrane interface can be taken as:

$$CH_3OH + \frac{3}{2}O_2 \rightarrow CO_2 + 2H_2O \qquad 1\text{-}3$$

The choice of metal for the cathode/anode when using methanol becomes important due to the high acidity the membrane can experience during the proton transfer. Typical DMFC research focuses on Pt based systems [3], [4], [11], [13] as this material allows the electrode to resist the acidity. Platinum also has the highest catalytic activity for oxygen reduction of any of the pure metals and is an active metal for the dissociative adsorption of methanol [4].

In addition to its utility in thermal combustion and DMFC or power generation, methanol also has a variety of uses as a feedstock. Methanol as a feedstock is often used in the formation of formaldehydes, acetic acids, methyl tertiary butyl ether (MTBE), methyl methacrylate (MMA), dimethyl carbonate (DMC) and as a liquid solvent [14]. Additionally, methanol can be reacted over a Ag-ZSM-5 zeolite catalyst to achieve yields of aromatic hydrocarbons up to 56 % after 5h of operation [15]. This creates higher grade petroleum products with low alkane production. As a result the production demand for methanol continues to grow with one of the world's largest methanol produces, Mitsubishi Gas Chemical (MGC), having methanol production plants operating across the globe, in Jose Venezuela (850,000 tons/annum), Al-Jubal Saudi Arabia (2,550,000 tons/annum) and Brunei (850,000 tons/annum) [16].

1.2.2. Current methods to produce methanol

Methanol is presently produced by reacting synthesis gas (syngas) (CO / H_2 mixture) [17], [18] as shown in Equation 1-4. It has been found that catalysts such as iron, nickel and aluminium [19] [14], used to react the syngas feed, achieve high yields with current commercial usage utilizes a copper zinc catalyst.

$$CO_{(g)} + 2H_{2\,(g)} \rightarrow CH_3OH_{(l)},\ \ \Delta H^0_{298K} = -\,90.8\ kJ/mol \qquad 1\text{-}4$$

Syngas can also be generated by reforming or gasification of sources such as biomass, natural gas, coal or from any carbon containing source [14]. Due to the relative low cost and ease of accessibility natural gas has become a preferred feed stock in syngas production via reforming. The reforming of natural gas can occur by reaction with water [19], Equation 1-5, or by dry reforming carbon dioxide [14], Equation 1-6.

$$CH_{4\,(g)} + H_2O_{(g)} \rightarrow CO_{(g)} + 3H_{2\,(g)},\ \Delta H^0_{298K} = 206\ kJ/mol \qquad 1\text{-}5$$

$$CO_{2\,(g)} + CH_{4\,(g)} \rightarrow 2H_{2\,(g)} + 2CO_{(g)},\ \Delta H^0_{298K} = 247\ kJ/mol \qquad 1\text{-}6$$

The combination of the syngas formation and the methanol production from the syngas forms the two-step process currently used to produce methanol. The syngas formation requires a large amount of energy input compared to the heat released in the methanol formation. Due to the endothermic reactions of the syngas formation, operating temperatures can reach up to 800 °C → 1200 °C [14], [20]. The higher operating temperature increases deactivation from coke formation on the catalyst [14] which increases both the capital and maintenance costs.

The syngas production is therefore the main cost contribution to methanol production. It would be beneficial to expand research into an alternative pathway that bypasses the syngas formation. One such pathway is the formation of methanol via an acid complex intermediate, particularly that of methyl-bisulphate. The advantage of this pathway is the high conversion of 90 % and selectivity of 81 % [20] towards methanol at comparatively low temperatures (200 °C) [21]. The overall pathway has been described by Palkovits et al. [21] and the reactions are: methane oxidation to methyl bisulphate (1-7), hydrolysis to form methanol (1-8) followed by SO_2 re-oxidation (1-9) given an overall methanol formation reaction (1-10):

$$CH_4 + H_2SO_4 + SO_3 \rightarrow CH_3OSO_3H + H_2O + SO_2 \tag{1-7}$$

$$CH_3OSO_3H + H_2O \rightarrow CH_3OH + H_2SO_4 \tag{1-8}$$

$$SO_2 + \frac{1}{2}O_2 \rightarrow SO_3 \tag{1-9}$$

$$CH_4 + \frac{1}{2}O_2 \rightarrow CH_3OH \tag{1-10}$$

Although the operating temperature is drastically reduced when compared to syngas formation, there are operational drawbacks to working with sulphuric acid. The corrosive aspect of the reaction increases reactor material costs and the presence of sulphur has the potential of poisoning any sulphur sensitive catalysts. Considerations also need to be given to the presence of sulphur dioxide as emission standards need to be upheld which further increase the operating cost. Despite this there has been promising catalyst activity seen for methanol via methyl bisulphate formation using Pt [21] and Hg [22] alloys.

Alternative catalysts which can operate at low temperatures include the use of zeolites such as Fe-ZSM-5 and Cu-ZSM-5 [20], [23]. The procedure for methanol production using a catalyst such as the Cu-ZSM-5 includes activating the catalyst at 450 °C with oxygen, then the catalyst is cooled to 200 °C and reacted with methane in the absence of oxygen to saturate the surface [20]. Methanol is then extract by desorption in the presence of steam which can provide methanol yields of 8.9 $\mu mol.g^{-1}$ with high selectivity [20]. This can be improved by utilizing a mordenite framework zeolite (MOR) such as Cu-MOR catalyst at high methane pressures of 36 bar, operated isothermally at 200 °C, to give 103.3 $\mu mol.g^{-1}$ [20]. However, the methanol is prone to undergo further oxidation this results in the fluctuating yields often coming with low methane conversions. The reason that these zeolite catalysts perform reasonably well with regard to selectivity at low temperatures is because they act similarly to methane monooxygenase enzymes [23].

Zeolites have isolated active sites which limits the catalyst reactive surface. This causes a radical favoured pathway where a methyl group interacts with the surface via stabilization by an OH bond rather than directly reacting with the surface active site [23], [24]. This makes zeolites reactive, as mentioned, but due to the reactivity of methanol and formaldehyde, the catalyst still needs to be limited to prevent methanol adsorption and reaction onto the surface when using these zeolite approaches. Similar high methanol selectivity can be achieved by reacting methane over a Au-Pd/TiO_2 with H_2 and O_2. This forms a radical intermediate with methyl hydro peroxide [23]. However, as with the zeolites the methanol conversion for this reaction is typically very low making it less favourable [23], [24].

The selectivity and conversion for these radical steps has been investigated for a variety of catalysts, specifically when considering oxidative coupling of methane to methanol [23], [25], at a variety of temperatures. At 700 °C, during aromatic production from methane in the presence of methanol, a Mo/HZSM-5 catalyst has been reported to achieve 95 % methanol selectivity with a methane conversion of 26 % [25]. The conversion of methane can be improved by substituting a Fe/SiO_2 catalyst at the same conditions which increases the conversion to 13.2 % but drops the selectivity to 70 % [25], attributed to the increased oxidation potential for methanol on the surface. However, these conversions require high operating temperatures, to improve cost and selectivity the temperature can be dropped. Low temperature methanol synthesis is preferred using the previously mentioned Fe-Cu/ZSM-5 catalysts, which can achieve 92 % selectivity at 50 °C but due to the lower kinetics the methane conversion only reaches 0.5 % [25]. Taking these two temperatures, 700 °C and 50 °C, it would seem that an intermediate may be useful for methanol formation. Operating at 180 °C, catalysts containing 6 wt% $Hg^{(II)}$ or $Pt^{(II)}$ are able to achieve methane conversions of 50 % and 34 % respectively [25]. In these cases, the safer Pt catalysts are preferred over mercury containing catalysts for both safety and the higher selectivity (91.6 % [25]).

Despite these activities, selectivity and lower temperatures the comparative ease of syngas formation and increased lifespan of catalysts tends current methanol production to focus away from these radical formation steps in favour of the two step process utilizing syngas formation. Although the pathway is unfavourable it remains in use until a more cost effective route can be investigated.

1.2.3. Direct conversion of methane to methanol

An ideal alternative method would be the removal of the intermediate syngas formation and directly convert methane into methanol using a process referred to as the direct conversion of methane to methanol. The advantage of this route would allow a low temperature one-step reaction with an overall reaction given in Equation 1-11 [19]:

$$CH_{4\,(g)} + \tfrac{1}{2}O_{2\,(g)} \leftrightharpoons CH_3OH_{(l)}, \quad \Delta H^0 = -128\ kJ/mol \qquad 1\text{-}11$$

This reaction may involve a single catalytic surface reaction in which methane is reacting with an atomic oxygen adsorbed on an active site [18]:

$$CH_4 + O_{(a)} \rightarrow CH_3OH_{(a)} \qquad 1\text{-}12$$

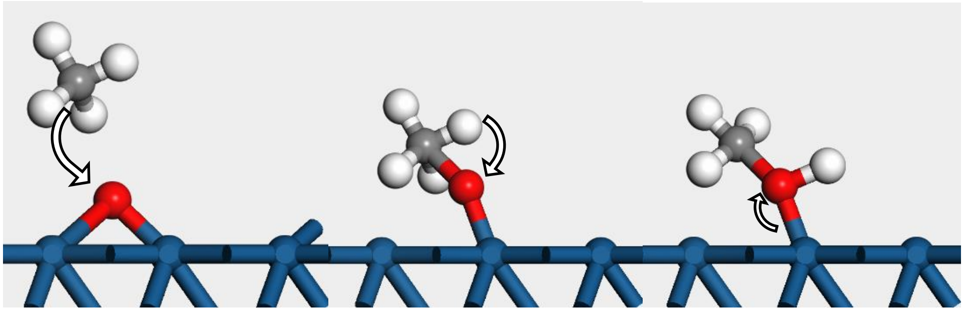

Figure 1-2: Reaction of methane with adsorbed oxygen on a metal surface. Blue - metal, Grey - carbon, Red - oxygen, White - hydrogen

This surface reaction would occur with two competing side-reactions [18], [26], [27] namely methane dehydrogenation in the absence of and in the presence of atomic oxygen on the surfaces given in Equation 1-13 and 1-14 respectively.

$$CH_4 \rightarrow CH_{3(a)} + H_{(a)} \tag{1-13}$$

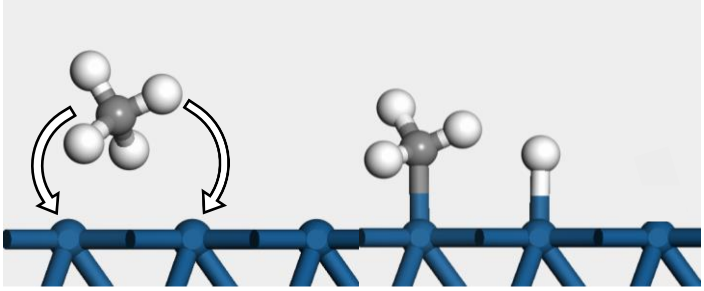

Figure 1-3: Methane dehydrogenation on metal surface. Blue - metal, Grey - carbon, White – hydrogen

$$CH_4 + O_{(a)} \rightarrow CH_{3(a)} + OH_{(a)} \tag{1-14}$$

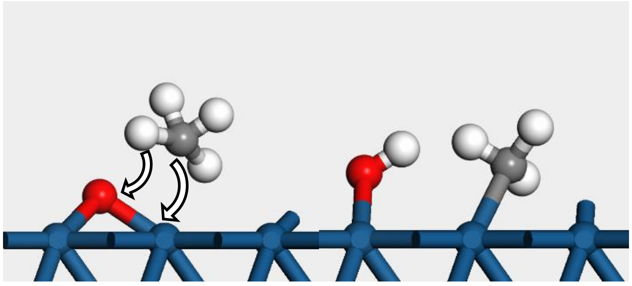

Figure 1-4: Methane dehydrogenation in the presence of adsorbed oxygen. Blue - metal, Grey - carbon, Red - oxygen, White - hydrogen

These side reactions take place on the catalyst surface when a free active site is available. By limiting the availability of free active sites on the catalyst surface the methanol formation reaction may be favoured over the two side reactions. Increasing the coverage on the catalyst might thus increase the selectivity of methanol. This has also been theoretically simulated by Tang et al. [26]. They observed that as the coverage on the catalyst increased the side reactions become less favoured due to the occupation of the free active sites [18]. It is therefore of interest to investigate the parameters that increase the coverage of the catalyst surface while maintaining atomic oxygen adsorption on the surfaces as a means to allow for the direct conversion of methane to methanol.

1.2.4. Platinum as a suitable metal catalyst

When selecting a suitable catalyst for this reaction, there has been growing research into platinum, due to the high catalytic activity for oxygen reduction in low-temperature fuel cells [4], [11] as previously mentioned. Platinum's high catalytic activity for oxygen reduction has been modelled in the work done by Nørskov et al. [13] which plotted the activity and oxygen adsorption energy for different metal surfaces. In their volcano plot, the peak metal was that of Pt followed by Pd, a trend which also occurred when they considered the trend in oxygen reduction activity plotted as a function of both O and OH binding energies.

In essence, the binding of O and OH on Pt is at an optimal level. If we consider the DMFC reaction then metals, such as Ni [4], [13], which increase the binding of O and OH decreases proton transfer rates. In contrast, Au has weaker bonding of O and OH on the surface which increases the dissociation barrier of O_2. The proton transfer becomes more exothermic and the rate increases but O becomes less stable on the surface resulting in the stability of $O_{2\,(g)}$ being preferred [13]. For this reason, the typical choice of metal catalyst is Pt which has the highest activity with regard to O and OH adsorption of any pure noble metal.

The adsorption of O is an important consideration for the direct methane to methanol formation pathway. Relatively strong adsorption is required to ensure sufficiently high coverage on the surface to reduce the potential for side reactions. However, excessively strong adsorption will prevent methanol formation as the reaction barrier increases. The adsorption of OH on Pt also plays an important role in the direct methane to methanol route. This co-adsorption could increase the total coverage of the surface of the catalyst. Consideration for OH will be further explained when considering the adsorption of O containing species discussed later. For now, the trend in activity and adsorption for O on Pt in addition to the high activity for low-temperature synthesis, prompts this research to primarily focus on the adsorption of O on Pt catalyst surfaces.

1.2.5. Platinum nano-particles

The exposed planes on nano-particles are dominated by surfaces with a low surface energy [28]. The planes which form are determined by the geometry that minimizes the surface free energy γ. We can view the surface free energy as the reversible work done in creating a new unit area for a new surface [28], [29]. By minimizing the surface free energy nano-particles tend to form defined equilibrium shapes [28]–[32]. In order to ensure our research will accurately represent a standard Pt nano-particle the preferred equilibrium shape and its resulting dominant surface terraces need to be identified.

There are four equilibrium shapes that metal nanocrystals tend towards namely; a tetrahedron, cubic, octahedron and truncated octahedron [30]–[32], illustrated in Figure 1-5. Experimental synthesis of platinum nanoparticles have found that the thermodynamically preferred shape pertains to that of the truncated octahedron shape [30], [32]. The truncated octahedron platinum shape is dominated by two terraces, the Pt(111) and Pt(100) facets, as indicated in Figure 1-6.

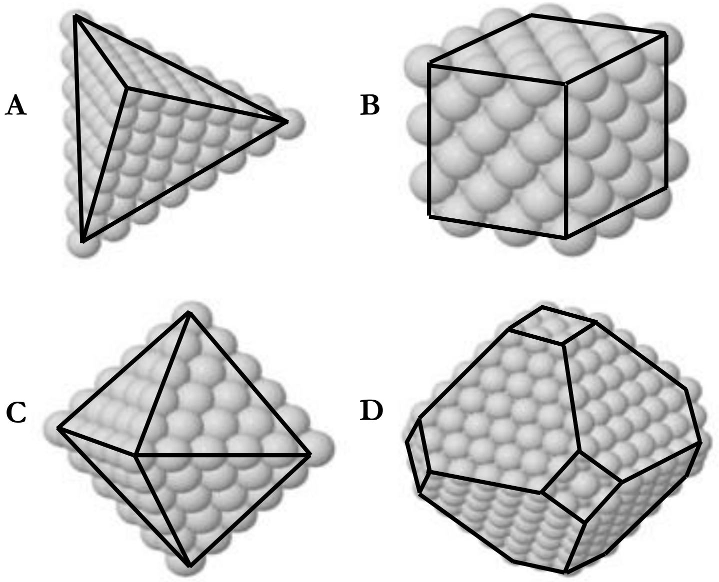

Figure 1-5: Nanoparticle shape configurations: A - tetrahedron, B - cubic, C - octahedron and D - truncated octahedron (images adapted from [32]).

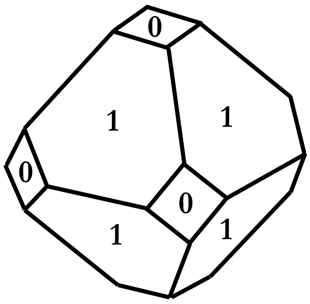

Figure 1-6: Dominant terraces on a platinum truncated octahedron: 0 - Pt(100), 1 - Pt(111).

These two facets dominate small Pt nano-particles (<1 nm). As the particle size increase the perfect shape tends to become deformed with step deformations occurring on each facet [33]. At low equivalent number of atoms nano-particles will tend to form the dominant particle structure, such as the truncated octahedron in platinum's case [32]–[34]. Therefore, when considering a model design for a platinum structure the main focus will be that of adsorption on Pt(111) and Pt(100).

1.2.6. Adsorption of O-containing species on platinum surfaces

There are several sites available on Pt(111) and Pt(100) for adsorption of O-containing species. On the Pt(111) there are 4 adsorption sites of interest namely the fcc, hcp, bridge and top site. The fcc and hcp sites are distinguished by the presence of a second layer atom with the fcc representing an empty hollow site and the hcp hollow site located over a second layer atom. The bridge site adsorption occurs between two surface atoms falling into neither the fcc or hcp hollow site, while top (also referred to as atop) adsorption occurs when the adsorbate bonds directly above one of the surface atoms. A visual representation of all these adsorption sites can be seen if we consider a Pt(111) multi-layered platinum surface, shown in Figure 1-7.

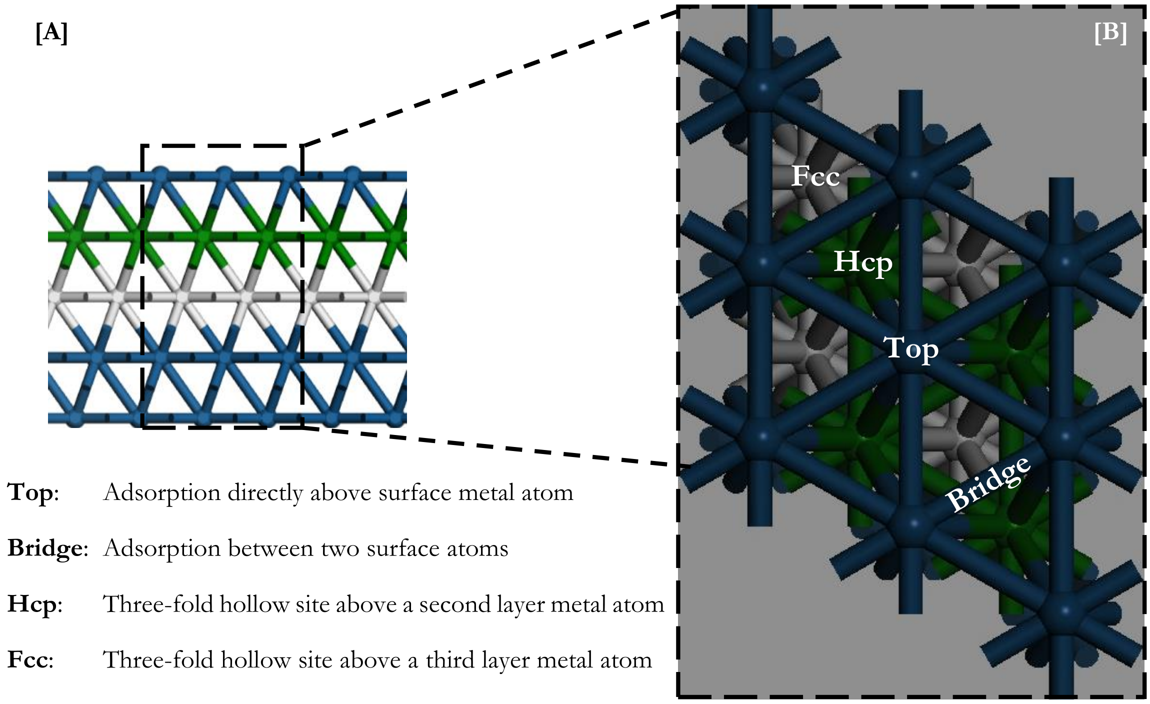

Top:	Adsorption directly above surface metal atom
Bridge:	Adsorption between two surface atoms
Hcp:	Three-fold hollow site above a second layer metal atom
Fcc:	Three-fold hollow site above a third layer metal atom

Figure 1-7: Atomic layer representation of Pt(111) adsorption sites: A - Side view of Pt(111) slab, B - Top view of section of Pt(111) slab (Indicated by the dotted block). Platinum atoms have been coloured blue with the second and third atomic layers' haven been coloured green and silver respectively.

Atomic oxygen adsorbed on Pt(111) has been found to prefer the hollow fcc site [35]–[37]. The adsorption has been experimentally found to reach saturation around an O coverage θ= 0.25 ML (0.25 O atom per Pt atom) at room temperature [36]. At even lower temperatures, 100 K, the saturation coverage tends to only reach 0.50 ML with no ordered structures for oxygen observed using low energy electron diffraction (LEED) [38], [39]. The limited saturation coverage has been attributed to the high repulsive interactions experienced between neighbouring O atoms on the surface [26], [27], [38], [40].

These coverage limitations are in general agreement with density functional theory (DFT) work done by Tang and colleagues [26]. They optimised the coverage of O on a (3x3) Pt(111) surface using a 3 layer slab with a 10 Å vacuum. Using this model, they tested the stability of 15 different O geometries on the surface and reported the formation energy of each. The formation energy for a given coverage θ was defined for O on the Pt(111) surface as [26]:

$$\Delta_f E = E_{O-Pt} - (1-\theta)E_{Pt} - \theta E_{p(1x1)-O} \tag{1-15}$$

Where E_{O-Pt} is the energy for the O geometry at a coverage of θ, E_{Pt} refers to the energy of a clean Pt(111) surface and $E_{p(1x1)-O}$ is the total energy of a fully saturated surface. In order to visualise the formation energy defined here an illustrated equivalent, see Figure 1-8, is present for a system where θ = 0.25 ML for a p(2x2) unit cell:

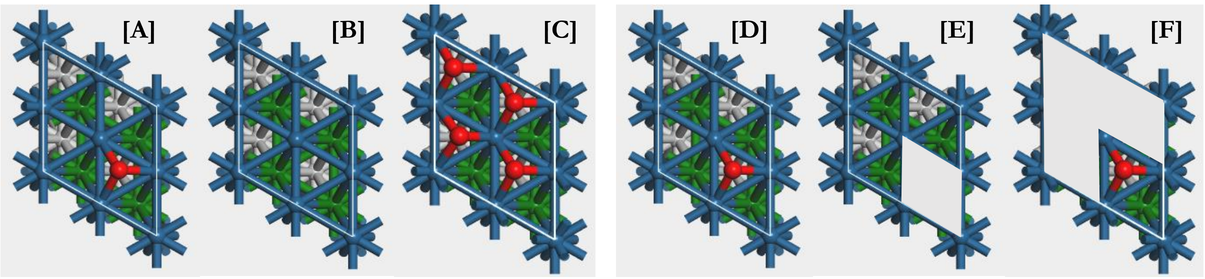

Figure 1-8: Visual representation of Equation 1-15 for Pt(111)-(2x2) with O adsorption present: [A] - E_{O-Pt}, [B] - E_{Pt}, [C] - $E_{p(1x1)-O}$ with [D] - E_{O-Pt}, [E] - $(1-\theta)E_{Pt}$, [F] - $\theta E_{p(1x1)-O}$ for θ = 0.25 ML.

The resulting formation energies are given in Table 1-1 with a visual representation of all the energies given in Figure 1-10 for each of the configurations tested. The geometries are reported relative to the standard geometry for a Pt(111) surface. As an example a (2x2)-O surface represents a standard sized (2x2) Pt(111) surface with one oxygen atom present, while a (√3x2)-O represents a unit cell with only 1 axis in the direction of a typical Pt(111) surface containing an O adsorbate with the unit cell lengths given in the brackets obtained from the geometry. These examples have been illustrated in Figure 1-9:

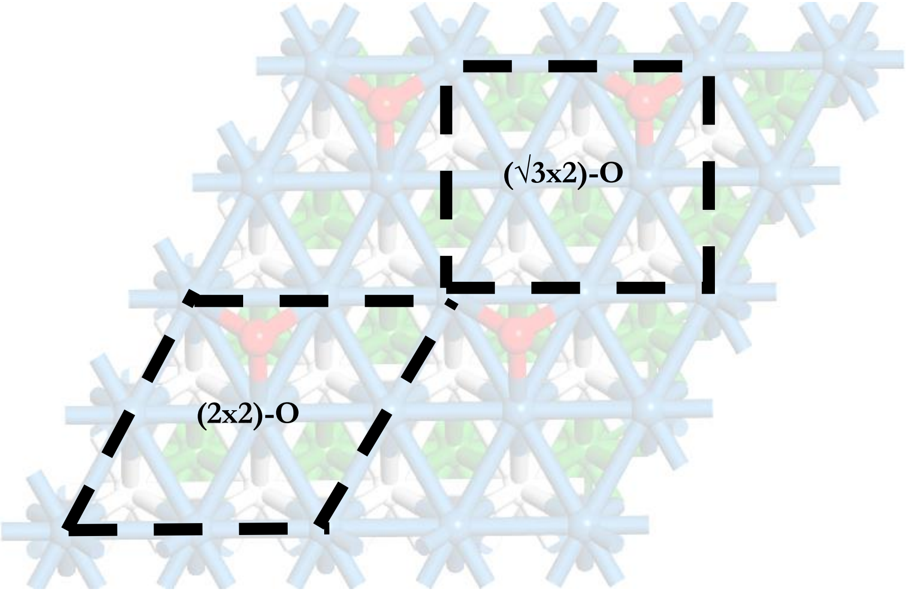

Figure 1-9: Geometries presented using a (2x2)-O and (√3x2)-O on a Pt(111) surface represented on a (4x4)-4O surface.

Table 1-1: Formation energies [meV] for the 15 tested ML coverages with indicated configuration on a Pt cell (Adapted from Tang et al. [26]) with the lowest energies of formation at each coverage given in bold.

Coverage of O [ML]	Configuration	Formation energy [meV]
0	No O – Clean surface	0.000
1/9	(3 x 3) – O	- 107.670
2/9	(3 x 3) – 2O^a	-189.641
2/9	**(3 x 3) – 2O^b**	**-202.428**
1/4	**(2 x 2) – O**	**-245.525**
1/4	($\sqrt{3}$ x 2) – O	-229.897
1/3	(3 x 1) – O	-233.265
1/3	**($\sqrt{3}$ x $\sqrt{3}$) – O**	**-283.512**
1/2	**(2 x 2) – O**	**-340.318**
1/2	($\sqrt{3}$ x 2) – 2O	-326.729
2/3	(3 x 1) – 2O	-266.384
2/3	**($\sqrt{3}$ x $\sqrt{3}$) – 2O**	**-318.790**
3/4	**(2 x 2) – 3O**	**-261.702**
3/4	($\sqrt{3}$ x 2) -3O	-260.625
1	(1 x 1) – O	0.000

a, b – There are 2 configurations for 2O on a (3x3) surface

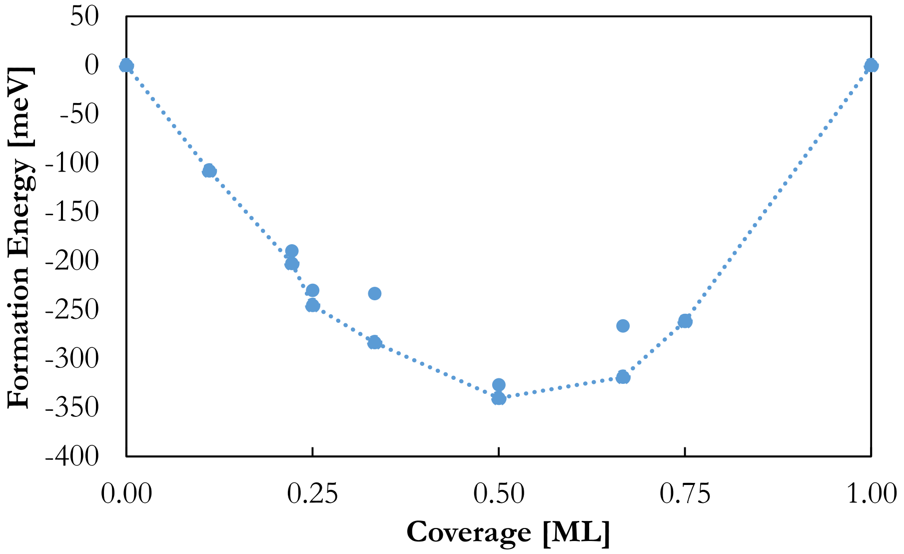

Figure 1-10: Formation energy [meV] for the adsorption of O on Pt(111) (formation energies defined by Equation 1-15.

The formation energies, as defined in Equation 1-15, and subsequent preferred geometries identified follow with the experimentally observed saturation coverage of O at low T corresponding to 0.50 ML, seen in Figure 1-10. This agreement with the experimental saturation coverage for O has been observed in several theoretical studies [18], [27], [36]. In order to increases the selectivity of methanol production, as described in Section 1.2.3, the surface needs to be fully saturated while maintaining an atomic oxygen species presence. To overcome the limitation of single species adsorption co-adsorption with a species that experiences strong attractive forces should be considered.

Water adsorption, resulting in the formation of surface hydroxyl (OH) species, could prove to be a suitable co-adsorption species. There has been extensive research focusing on water adsorption on Pt(111) both experimentally and theoretically using DFT [41]–[43]. Bedurftig [41] and Seitsonen [43] exposed a clean Pt(111) surface to O_2 at 100 K and annealed at 200 K. This created an ordered (2x2) – O structure, as indicated by LEED. The surface was then exposed to water and annealed at 155 K yielding the formation hydroxyl species:

$$H_2O_{ad} + O_{ad} \rightarrow 2OH_{ad} \tag{1-16}$$

An ordered OH adsorbate overlay with a (3x3)-OH structure was observed, which corresponded to a coverage of 0.75 ML. This is higher than the maximum coverage of 0.50 ML seen for O on Pt(111) [26], [40]. To find an attributing factor, they performed scanning tunnelling microscopy (STM) and found that the OH tends to form a six-membered ring on the surface in close packed OH islands, see Figure 1-11 [43]. To investigate this formation, DFT studies by Seitsonen [43] and Michaelides [42] found that these stable, honey-comb like structures were formed due to the top site adsorption preference of OH and the low diffusion barrier of 0.11 eV for bridge to top site adsorption [42]. The low barrier allows OH to form long chains at coverages over 0.50 ML that bind linearly on the top site which point directly towards adjacent OH [42]. The overall result is an attractive dipole-dipole interaction estimated to be 0.34 eV per OH [43] which sustains coverages over 0.50 ML. Further increasing the coverage resulted in their DFT research indicating that the most stable formation occurred when a (3x3)-OH structure was tested, which conforms with the experimental coverage of 0.75 ML.

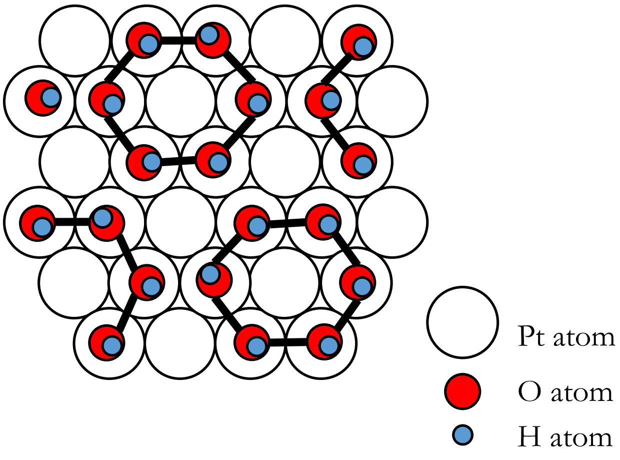

Figure 1-11: Top view of a (3 x 3) surface structure with OH adsorption present in honeycomb shape with solid lines indicating hydrogen bonding [41].

The main contributor to this honey-comb structure is the presence of potential hydrogen bonding [27], [41], [43] and electrostatic contribution from top site OH. The preference for top adsorption site [27], [36], [41] also allows for stabilisation of the adsorption bond via bending, which stabilises OH adsorbates up to 0.75 ML coverage.

As has been mentioned, higher coverages have been postulated to be preferred in the direct methane to methanol reaction route. The high adsorption coverage of OH may complement the low saturation coverage of O and the preferences for separate sites with these two adsorbates could potentially allow for higher co-adsorption potential. In addition, the binding energy, previously mentioned for Pt metals, is neither excessively under or over bound for both O and OH. Finally, the tendency for water and adsorbed O to form OH and O adsorbates makes co-adsorption of water with oxygen on Pt catalyst a field of interest which this research will focus on as a means to reach higher coverages.

1.3 Objective

1.3.1. Problem statement

As the consumption of energy rich raw materials increases, there is a growing demand to create a usable high-energy density liquid fuel. One such fuel is methanol which may be produced by reacting methane with atomic oxygen on a platinum catalyst in a direct synthesis route at low temperatures. In order to increase the selectivity towards methanol and reduce undesirable side reactions, the surface coverage on the catalyst needs to be high, preferably fully covered ($\theta = 1.00$ ML). Atomic oxygen coverage on Pt(111) has been found to be limited to saturation coverages of 0.25 – 0.50 ML both experimentally and theoretically. In contrast, hydroxyl adsorption onto platinum surfaces can reach saturation coverages up to 0.75 ML, due to higher stable coverages attributed to hydrogen bonding and adsorption site preference. In order to increase the coverage on platinum nanoparticle catalysts an investigation into the obtainable coverages, in a co-adsorption system with atomic oxygen and hydroxyl species, has been proposed on Pt(111) and Pt(100). Particular interest will be given to conditions that yield higher coverage up to full coverage.

1.3.2. Scope of study

This research focuses on modelling O and OH adsorption on the Pt(111) and Pt(100) surfaces. Density functional theory (DFT) calculations will be performed to identify how coverage may vary as a function of temperature and pressure. This could identify the conditions that could allow for high coverage on Pt-surfaces. The results will be represented in a surface coverage phase diagram and will be expanded upon to include considerations for dispersion forces such as those associated with van der Waals forces.

This study will only consider the dominant bulk surfaces namely Pt(111) and Pt(100). Coverages from a clean surface up to full monolayer coverage (1.00 ML) will be modelled and no coverages over 1.00 ML will be modelled. This study also focuses explicitly on the obtainable coverages of O, OH and O/OH co-adsorption for use in methanol formation and not on the molecular reactions on the catalyst surface to form an adsorbed methanol species itself.

1.3.3. Hypothesis

It is hypothesised that due to the attractive forces experienced by OH adsorbates, attributed to hydrogen bonding, co-adsorption of O and OH on the dominant platinum terraces will be able to achieve higher coverages than any single adsorbate species due to the high electronegativity of adsorbed O species stabilising higher coverages. It is therefore possible to fully saturate a surface with O containing species at a determinable pressure and temperature.

1.3.4. Key questions

Taking into account the problem statement and the current literature available for coverages on platinum surfaces the key questions for the current study are:

1. What are the stable geometries and subsequent coverages on Pt(111) and Pt(100) for O, OH and O/OH co-adsorption systems?
2. How does the preferred coverage vary as a function of temperature and oxygen/water partial pressure?
3. How does the inclusion of a dispersion model, to incorporate van der Waals interactions, affect the stable coverages and adsorption energies?
4. At what low temperature conditions can a Pt nanoparticle be fully saturated while maintaining an adsorbed O species?

2. MODELS

2.1 Computational modelling methods

Computational modelling of atomic structures is based on the solution to the time-independent Schrödinger equation (TISE) given by:

$$H\psi = E\psi \tag{2-1}$$

where H is the Hamiltonian, ψ is the wave function and E is the total energy for the system. The solution to the TISE gives information about the probability distribution for all energy configurations [44], [45]. For any realistic system, the TISE must be simplified by the Born-Oppenheimer approximation. This approximation takes into consideration that electrons move faster and more freely than nuclei movement. Hence, the nuclei position can be considered to be constant in relation to the position of the electrons [44], [45]. The electronic structure is therefore an "electron cloud" surrounding a fixed configuration of nuclei. The electronic structure itself is determined by the solution to the TISE with the result being the ground-state energy. The set of solutions to Equation 2-1 as a function of the nuclei positions maps out the potential energy surface (PES). This PES forms the basis for heterogeneous catalysis modelling.

Analytical solutions to solve the TISE are not feasible for systems with a large number of electrons and as a result approximate numerical iterations are used. One of the simplest techniques for solving the TISE in terms of one-electron orbital is the Hartree Fock Self-Consistent Field (HFSCF) method. The Hartree Fock method approximates the total wave-function as an antisymmetric product of one-electron wave-functions i.e. a Slater determinant to enforce the Pauli Exclusion Principle [26]. In the HFSCF approach the electron wave-function for the system is written as a product of one-electron wave-function with adjustable parameters [44], [45]. Taking this wave-function the TISE can be written into a one-electron equation given by Equation 2-2:

$$-\frac{\hbar^2}{2m}\nabla^2\psi + v\psi = \epsilon\psi \tag{2-2}$$

where $\hbar$ is Planck's constant, m is the rest mass of an electron, ∇^2 is the Laplacian, v is an effective one-electron potential and ϵ is an effective one-electron eigenvalue [44], [45]. The iterative process used to solve Equation 2-2 involves an initial guess for the one-electron wave-function. The average electron interactions energies are determined from these wave-functions and the interactions are substituted into the effective one-electron potential v. The solution yields an improved one-electron orbital. The process is then repeated until orbital convergence is achieved, finally giving the PES required [44], [45].

The HFSCF method is appealing in its simplicity but has the drawback of inaccurate molecular energies due to a lack of inclusion of electron correlation effects [44], [45]. The requirement to account for correlation effects makes it preferable to use an approximate method capable of evaluating these correlation effects. The Density Functional Theory (DFT) is one such method capable of calculating reasonably large systems of particle density for practical effect. The methodology for DFT is similar to that of the HFSCF approach, but with an expanded one-electron potential energy function v to account for the exchange-correlation interactions [44], [45]. This allows DFT to account for an effective electron correlation effect with reasonable computational cost, which scales with M^3, in contrast to the computational cost of the HFSCF method which scales with M^4, where M is the number of *basis-functions* [44], [45].

2.2 Density functional theory

Density functional theory (DFT) was derived by Hohenberg and Kohn (1964) which was expanded upon by Levy (1979) for independent fermions [44]. DFT is used to deal with the interactions of N electrons in an external potential $v(r)$ which is traditionally expressed by the 3N-dimensional Schrödinger equation for a wave-function $\psi(r_1, r_2, \dots r_N)$, where r_i denotes the electron positions and spin coordinates [44], [46]. The Hamiltonian H for N electrons moving in an external potential with a kinetic (K) and electron-electron (V_{ee}) interaction can be considered as [44]:

$$H = K + V_{ee} + \sum_{i=1}^{N} v(r_i) \tag{2-3}$$

Levy defined a functional:

$$F[\rho] = \min_{\psi \to \rho} \langle \psi | K + V_{ee} | \psi \rangle \tag{2-4}$$

The functional applies to all densities $\rho(r)$ that can be obtained from antisymmetric wave-functions. The specific ψ, which minimizes the energy functional in Equation 2-4 for a particular density, will be referred to as the minimum ψ. The minimum ψ gives the density ρ across all wave-function values and allows for the calculations of the total energy (E) expressed in terms of the functional. This refers now to ground-state (GS) energies, wave-functions and densities for minimal ψ . The basic DFT is therefore taken for all $\rho(r)$ given in Equation 2-5:

$$E[\rho] \equiv \int v(r)\rho(r)dr + F[\rho] \geq E_{GS} \tag{2-5}$$

This is referred to as the variational principle [44] in that the differentiable functional E can obtain a minimum such that $E' = 0$, where E_{GS} can be described as the ground state energy defined as:

$$E_{GS} = \int v(r)\rho_{GS}(r)dr + F[\rho_{GS}] \tag{2-6}$$

As the variational principle holds here by minimising the energy functional we can obtain the ground state energy density for the system, this implies that Equation 2-4 needs to be minimized by introducing a wave-function $(\psi^{\rho}_{min}(r))$ that yield a minimized energy such that:

$$E_{GS} = \langle \psi_{GS} | \textstyle\sum_i v(r_i) + K + V_{ee} | \psi_{GS} \rangle \leq \left\langle \psi^{\rho,GS}_{min} \middle| \textstyle\sum_i v(r_i) + K + V_{ee} \middle| \psi^{\rho,GS}_{min} \right\rangle \tag{2-7}$$

By subtracting the interactions between the external potentials the total ground state energy derives back down to that of Equation 2-6 which forms the proof of the basic theorems used within density functional theory [44]. The ground state wave-function can now be determined along with the ground state charge density which then leads to an iterative process as the charge density determines the ground state wave-functions [44]. The general procedure for calculating the ground state properties is for an approximation to be found for $F(\rho)$ and then for the total energy ($E(\rho)$) to be minimised in Equation 2-5 for the potential $v(r)$ of interest which then approximates E_{GS} and $\rho_{GS}(r)$.

The benefit of DFT is that these interactions between atoms and molecules are redefined in terms of the electronic density distribution $\rho(r)$ and an exchange-correlation functional $E_{xc}[\rho(r)]$. This improvement over Hartree-Fock theory allows for the many electron Schrödinger equation to be solved by approximating $E_{xc}[\rho(r)]$ and then solving a single electron equation [44], [46].

2.3 Exchange-correlation functional

The practical implementation of DFT follows the widely accepted Kohn-Sham method [47], [48]. The theory calculates the self-consistent field electronic structure of the ground state properties for the atoms, incorporating an approximation to the exchange-correlation energy functional, $E_{XC}[\rho(r)]$. When determining the exchange-correlation energy, only the energy as a functional of the electron spin up, $n_{\uparrow}(r)$, and spin down, $n_{\downarrow}(r)$, densities needs to be approximated. It has been well established that of the numerous exchange-correlation energy functionals available the generalized gradient approximation (GGA) yields improved results when compared to the local density approximations (LDA) where the latter has been reported to overestimate molecular bond energies [48].

The GGA method yields improved molecular energies, energy barriers and structural energy differences and improves the accuracy of calculated parameters such as lattice spacings and bond lengths [47]. The GGA functional can be expressed as in Equation 2-8:

$$E_{XC}^{GGA}[n_{\uparrow}, n_{\downarrow}] = \int f(n_{\uparrow}, n_{\downarrow}, \nabla n_{\uparrow}, \nabla n_{\downarrow})\, d^3r \qquad 2\text{-}8$$

Where $n_{\uparrow}$ and $n_{\downarrow}$ are the up and down spin densities, respectively, the GGA exchange-correlation functionals can be related to the energy per particle of a uniform electron gas $\epsilon_{xc}^{GGA}(\rho(r), \nabla\rho)$, as shown in Equation 2-9 [47], [48]:

$$E_{xc}^{GGA}[\rho(r)] = \int \rho(r)\epsilon_{xc}^{GGA}(\rho(r), \nabla\rho(r))\, dr \qquad 2\text{-}9$$

This form for the GGA method includes the density gradients. There are several common GGA exchange-correlation functionals that are used in heterogeneous catalyst research, i.e.; the Perdew-Wang functional from 1991 (PW91) [49], the Perdew, Burke and Ernzerhof functional (PBE) [47], which is itself a modification of the PW91 model, and the Revised Perdew, Burke and Ernzerhof functional (RPBE) [48].

The common approach to modelling adsorption on metal catalysts is to use the PBE functional which does not report strong over-binding compared to PW91, for adsorptions upon metallic surfaces such as platinum [50]–[52]. The RPBE functional has also reported accurate chemisorption results on metallic surfaces and has been able to describe surface adsorbates without over-binding but only in the absence of large contributions from van der Waals interactions [52]–[54]. In these conditions, the model yields lower energies than what has been reported experimentally.

The adsorption energies need to be considered along with the predicted physical properties from the model selection. The RPBE and PBE model both predict the adsorption energies without large over-binding but only the latter yields results for lattice and molecular bond lengths which agree with experimentally determined values in the presence of strong adsorbate species such as atomic O and OH [55], [56].

The differences that occur between the PBE and RPBE occurs due to the modification to the local exchange enhancement factor, $F_x(s(r))$, in the exchange energy function:

$$E_{xc}^{GGA}[\rho(r)] = \int \rho(r)\epsilon_{xc}^{GGA}(\rho(r), \nabla\rho(r))\, dr = \int \rho(r)\epsilon_{xc}^{GGA}\big(\rho(r)\big)\mathrm{F_x}(s(r))\, dr \qquad \text{2-10}$$

Where s is the reduced gradient density [44], [48] and the local exchange enhancement factor is expanded upon in Equation 2-11[47], [53], [57], [58]:

$$F_x(s) = 1 + \kappa - \frac{\kappa}{1 + \frac{\mu s^2}{\kappa}} \qquad \text{2-11}$$

The local exchange enhancement factor has two empirical parameters namely μ and κ. The parameter μ is the same for both the PBE and RPBE models. Where these models differ is in the latter parameter (κ_{PBE}= 0.804, κ_{RPBE}= 1.245) [47], [53], [59]. This causes the local exchange enhancement factor to increase more rapidly for the RPBE than the PBE model, and thus results in large reduced gradients being stabilized more with the RPBE as it predicts weaker interactions than the PBE model [53], [60].

The weakened interactions reduces the accuracy of various properties, such as lattice spacing and bond lengths, to values greater than those determined experimentally when compared to the PBE model, as reported by Perdew, Burke and Ernzerhof (1998) summarised in Table 2-1 [55]:

Table 2-1: Bond lengths [Å] from PBE, RPBE and experimental results, values in brackets indicate deviation from experimental results.

Molecule	PBE	RPBE	Experiment
H_2	1.418 (+1.21 %)	1.413 (+0.856 %)	1.401
CH_4	2.071 (+0.926 %)	2.073 (+1.02 %)	2.052
N_2	2.084 (+0.579 %)	2.089 (+0.820 %)	2.072
NO	2.189 (+0.644 %)	2.196 (+0.966 %)	2.175
O_2	2.306 (+1.10 %)	2.313 (+1.40 %)	2.281
F_2	2.672 (-0.225 %)	2.685 (+0.261 %)	2.678

As seen in Table 2-1 when considering the structural properties of these molecules, the PBE functional provides improved agreement relative to experiment compared to the RPBE functional. As a result of the over estimation of geometric parameters calculated with the RPBE functional, many heterogeneous surface reactions on metal surfaces are still investigated using the GGA-PBE approach.

2.4 Application of density functional theory

In this study the Vienna *Ab Initio* Simulation Package (VASP) is used to solve the Kohn-Sham equation [61]–[63], VASP utilizes a plane-wave basis set to solve the electron density. In addition the Blöchl all electron projector augmented-wave (PAW) method is applied to describe the full valence and core wave functions, VASP allows for high-quality DFT simulations incorporating exchange-correlations effects [64].

The exchange-correlation functional selected in this study is the GGA-PAW-PBE model since the presence of atomic O and OH on the surface of Pt(111)/Pt(100) will have both strong and relatively weak interactions in co-adsorbed and mono adsorption conditions. This also enables comparison to be made with other studies that have looked at the adsorption of diatomic and atomic oxygen on platinum surfaces using DFT calculations [26], [35], [65]–[67] all of which used the GGA-PAW-PBE approach. The primary choice for PBE over the RPBE functional is due to the overestimation of bond lengths and lattice spacing obtained with the RPBE functional when compared to experimental results as seen in Table 2-1. As co-adsorption of O/OH on platinum is a relatively new field of interest, the selected model needs to provide reliable convergence of both the adsorption energies and geometric properties while minimising overestimations. As both adsorption and geometric properties are modelled reasonably accurately with the PAW-PBE model this study will use the VASP computational code with a PAW-PBE exchange-correlation energy functional in the initial investigation of the adsorption of atomic O and OH species on an optimized Pt(111) and Pt(100) model.

2.5 Thermodynamic calculations

The optimized model using DFT calculations will only determine the electronic energy (E^{elec}), as the focus of this study is to determine the possible coverages obtainable on the platinum as a function of temperature and pressure, thermodynamic corrections need to be applied. In this section the thermodynamic calculations performed in this research will be outlined, the equations presented are based on the work of Hirano [68] and Sandler [69].

2.5.1. Temperature correction

The first consideration to the thermodynamic energy calculations is the temperature correction to the Gibbs free energy of each component at a given temperature T. The Gibbs free energy of a species i is given in Equation 2-12:

$$G_i(T) = H_i(T) - TS_i \qquad 2\text{-}12$$

Where $H_i(T)$ and S_i are the enthalpy and entropy of the component i. The enthalpy correction from a zero-point DFT energy to the given temperature can be calculated using Equation 2-13:

$$H_i(T) = E^{elec} + E_i^{vib}(T) + E_i^{rot}(T) + E_i^{trans}(T) + RT \qquad 2\text{-}13$$

Where E^{elec} is the DFT calculated energy and the vibrational, rotational and translational contributions are given by $E_i^{vib}(T)$, $E_i^{rot}(T)$ and $E_i^{trans}(T)$ respectively. The ideal gas contributions for vibrational, rotational and translation can be calculated using the partition functions given in Hirano [68] rewritten here in Equations 2-14 to 2-16:

$$E_i^{vib}(T) = \frac{1}{2} N_A \sum_j hv_j + N_A \sum_j \frac{hv_j \exp\left(-\frac{hv_j}{k_B T}\right)}{1 - \exp\left(-\frac{hv_j}{k_B T}\right)} \qquad 2\text{-}14$$

$$E_i^{rot}(T) = \frac{n_{rot}}{2} RT \qquad 2\text{-}15$$

$$E_i^{trans}(T) = \frac{3}{2} RT \qquad 2\text{-}16$$

Where the variables given are defined as:

N_A : Avogadro constant
h : Planck constant
v_j : Vibrational mode of component i
k_B : Boltzmann constant
n_{rot} : Rotation for linear (n_{rot}= 3) or non-linear (n_{rot}= 2) molecules
R : Ideal Gas constant

Similarly, the entropic contribution of a component i at a given temperature T, can be determined using Equation 2-17:

$$S_i(T) = S_i^{vib}(T) + S_i^{rot}(T) + S_i^{trans}(T) + S_i^{degeneracy} \tag{2-17}$$

Where the contributions to entropy for vibration, rotation, translation and degeneracy are given by $S_i^{vib}(T)$, $S_i^{rot}(T)$, $S_i^{trans}(T)$ and $S_i^{degenerancy}$ respectively. It should be noted that the rotational contribution for entropy has two different equations depending on whether the molecule is linear or non-linear. The values for each of these contributions can be calculated as shown in Equations 2-18 to 2-22:

$$S_i^{vib}(T) = R\sum_j \frac{\frac{hv_j}{k_BT}\exp\left(-\frac{hv_j}{k_BT}\right)}{1-\exp\left(-\frac{hv_j}{k_BT}\right)} - R\sum_j ln\left(1 - hv_j\exp\left(-\frac{hv_j}{k_BT}\right)\right) \tag{2-18}$$

$$S_i^{rot-linear}(T) = Rln\left(\frac{8\pi^2 I k_B T}{\sigma h^2}\right) + R \tag{2-19}$$

$$S_i^{rot-nonlinear}(T) = \frac{R}{2}\ln\left(\frac{\pi}{\sqrt{\sigma}}\frac{8\pi^2 cI_A}{h}\,\frac{8\pi^2 cI_B}{h}\,\frac{8\pi^2 cI_C}{h}\,\left(\frac{k_BT}{ch}\right)^3\right) + \frac{3}{2}R \tag{2-20}$$

$$S_i^{trans}(T) = R\left(\ln\left(\left(\frac{2\pi k_B T M_w}{h^2 N_A}\right)^{\frac{3}{2}}\frac{k_BT}{P}\right) + \frac{5}{2}\right) \tag{2-21}$$

$$S_i^{degeneracy} = Rln(g) \tag{2-22}$$

Where the introduced variables are defined as:

I_x : Moment of inertia about the axis x
σ : Symmetry number per molecule i (based on Fernández-ramos et al. [70])
c : Speed of light in a vacuum
g : The degeneracy number (number of arrangements that yield the same energy)
P : Pressure of the system

The contributions of each correction are treated differently when regarding a gas phase molecule (as gas molecules are used as a reference state) or a surface adsorbate. Gas phase molecules are assumed free in all directions and so can vibrate, rotate and translate freely, as a result when calculating these gases all contributions are taken into account. Adsorbed species are considered restricted in their capacity to rotate and translate as the chemical bond with the surface restricts these movements. It is therefore assumed that there is no contribution by hindered rotation or translation and only the vibrational contributions are taken into consideration when considering the contributions to adsorbates in most studies.

2.5.2. Hindered translation

There is an additional consideration towards the stability of an adsorbate that needs to be taken into account that of translational stabilization. Typically, the energy of an adsorbate is considered well represented by considering the adsorbate as fixed in its adsorption site. This implies that the thermodynamic properties are calculated considering no contributions from rotational or translational entropy/enthalpy. Taking this into account implies that on the surface an adsorbates properties have no E_i^{trans}, E_i^{rot} or S_i^{trans}, S_i^{rot} in comparison to a gas phase species. Although their rotationally restricted the translation contributions become significant as the translation barrier drops (W_x). In this section a brief outline of how translation contributions can be modelled will be outlined and are primarily based on the work done by Hill [71], Campbell [72] and Sprowl [73].

When describing a gas adsorbed on the surface with a translation contribution there are 3 main approaches used. The choice of which one best represents the system is based on the translation energy barrier. The translation barrier is the energy required for an adsorbate to move a distance b to the nearest neighbour identical adsorption site. To more readily explain this we can consider a Pt(111) surface with an adsorbate present on the surface undergoing a surface movement from a lower energy fcc to an adjacent hcp site. This translation movement is determined by the minimum distance between the two stable adsorption sites approximated by the surface distance to the hypothetical nearest neighbour atom [71], which effectively predicts ideal linear movement between two identical adsorption sites. The translation barrier is the energy needed to overcome the shift over the bridge site, a comparative view is to see this as an activation energy required to initiate the translation.

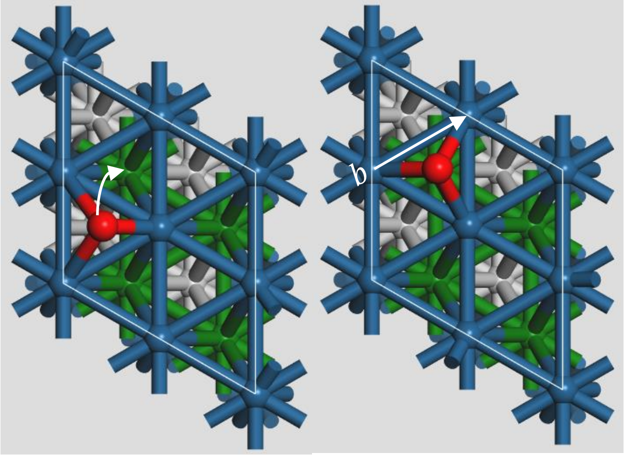

Figure 2-1: Adsorbate translation from an fcc to hcp site on Pt(111) with nearest neighbour distance to identical adsorption site (fcc → fcc) (b).

The energy required to initiate this movement, referred to as the translation barrier in the axis of motion, determines how the adsorbate on the surface should be treated. The translation barrier can take one of 3 forms which we will refer to as a high, moderate or low translation barrier when compared to the relative energy of the adsorbates present, see Figure 2-2.

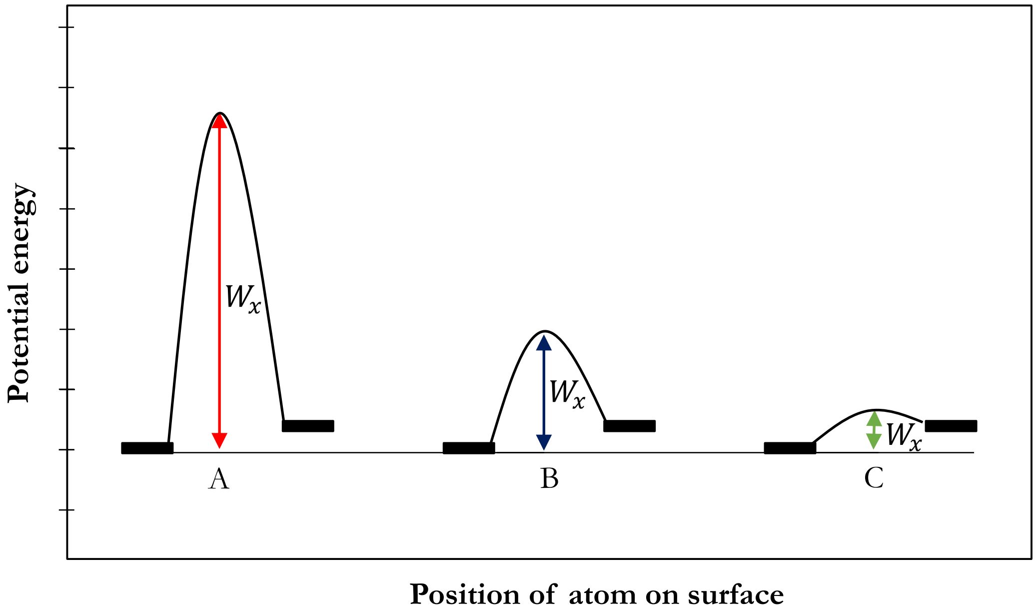

Figure 2-2: Potential energy for the translation of an adsorbate from a lower energy site to a higher energy site against relative position on the surface. A - high barrier, B- moderate barrier, C - low barrier

The translation barrier can be calculated when adsorbates experience localized adsorption and vibration about a minima with a frequency in each axis by making several assumptions [71]–[73]:

- The translation barrier in the x and y axis are equivalent,
- Solid density remains unchanged upon adsorption,
- All adsorbates have negligible interactions between each other such that the vibration can be linked to the translation barrier.

The link between translation and vibration (v_x) is based on the mass of the adsorbate m and the geometry of the surface structure. For a (100) surface the translation barrier can be calculated by utilizing the (100) area function Mb^2[71], where M is the number of identical sites available:

$$v_x = v_y = \left(\frac{W_x}{2mb^2}\right)^{\frac{1}{2}} \tag{2-23}$$

A similar link can be generated for a (111) surface by taking into account the (111) area function $M\left(\frac{\sqrt{3}}{2}\right)b^2$ [71]:

$$v_x = \left(\frac{W_x}{\sqrt{3}mb^2}\right)^{\frac{1}{2}} \tag{2-24}$$

These translation barriers can now be compared to the energy available to determine which barrier type is present, Figure 2-2. The energy available to each adsorbate can be calculated by considering Boltzmann's constant and the temperature of the system (k_BT) [72], [73]. If W_x is substantially larger [A] than the energy for each adsorbate then the barrier is considered high and the adsorbate is treated as a 2D ideal lattice gas as it is stuck in harmonic oscillation in both the x and y direction

[71]. This implies that when considering the energy of the system considering only vibrational considerations are needed to accurately describe the adsorbate ($E^{trans} = S^{trans} = 0$).

The alternative extreme is when the energy of the adsorbate greatly exceeds W_x [C], in this case the adsorbate potential is effectively flat except at the surface edges where they go off to infinity [71]. In this case the adsorbate acts more like a free moving 2D ideal gas with free translation and vibration only in the axis perpendicular to the plane. In this case it is best to describe each characteristic with reference to gas phase energies, considering entropy as an example the entropy is more reliably describe by:

$$S_{ad}^{0} = S_{gas}^{0} - \frac{1}{3} S_{gas,trans}^{0} + S_{vibZ}^{0} \qquad \text{2-25}$$

The final type of barrier that can be seen is when W_x falls between these two extremes [B], when the adsorbate is considered to behave as a hindered translator. In this case the adsorbate has contributions from both vibrational movement and from translation such that the effective energy can be described by add the harmonic oscillation energy $E_{HO,i}$ with a contribution from translation ΔE_x such that:

$$E_{total} = E_{HO,i} + \Delta E_x \qquad \text{2-26}$$

The harmonic oscillation energy is calculated as previously mentioned in the temperature correction section. The addition ΔE_x is given by [71]:

$$\Delta E_x = N k_B T \left(-\frac{1}{2} - \frac{1}{(2 + 16 r_i) T_i} + \frac{r_i}{2T_i} \left(1 - \frac{I_1 \left[\frac{r_i}{2T_i} \right]}{I_0 \left[\frac{r_i}{2T_i} \right]} \right) \right) \qquad \text{2-27}$$

Where T_i and r_i are the dimensionless temperature value and energy to frequency barrier respectively, each calculated via:

$$T_i = \frac{k_B T}{h v_i} \qquad r_i = \frac{W_i}{h v_i} \qquad \text{2-28}$$

Where W_i is the aforementioned translation barrier and v_i is the vibration associated with the translation, see Equation 2-23/2-24. The ratio of T_i and r_i is solved using both a zero ordered modified Bessel functional and one of the first kind given by I_0 and I_1 respectively. The zero ordered modified Bessel functional is a solution to a second-order ordinary differential equation:

$$x^2 \frac{d^2 y}{dx^2} + x \frac{dy}{dx} - (x^2 + n^2) y = 0 \qquad \text{2-29}$$

Which can be solved for real numbers using:

$$I_n(z) = \frac{1}{\pi} \int_0^{\pi} e^{z cos\theta} \cos(n\theta) \, d\theta \qquad \text{2-30}$$

When considering the entropy of a hindered translator the same approach to that of the energy is used in that there is the standard harmonic oscillation contribution, $S_{HO,i}$, with an additional translation contribution, ΔS_x:

$$S_{total} = S_{HO,i} + \Delta S_x \qquad \text{2-31}$$

The contribution to entropy from translation is again an equation that requires a Bessel functional and takes the form:

$$\Delta S_x = Nk_B\left(-\frac{1}{2}-\frac{r_i}{2T_i}\frac{I_1\left[\frac{r_i}{2T_i}\right]}{I_0\left[\frac{r_i}{2T_i}\right]}+\ln(\left(\frac{\pi r_i}{T_i}\right)^{\frac{1}{2}} I_0\left[\frac{r_i}{2T_i}\right])\right) \qquad \text{2-32}$$

These additional calculations will need to be considered should the translation barrier be such that the adsorbate is best considered as a hindered translator, which will require determining the translation barrier, the relative translation frequency and adsorbate pathway. However, it has been observed [72], [73] that a hindered translator model can still reliably predict systems with high W_x, this implies that the energies calculated using a hindered translator model and those of a 2D ideal lattice gas will yield the same result when W_x is high.

2.5.3. Determining the vibrational frequencies

In order to determine the enthalpy and entropic contributions of adsorbed species and the gas phase references the vibrational frequencies are required. The vibrational analysis performed calculates the second derivate of the energy with respect to the position for each atom (the Hessian matrix). In the vibrational analyses a displacement step of 0.02 Å was used in all three Cartesian directions. Due to the relative size of Pt atoms to the adsorbates (O/OH) the Pt atoms are considered immobile due to the bulk presence in the crystal structure, due to this assumption there is no contribution due to vibrations from Pt atoms, this was practically implemented by fixing the Cartesian positions of the Pt atoms in their geometrically optimized positions and only allowing the adsorbates to vibrate.

2.5.4. Reference state for adsorption energy

As mentioned we consider two gas phase molecules as our reference state that of oxygen (O_2) and water (H_2O). In order to determine which coverages are obtainable on the Pt(111) and Pt(100) terraces the change in Gibbs free energy upon adsorption was determined, as the system will tend towards the lowest total Gibbs free energy for the system. In this study the change in Gibbs free energy upon adsorption for a system i at a temperature and pressure (T, P) is defined in Equation 2-33:

$$G_i(T,P) = G_{Adsorbed\,surface}(T,P) - G_{clean\,surface}(T,P) - G_{gas\,reference}(T,P) \qquad \text{2-33}$$

Where $G_{Adsorbed\,surface}(T,P)$ is the Gibbs free energy of the slab with the adsorbed species at a certain coverage, $G_{clean\,surface}(T,P)$ is the Gibbs free energy of a clean slab and $G_{gas\,reference}(T,P)$ is the total Gibbs free energy of the adsorbate species in their gas phase equivalent stable forms. The gas reference states are important to define for each adsorbate combination on the surfaces for use in Equation 2-33.

In this study a p(2x2) cell is used which corresponds to potential coverages of 0.25, 0.50, 0.75 and 1.00 ML on the surface with four adsorption sites available for any combination of adsorbate species. As each coverage will have its own gas reference, the relative coverages with the adsorbate species that will be modelled and tested in this study are given in Table 2-2 and Table 2-3 along with the gas reference states needed for Equation 2-33.

Table 2-2: Adsorbates present for coverages of 0.25 and 0.50 ML with the gas phase reference reaction for Gibbs free energy determination.

Coverage [ML]	Adsorbates present	Adsorption reference equation
0.25	O	$\frac{1}{2}O_{2,(g)} \rightarrow O_{(a)}$
	OH	$\frac{1}{2}H_2O_{(g)} + \frac{1}{4}O_{2,(g)} \rightarrow OH_{(a)}$
0.50	$2O$	$O_{2,(g)} \rightarrow 2O_{(a)}$
	$2OH$	$H_2O_{(g)} + \frac{1}{2}O_{2,(g)} \rightarrow 2OH_{(a)}$
	O/OH	$\frac{1}{2}H_2O_{(g)} + \frac{3}{4}O_{2,(g)} \rightarrow OH_{(a)} + O_{(a)}$

Table 2-3: Adsorbates present for coverages of 0.75 and 1.00 ML with the gas phase reference reaction for Gibbs free energy determination.

Coverage [ML]	Adsorbates present	Adsorption reference equation
0.75	$3O$	$\frac{3}{2}O_{2,(g)} \rightarrow 3O_{(a)}$
	$3OH$	$\frac{3}{2}H_2O_{(g)} + \frac{3}{4}O_{2,(g)} \rightarrow 3OH_{(a)}$
	$2O/OH$	$\frac{1}{2}H_2O_{(g)} + \frac{5}{4}O_{2,(g)} \rightarrow OH_{(a)} + 2O_{(a)}$
	$O/2OH$	$H_2O_{(g)} + O_{2,(g)} \rightarrow 2OH_{(a)} + O_{(a)}$
1.00	$4O$	$2O_{2,(g)} \rightarrow 4O_{(a)}$
	$4OH$	$2H_2O_{(g)} + O_{2,(g)} \rightarrow 4OH_{(a)}$
	$O/3OH$	$\frac{3}{2}H_2O_{(g)} + \frac{5}{4}O_{2,(g)} \rightarrow 3OH_{(a)} + O_{(a)}$
	$2O/2OH$	$H_2O_{(g)} + \frac{3}{2}O_{2,(g)} \rightarrow 2OH_{(a)} + 2O_{(a)}$
	$3O/OH$	$\frac{1}{2}H_2O_{(g)} + \frac{7}{4}O_{2,(g)} \rightarrow OH_{(a)} + 3O_{(a)}$

2.5.5. Chemical potential

The Gibbs free energy of a multicomponent system is based on both the temperature and pressure of the components present, in order to measure pressure contribution to the coverages obtainable the effect of temperature and pressure will be combined into one definable parameter, chemical potential. The chemical potential of a component i is given by the Gibbs free energy per atom (N) at a temperature (T) and Pressure (P) as seen in Equation 2-34 [65], [69], [74]:

$$\mu_i = \left(\frac{\delta G}{\delta N_i}\right)_{T,P,N_{i\neq j}} \tag{2-34}$$

By applying the ideal gas equation, the chemical potential can be redefined [69] to calculate the change in Gibbs free energy over a finite change in pressure from P^0 to P as described in Equations 2-35 and 2-36:

$$G_{T,P} - G_{T,P^0} = \int_{P^0}^{P} \left(\frac{\delta G}{\delta P}\right)_T dP = Nk_B T ln\left(\frac{P}{P^0}\right) \tag{2-35}$$

$$\mu_{i,T,P} = \mu_{i,T,P^0} + k_B T ln\left(\frac{P}{P^0}\right) \tag{2-36}$$

The chemical potential can now be determined at any given pressure and temperature from a predefined reference state. Here, we define the reference state chemical potential at a temperature T and at constant pressure P^0 as the change in Gibbs free energy from the chemical potential at $T = 0$ K and $P^0 = 1$ bar given in Equation 2-37:

$$\mu_{i,T,P^0} = \mu_{i,0\ K,P^0} + \Delta G_{\Delta T,P^0,i} \tag{2-37}$$

Where the electronic energy is taken as the chemical potential at absolute zero. The final equation for determining the effect of pressure on the chemical potential of the adsorbed species is now given in Equation 2-38:

$$\mu_{i,T,P} = G_{\mathrm{T},P^0,i} - G_{0\ \mathrm{K},P^0,i} + k_B T ln\left(\frac{P}{P^0}\right) \tag{2-38}$$

The primary advantage for looking at the chemical potential of the gas species is that we can apply an upper and lower limit to investigate with regards to chemical potential. We will refer to these selected upper and lower limits as the maximum chemical potential that will be tested and the minimum chemical potential that will be tested. The choice of the maximum and minimum was such that above the maximum chemical potential all gas phase molecules condense onto the surface whereas below the minimal chemical potential all components remain in the gas phase [69], [74]. As each chemical potential incorporates several combinations of temperature and pressure determining the coverages from the minimum to the maximum takes into consideration all possible operating conditions. As the focus of this research is to determine oxygen and water adsorption on platinum surfaces the maximum chemical potential corresponds to the critical point of oxygen [69] and of water [69]:

$$\mu_{O_2,\mathrm{max}(-118.6\ ^0C,\ 50.06\ bar)} = -0.20\ eV \tag{2-39}$$

$$\mu_{H_2O,\mathrm{max}(374.2\ ^0C,\ 220.48\ bar)} = -0.95\ eV \tag{2-40}$$

The minimum chemical potential is more difficult to define but for comparative reasons has been selected to be similar to the work with Ruthenium [65], [74] given in Equation 2-41:

$$\mu_{i,min} = -3.5\ eV \tag{2-41}$$

This values corresponds to extreme dilute systems with partial pressures below 10^{-15} bar at conditions of 400 °C. To ensure that a sufficient adsorption chemical potential range is chosen the highest and lowest end of these chemical potentials will be taken which will generate a phase diagram for a chemical potential range of -0.20 → -3.5 eV.

2.6 Consideration for van der Waals forces introduction

The selection of a PAW-PBE models is a good approximation of the adsorption energies to be using the thermodynamic relations described earlier. However, DFT models typically struggle to model the induced dipole intermolecular forces, particularly those associated with van der Waals interactions. As this research focuses on co-adsorption with O_2 and H_2O reference gases these additional London dispersion forces may be an important model addition, especially at high atomic O coverages with induced dipole-dipole forces in OH adsorbates [75]–[77]. These dipole interactions are considered more dominant with OH on Pt than O, which is predominantly a chemisorption process [54].

London dispersion forces are caused by momentary oscillations of electron charge which occur in all atoms [75]–[77], as the close proximity of one atom to another induces a dipole moment between the two. This resulting charge migration causes an attraction between molecules which can assist in adsorption. This attraction interaction is present in long range van der Waals which can strengthen the adsorption onto the catalyst surface, particularly for molecules which experience high induced dipole interactions. Traditional DFT exchange-correlation functional have been limited in their ability to account for long range van der Waals interactions as they are only considered by first-principles, using quantum chemical methods [57]. The limiting factor is that exchange-correlations can be seen to only consider local properties. This can be viewed if we consider two noble gas atoms. The functional will give binding or repulsion only when the electron densities overlap for the two atoms [60]. This can account for close proximity interactions but does not describe long-range electron correlations responsible for van der Waals forces. As dispersion contributions become significantly larger when considering systems containing non-noble components the accuracy to which a DFT model can predict the desired energies may drop away from ideal molecular accuracy. A reasoning for this is that the mathematical form of the functional do not support the physical situation [78]. This reasoning has led to an increase in research surrounding approximating van der Waals interactions in DFT studies [53], [58], [60], [79].

There are two general approaches used to account for van der Waals forces that of a more mathematical appreciation with van der Waals energies estimated using embedded molecular mechanics or an adjusted functional-based dispersion correction approach to account for the "missing" forces. In this section a brief overview of both these approaches will be given along with motivation for the van der Waals choice selected for this research.

2.6.1. Embedded molecular dispersion correction

The approach outlined here is based on the work done by Grimme [78], which was expanded upon in Grimme, Ehrlich and Goerigk [80], this focuses on using a modified GGA with parameterized adjustments to include van der Waals correction. The approach can be seen as working from basic principles and working up towards energies that are reflected in experimentation. Their work focused on modifying their current density functional (DF) GGA to include considerations for short to medium range electron correlation dispersions from a more mathematical theory approach.

The model approximates the dispersion (D) within the functional as a modification to how Becke's GGA functional introduced it, first introduced in 1997 [81], with the total energy modelled by [78]:

$$E_{DFT-D} = E_{KS-DFT} + E_{disp} \tag{2-42}$$

Where E_{KS-DFT} is the self-consistent Kohn-Sham energy, E_{disp} is an empirical dispersion correction based on the number of atoms present in the system, N_{at}, and the dispersion coefficient for an atom pair of ij, denoted as C_6^{ij}, the interatomic distance R_{ij} and a global scaling factor dependent on the DF used, s_6. This gives a dispersion energy by [78]:

$$E_{disp} = -s_6 \sum_{i=1}^{N_{at}-1} \sum_{j=i+1}^{N_{at}} \left(\frac{C_6^{ij}}{R_{ij}^6}\right) f_{damp}\left(R_{ij}\right) \tag{2-43}$$

Where f_{damp} is a dampening factor based on the sum of the van der Waals radii to prevent near singularities for small interatomic distance [80]. This dispersion energy can now be empirically adjusted per DF by adjusting the scaling factor. This is not where the theoretical basis for the dispersion consideration resides, as the fundamental consideration is given in the dispersion coefficient C_6^{ij}. The dispersion coefficient C_6^{ij} was determined from a geometric mean of the form [78]:

$$C_6^{ij} = \sqrt{C_6^i C_6^j} \tag{2-44}$$

The C_6^i coefficient is derived from the London formula for dispersion and is based on the ionization potential I_p and static dipole polarizabilities α which gives a coefficient for an atom i as [78]:

$$C_6^i = 0.05 N I_p^i \alpha^i \tag{2-45}$$

Where N has a predetermined value for atoms within each row of the periodic table. This now gives a mathematically appropriate approximation for dispersion energies within a system and requires less empirical adjustment using fewer parameters. The accuracy obtained from this approach can be improved upon for weakly bonded van der Waals systems by the inclusion of a Becke-Johnson damping which reduces the mean absolute deviation from experimental work significantly for non-covalent interactions [80]. There is however a consideration that needs to be given to this approach. The system approximates non-covalent interactions when the atoms have a relatively small difference between the free atom and the atom bonding state well however, it tends to deviate for transition metals.

Transition metals have large discrepancies between their free atom and bonded states [78] and the approach to calculate C_6 becomes less robust. A simplification is often made by an average C_6 coefficient, typically calculated from the preceding rare gas and group III elements, which holds provided the number of metal atoms are substantially less than the total atoms within the system [78]. The simplification is therefore not valid when modelling a metallic surface as the metal atoms outnumber those of the adsorbates. The coefficient would then need to be determined for each metallic system from the molecular properties if the polarizability differs in the system from the free atom state, which can be seen in work done by Becke and Johnson [82]. It should however be noted that the development of this system focused on determining the dispersion of gaseous molecular systems and not catalyst surfaces.

In summary, this approach has a more mathematical consideration for van der Waals forces, but the correlation is still partially empirical providing reasonable approximations for short and medium range interatomic forces. The primary advantage can be taken as knowing where contributions to dispersion originate as the physical description is supported mathematically. The primary drawback though is the coefficient calculations required when dealing with a more polarizable system, particularly when transition metals are present in bulk, which need to be calculated for each adsorbate system. Including these calculations may not yield a fully optimized system as some elemental dispersion coefficient assumptions still need to be made [60], [80] which may not account for all potential dispersion interactions.

2.6.2. Adjusted functional-based dispersion correction

To potentially account for all possible dispersion interactions present on a surface, a more focused empirical approach can be used. This approach is done by modifying the model to describe the energies observed in experimentation. This follows a more top down approach working from the energy result down to the empirical parameters. In this section focus will be given to the work done by Hensley et al. [54] regarding the accuracy of widely used empirical van der Waals correlations and Klimes et al. [53], [60] which describe the correlation approach, although the discussion that follows will be less detailed than that given in their work.

The first step is to describe the desired London dispersion as an additive to the existing exchange correlation energy. A method for this is the non-local van der Waals density functional (vdW-DF) [53], [57] which describes the energy as:

$$E_{XC} = E_x^{GGA} + E_c^{LDA} + E_c^{nl} \qquad \text{2-46}$$

Where E_x^{GGA} is once again the GGA exchange energy, E_c^{LDA} is the local correlation energy from the local density approximation and E_c^{nl} is the non-local correlation energy. The non-local correlation energy is of interest here as it is based on the electron density calculated via a response functional [60]. The result of this is that the non-local correlation becomes sensitive to the model selection. The typical result however is often not considered accurate enough when comparing the calculated results to datasets, such as the S22 dataset [52], [83], yielding mean absolute deviations (MAD) as large as 60 meV [60]. The S22 dataset is a collection of small complexes, representing non-covalent interactions in common biological molecules and weak dimers [83]. This dataset serves as a benchmark for realistic calculation validation particularly for theoretical empirical methods or density functional based methods. In practice, an exchange correlation can be adjusted to reduce the MAD when compared to the S22 dataset which would give a better representation of an accurately modelled system.

An example of these adjustments can be seen in the optimized PBE (optPBE) and the optimized B88 (optB88) functional. The name optPBE/B88 implies that the PBE/B88 functional has been adapted to potentially include the van der Waals considerations mentioned earlier. These functionals are adjusted by considering the enhancement factor found in the GGA exchange energy density given as [53]:

$$\epsilon_x(n,s) = \epsilon_x^{LDA}(n)F_x(s) \tag{2-47}$$

Where $\epsilon_x^{LDA}(n)$ is the exchange energy density and $F_x(s)$ is the enhancement factor which is the same enhancement factor as the one described in Equation 2-11, but are repeated here for both optPBE and optB88 exchange correlation respectively [53]:

$$F_x^{optPBE}(s) = 1 + \kappa - \frac{\kappa}{1 + \frac{\mu s^2}{\kappa}} \tag{2-48}$$

$$F_x^{optB88}(s) = 1 + \frac{\mu s^2}{1 + \beta s \operatorname{arcsinh}(cs)} \tag{2-49}$$

In these enhancement factors the empirical values of κ, β and μ are adjusted to reduce the MAD from the S22 data set to as low as possible which results in the following values for the optPBE and optB88 [53]:

$\kappa^{optPBE} = 1.04804$, $\mu^{optPBE} = 0.175519$

$\mu^{optB88} = 0.22,$ $\beta = 0.22/1.2$, $c = 2^{\frac{4}{3}}(3\pi^2)^{\frac{1}{3}}$

These are empirical adjustments which reduce the MAD of the optPBE to 15 meV and the optB88 to 10 meV when compared to the S22 dataset [53]. The optB88 proves to be a better approximation than the former B88 which was shown to underestimate the binding of dimers which led to the adjustment, such that $\mu/\beta = 1.2$ [53]. It may be tempting to use the optB88 to model a catalyst system as it has been shown to accurately model the S22 dataset and will account for all possible interactions present. However, dimer sets are not fully representative of a surface catalyst system and consideration should first be given how these empirically adjusted models will represent an adsorption system, particularly with the adsorbates of interest, O and OH.

Hensley and colleagues [54] considered 39 surface based adsorption reactions on a variety of dominant catalyst surfaces, such as Ni(111)/(100), Au(111), Pt(111) and others. The adsorption energies for each surface reaction was calculated using an optimized surface model. They compared the results to experimental values so that a compelling argument could be given to modelling dispersion, such as van der Waals, in DFT. The 39 surface reactions were separated into two dominant categories with the first 25 reactions considered to be chemisorption systems, while the last 14 were considered strong van der Waals. Included in this sample set are [54]:

$$O_2 + Pt(111) \rightarrow 2O/Pt(111) \tag{2-50}$$

$$H_2O + Pt(111) \rightarrow H_2O/Pt(111) \tag{2-51}$$

These correspond to a comparatively weak van der Waals, (2-50), and strong van der Waals surface reaction, (2-51). As the system of interest in this study will focus on adsorbate combinations of O, OH and O/OH it is worth further analysing their findings. They calculated the mean signed error (MSE), mean absolute error (MAE) and root mean square error (RMSE) per molecule fragment created upon adsorption, which measure quantity, prediction and sample/population accuracies respectively. A selection of their findings applicable to this research is given in Figure 2-3.

In their work the optPBE model was not considered however, the RPBE model uses the same enhancement factor as optPBE, see Equation 2-28, but with κ = 1.245 [53]. For comparative purposes, the general trend reported for RPBE follows that of optPBE, which indicate that for chemisorption systems the selection of the optPBE yields more accurate results than the corresponding optB88, which over estimates the adsorption energy. Considering strong van der Waals contributions, the reverse is observed with optB88 more accurately representing adsorption of H_2O on Pt(111) while the optPBE would underestimate the adsorption. This illustrates now why the optB88 has been mentioned previously in our study, as when considering a system with more dominant OH coverage the optB88 would be the preferred model.

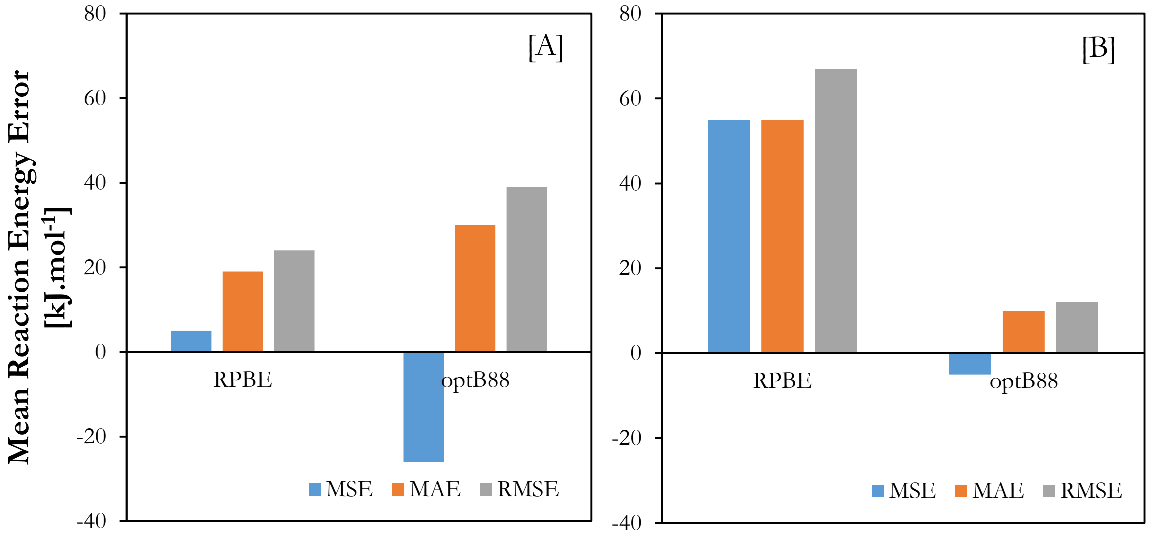

Figure 2-3: Accuracy of RPBE and optB88 functional relative to 39 adsorption reactions when compared to the experimental data set for [A] Chemisorption and [B] large van der Waals contributions with the relative mean signed error (MSE), mean absolute error (MAE) and root mean squared error (RMSE), adapted from the results obtained from Hensley et al. [54].

This highlights the drawback of a more empirical approach in that adjusting exchange-correlations results in a particular model representing a particular system accurately but at the cost of varied accuracies for other systems. This is further complicated when attempting to predict a more complex system when it becomes unclear what adsorbates are present on the surface and whether there will be a domination of chemisorption or van der Waals contributions. The effective choice for adsorption of O and OH on Pt, when accounting for dispersion, becomes a choice between the optPBE, which will underestimate OH adsorption energies, or optB88, which will overestimate the adsorption energies of O. A key advantage though is that in the more empirical approach which adsorption is being over/underestimated is known.

2.6.3. Contextualising the selection of a dispersion model

The approach to consider van der Waals in this research could either follow the embedded molecular dispersion, as done by Grimme [78], or a an adjusted functional-based dispersion approach, as done by Klimes et al. [53], [60]. The difficulty in approximating the interaction coefficients and assumptions required for transition metals in the embedded molecular approach would require calculations from elemental properties which may still be omitting some interactions. The resources to develop and implement this make the approach less desirable if the final result may not accurately represent a surface catalyst system, especially if experimental data is unavailable to check model accuracy. This reasoning leads us to instead focus on the more empirical approach of selecting an adjusted exchange correlation. This has the drawback of under or overestimating certain adsorptions but has the advantage of potentially accounting for all possible interactions with some guidance indicating which adsorptions are being over or underestimated.

There is still development within the model accuracy to account for dispersion van der Waals, particularly in the empirical approaches, with promising results being shown from a hybridized correlation. One such method is the sigmoid-weighted (SW) sum of the RPBE and optB88 referred to as the SW-R88 [54], which could in future predict both chemisorption and van der Waals dominant reactions along with the intermediates. However, as these models are still in development we will limit our selection in this research to the two models that have sufficient accuracy for our adsorbates, these models being those of the optPBE and optB88 for representing O_2 and H_2O adsorption respectively [54].

As will be illustrated, a dispersion model increases computational time and as a result it is not efficient to model multiple dispersion models simultaneously, instead a single dispersion model should be selected. In order to select between these models several parameters will be tested, such as preferred adsorption geometries, adsorption energies and bond lengths before a final model will be selected to represent the possible dispersion contributions in the system. The model selection will result in either over or underestimations of certain adsorption energies but it can at least be acknowledgement which adsorbate have altered energies. To appreciate the dispersion model and how it influences adsorption research this research will report on both the PBE and selected dispersion (optPBE/optB88) for comparative purposes.

3. MODEL OPTIMIZATION

3.1 Bulk platinum

In order to generate an accurate model, there needs to be a convergence within an acceptable accuracy criterion. This requires optimization of the basis set cut-off energy and the Monkhorst-Pack grid parameter. Utilizing a minimum kinetic cut-off energy will provide reasonable approximations while maintaining lower computational times. This also requires optimisation of the k-point system which is an application of Bloch Theorem that maps an infinite periodic system using symmetry [84] and if insufficient will inaccurately predict the total energy. As computational time increases with an increasing k-point density there needs to be a refinement in this parameter to prevent excessive computational times. Finally, the bulk lattice parameter needs to be optimised by minimizing the total energy and comparing to an experimental value to determine the models accuracy.

3.1.1. Optimization of basis set cut-off energy

The cut-off energy was optimized using a conventional face centred cubic platinum unit cell with a lattice parameter from literature sources of 3.924 Å [34], [36]. A large k-point grid of 16x16x16 (0.0157 $Å^{-1}$) was selected for all cut-off energy optimizations to ensure a sufficient number of irreducible k-points were accessible. Single point energy calculations were conducted based on the Methfessel-Paxton (MP) scheme with a smearing width of 0.1 eV with a convergence criteria desired of 1 meV.$atom^{-1}$. The results can be seen in Figure 3-1 which indicate that the energy of the cell converges after 400 eV. This cut-off energy is within the recommended VASP cut-off energy but substantially larger than previous studies which used cut-off energies of 300 eV and 340 eV [26], [35], [36] which used ultrasoft pseudopotentials that require lower cut-off energies.

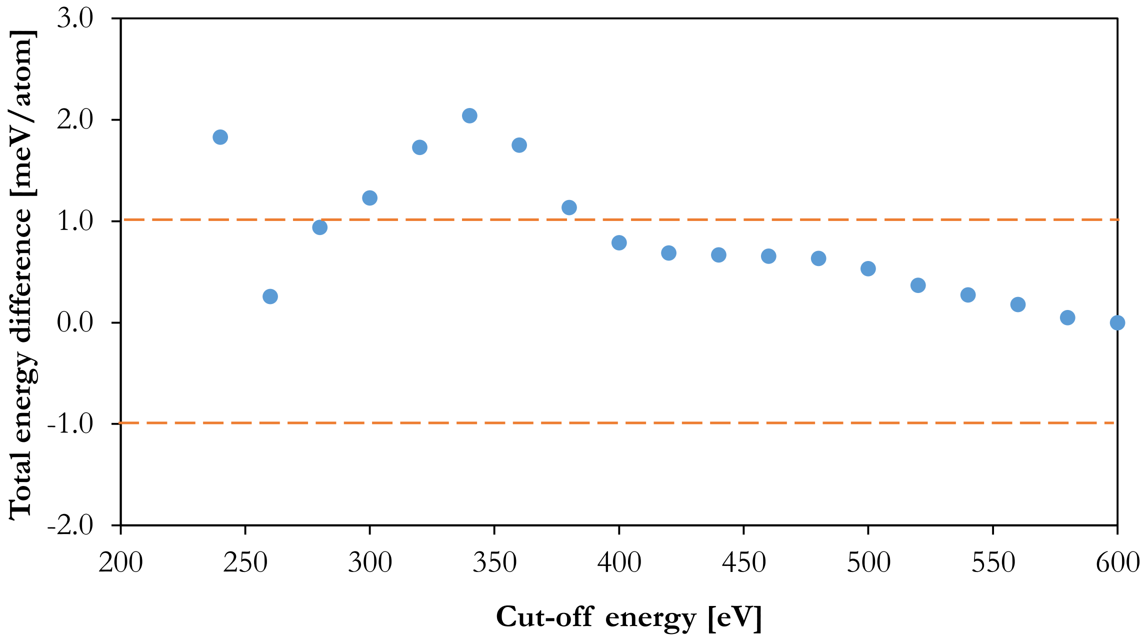

Figure 3-1: Convergence of total energy of conventional bulk platinum cell as a function of cut-off energy. The energy difference was determined with reference to the total energy at a cut-off energy of 600 eV using PAW-PBE. The dotted lines indicate the upper and lower convergence limit of 1 meV.$atom^{-1}$.

3.1.2. K-point optimization

The k-point sampling was optimized using the conventional unit cell for bulk platinum with the lattice parameter of 3.924 Å [34], [36]. The cut-off energy was set to 600 eV for the grid optimization to ensure a sufficient plane-wave basis for convergence. The single point calculations were performed using a smearing width of 0.1 eV. The results can be seen in Figure 3-2:

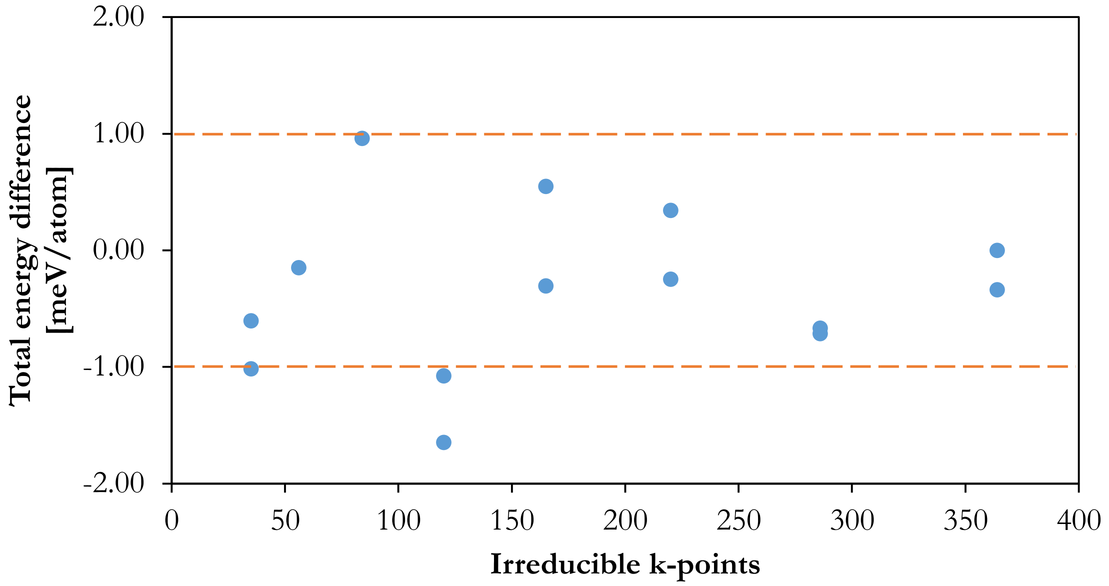

Figure 3-2: Convergence of total energy of bulk platinum as a function of the k-point grid. The energy difference is referenced to the energy of a 23x23x23 k-point grid (364 irreducible k-points). The dotted lines indicate the upper and lower limit convergence of 1 meV.atom^{-1}.

The results indicate that the total bulk platinum conventional unit cell is converged to within 1 meV for 120 irreducible k-points in a 14x14x14 k-point grid (0.0180 Å^{-1}).

3.1.3. Lattice optimization

Bulk platinum occurs in a face-centred cubic (fcc) crystal structure [30] as it forms a truncated octahedron during crystallite growth. Having determined the optimal k-point and cut-off energy the lattice parameters of the cell need to be determined to minimize the energies calculated. The conventional unit cell for bulk platinum can be seen in Figure 3-3*:*

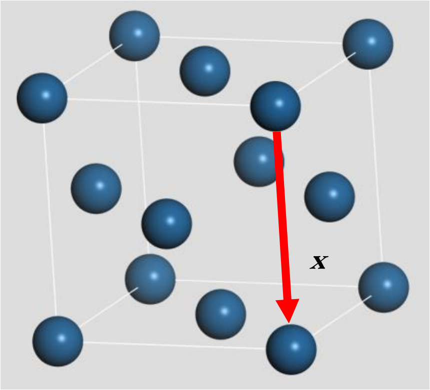

Figure 3-3: Conventional unit cell of bulk platinum with x representing the lattice parameter.

To determine the lattice parameter a non-spin polarized single point energy DFT calculation using VASP was performed. The lattice parameter was varied between 3.72 Å to 4.12 Å as this range comprises of an extended range for lattice parameters determined in other Pt model work [34], [36], [85]. The model lattice results, using the optimized 14x14x14 k-point grid with a cut-off energy of 400 eV, can be seen in Figure 3-4:

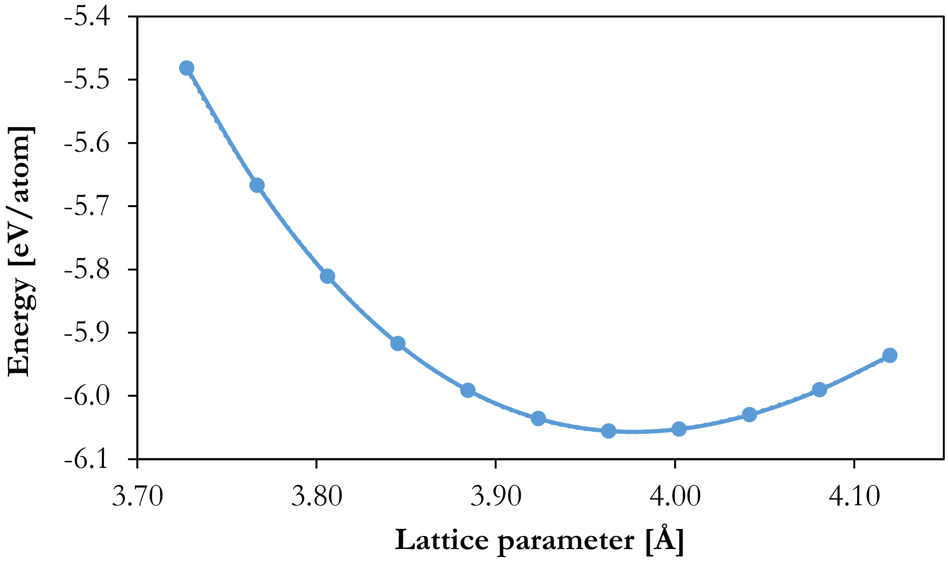

Figure 3-4: Bulk platinum lattice parameter optimization with regard to the total energy of each atom taken at across the lattice parameter range of 3.72 to 4.12 Å using a 14x14x14 k-point grid and a 400 eV cut-off energy.

The energy calculations yielded an optimal lattice parameter of 3.976 Å. This was found by fitting a third order polynomial to the curve of best fit and solving for the point where the first derivative reached zero. The optimized Pt lattice needs to be compared to an experimentally determined lattice parameter reported as 3.924 Å [26], [34]. The resulting lattice parameter, when compared to the experimental value, is 1.33 % larger than expected. This overestimated deviation between the simulated and experimental lattice parameter was reported by Perdew, Burke and Ernzerhof [55]. In their work they found that lattice parameters and bond lengths were typically overestimated by 1.23 % when using PAW-PBE. In their review letter they attribute the deviation in the lattice parameter to the empirical adjustment of κ. The PBE parameter optimizes the atom energies and covalent bonds but report binding properties lower than expected on crystalline lattice parameters and hydrogen bonds [55]. This results in the lattice parameter varying slightly from experimental values, which has also been reported in other model works [26], [36], [55].

In conclusion the model does converge with an acceptable accuracy for the total energy per atom to within 1 meV.atom^{-1} with a 3.976 Å which will form the base lattice parameter from this point onwards. In addition to optimizing the platinum lattice, the model must be able to effectively represent the gas phase specie references, given in Table 2-2 and Table 2-3, with regard to the bond lengths and bond angles.

3.2 Gas phase molecule

As mentioned in this study the molecular gases of interest are oxygen (O_2) and water (H_2O) as these form the reference states for the systems. The gases were modelled by placing the gas species in a rectangular vacuum box, with dimensions a = 13 Å, b = 12 Å, c = 14 Å, and allowed to relax.

The energy and force convergence were set to 10^{-5} eV and 0.01 eV.$Å^{-1}$ respectively. The cut-off energy was set to 400 eV with a k-point grid of 1x1x1 and a Gaussian smearing width of 0.01 eV. The vacuum structure model can be seen in Figure 3-5 and was used to calculate the energy of all gas phase molecules performed including spin-polarisation. A summary of the electronic energies and vibrations for O_2 and H_2O can be seen in Appendix C, Table C-2.

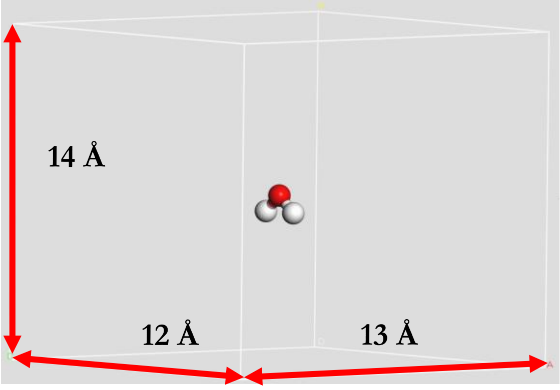

Figure 3-5: Rectangular vacuum box with centred water molecule using a 400 eV cut-off energy and a k-point grid of 1x1x1: Red – oxygen, White –hydrogen.

3.2.1. Oxygen

A relative indication to the accuracy to which a model can predict the gas phase molecules is to investigate the predicted model bond lengths. The calculated bond length for diatomic oxygen gas molecule was shown to be 1.234 Å using PAW-PBE with a vibration frequency of 1565 cm^{-1}. The calculation overestimated the bond length by 2.24 % when compared to experimental oxygen bond lengths of 1.21 Å [86]. The overestimation of the PAW-PBE method is within expected deviations as it has been reported by Ernzerhof [40] with the deviation in bond lengths typically 1.8 % - 2.3 % larger than experimentally determined. A similar trend can be seen for the dispersion correction models, PAW-optPBE and PAW-optB88, which are reported in Table 3-1:

Table 3-1: Bond length, DFT energy and bond length deviation from experimental for O_2 calculated in a vacuum box using 400 eV and a 1x1x1 k-point grid for PBE/optPBE/optB88.

	Bond Length [Å]	Bond Deviation [%]	E^{elec} [eV]
PBE	1.234	2.24	-9.83
optPBE	1.240	2.73	-8.47
optB88	1.234	2.24	-8.31
Experimental [86]	1.207	-	-

The overestimation of the bond length is again seen in the dispersion models, this is expected as these models are only empirical adjustments of the PBE and B88 models. It can be seen though that both models reasonably approximate the bond length in O_2. The energies obtained are similar to other DFT model work done containing oxygen species [26], [85] and as a result no model can be seen as being unable to predict O_2.

We further confirm the model approximation by looking at the orbital occupancy for PAW-PBE/optPBE/optB88. Oxygen has in its outer most shell 12 electrons with 2 unpaired electrons found in $2\pi^*$ orbital [77]. The results from each of the models selected yielded the same occupancy indicating 5 paired electrons with 2 unpaired electrons in the same spin orientation but different bands, see Table 3-2 to Table 3-4. The same occupancy can be seen for all three models and these follow with Pauli's exclusion principle in that each band has only two occupancies total. The only noticeable difference between each of the dispersion models and the non-dispersion model is the energy of the respective bands. The energy for the optB88 bands are consistently higher in energy than those of optPBE which is in turn lower in energy than the PBE model. This trend is expected as the inclusion of the enhancement factors has been shown to lower the relative calculated energies [54] and the optB88 has a larger enhancement correction than that of optPBE. Although the optB88 model has switched which spin component is present in the unpaired orbitals this has no effect on the energies calculated as spin-up and spin-down unpaired orientations are equivalent.

Table 3-2: Orbital occupancy (band) for O_2 using PAW - PBE with respective spin orientations.

Band	Energy [eV]	Spin component 1 [Occupancy]	Energy [eV]	Spin component 2 [Occupancy]
1	-32.54	1	-31.31	1
2	-20.68	1	-18.88	1
3	-13.44	1	-12.51	1
4	-13.29	1	-11.44	1
5	-13.28	1	-11.44	1
6	-6.97	1	-4.70	0
7	-6.97	1	-4.70	0

Table 3-3: Orbital occupancy (band) for O_2 using PAW - optPBE with respective spin orientations.

Band	Energy [eV]	Spin component 1 [Occupancy]	Energy [eV]	Spin component 2 [Occupancy]
1	-32.47	1	-31.26	1
2	-20.83	1	-19.11	1
3	-13.57	1	-12.65	1
4	-13.34	1	-11.57	1
5	-13.34	1	-11.57	1
6	-7.18	1	-5.01	0
7	-7.18	1	-5.01	0

Table 3-4: Orbital occupancy (band) for O_2 using PAW - optB88 with respective spin orientations.

Band	Energy [eV]	Spin component 1 [Occupancy]	Energy [eV]	Spin component 2 [Occupancy]
1	-31.24	1	-32.38	1
2	-18.78	1	-20.42	1
3	-12.75	1	-13.67	1
4	-11.77	1	-13.57	1
5	-11.77	1	-13.57	1
6	-5.08	0	-7.29	1
7	-5.08	0	-7.29	1

3.2.2. Water

The water molecule contains two important parameters for equilibrium calculations, the O-H bond length and the H-O-H bond angle. The calculated bond length for O-H in the water molecule for PAW-PBE was calculated to be 0.974 Å with a H-O-H bond angle of 104.6 ° and vibrations of 3818 cm^{-1}, 3699 cm^{-1}, and 1579 cm^{-1}. This corresponds closely to experimentally determined water properties of O-H bond length of 0.957 Å with a H-O-H bond angle of 104.5 ° [86]. The calculated bond lengths and bond angles for all the models including the dispersion models can be seen in Table 3-5:

Table 3-5: Bond length, bond angle, DFT energy and bond length deviation from experimental for H_2O calculated in a vacuum box using 400 eV and a 1x1x1 k-point grid.

	Bond Length [Å]	Bond Deviation [%]	Bond Angle [°]	E^{elec} [eV]
PBE	0.974	1.78	104.6	-13.88
optPBE	0.974	1.78	104.7	-13.67
optB88	0.974	1.78	104.8	-13.42
Experimental [86]	0.957	-	104.5	-

As seen the approximation of the geometry of water in all models is fairly consistent. This is an indication that all the models predict the same geometries in gas phase water molecules with only the final electronic energy changing, this follows with the prediction that the enhancement factor only primarily alter the total energy calculated. It can be seen once again there is a consistent over-estimation in the bond lengths which correspond to expected deviations for the same reasoning given for O_2.

As with oxygen the orbital occupancy for each model with regards to water was determined. In water the valence shell comprises of the combination of the 2s and 2p orbitals of O with the 1s orbitals of H, the resulting electron occupancy is 4 paired electrons [77]. In the case of water this 4 paired occupancies are predicted by PAW-PBE/optPBE/optB88 and follows the same trend as seen for O_2 with the energy of each orbital band lower in optB88 and highest when using PBE, see Table 3-6 to Table 3-8. The results of these orbital occupancies, combined with the orbital occupancies for O_2, indicate that any selected model will not generate inconsistent occupancy for any of the gas phase molecules.

Table 3-6: Orbital occupancy (band) for H_2O using PAW - PBE with respective spin orientations.

Band	Energy [eV]	Spin component 1 [Occupancy]	Energy [eV]	Spin component 2 [Occupancy]
1	-25.25	1	-25.25	1
2	-13.06	1	-13.06	1
3	-9.22	1	-9.22	1
4	-7.17	1	-7.17	1

Table 3-7: Orbital occupancy (band) for H_2O using PAW - optPBE with respective spin orientations.

Band	Energy [eV]	Spin component 1 [Occupancy]	Energy [eV]	Spin component 2 [Occupancy]
1	-25.36	1	-25.36	1
2	-13.21	1	-13.21	1
3	-9.38	1	-9.38	1
4	-7.32	1	-7.32	1

Table 3-8: Orbital occupancy (band) for H_2O using PAW - optB88 with respective spin orientations.

Band	Energy [eV]	Spin component 1 [Occupancy]	Energy [eV]	Spin component 2 [Occupancy]
1	-25.05	1	-25.05	1
2	-13.24	1	-13.24	1
3	-9.36	1	-9.36	1
4	-7.39	1	-7.39	1

4. SURFACE MODELS OF PLATINUM

4.1. Introduction

Prior to calculating the adsorption energies at different pressures and temperatures the dominant surfaces of the truncated octahedron need to be optimized to minimize the surface energy [30] and achieve a reasonably accurate model. To achieve this the dominant surfaces present, namely Pt(111) and Pt(100) [30], [33] terraces, were optimized to minimize the computational time while maintaining the desired energy convergence. As the primary focus of this study is the adsorption of O and OH, the slabs were optimized by converging the adsorption energy of O using a 0.25 ML coverage with O adsorbed in a hollow fcc site. This is the reported preferred adsorption site for O on Pt(111) [36], [38] but will be confirmed once the slab has been refined. The preferred adsorption of Pt(100) will be determined following its optimization. The slabs were optimized using PAW-PBE as this model yields accurate O_2 bond lengths and satisfies integrated bounds for any electron density in simple metal approximations [55] but the preferred adsorption sites were checked using both dispersion models to identify any discrepancies.

4.2. Pt(111) model optimisation

4.2.1. Slab thickness, vacuum spacing and relaxed layer optimization

Theoretically a perfect model surface would be represented by an infinite layered slab with an infinite vacuum. This is however not feasible as the computational time would become excessively large. It is not necessary though to develop an infinite slab, if we consider a (2x2) unit cell containing 24 (6 layers) and 28 atoms (7 layers) the converged adsorption energy difference between the two is less than 10 meV but each have a computational cost of 78 min.atom^{-1} and 83 min.atom^{-1} respectively, as will be shown. It is preferred then to refine the parameters to reach an acceptable energy convergence while minimizing the computational demands.

The first two parameters that contribute significantly to both computational time and energy convergence are the number of layers and the vacuum spacing present. The atomic layers were optimized using a Pt(111) – p(2x2) unit cell with an initial 14 Å vacuum spacing and a cut-off energy of 400 eV. The k-point grid was changed to a 10x10x1 grid which reflects a k-point spacing of 0.01778 Å^{-1}. First order Methfessel-Paxton (MP) method with a smearing width of 0.1 eV was used during optimisation. The convergence criteria chosen was O adsorption with the energy converged to less than 10 meV using an energy and force convergence set to 10^{-5} eV and 0.01 eV.Å^{-1} respectively. The adsorption energy for 0.25 ML O adsorption was calculated as:

$$E_{adsorption} = E_{Slab+adsorbate} - E_{clean\ slab} - \frac{1}{2}E_{Reference\ gas} \qquad 4\text{-}1$$

In order to optimize the number of atomic layers in the Pt(111) slab the number of layers was varied from 2 (8 Pt atoms) to 12 (48 Pt atoms) layers with the top two atomic layers relaxed. A representation of the slab optimisation model can be seen in Figure 4-1.

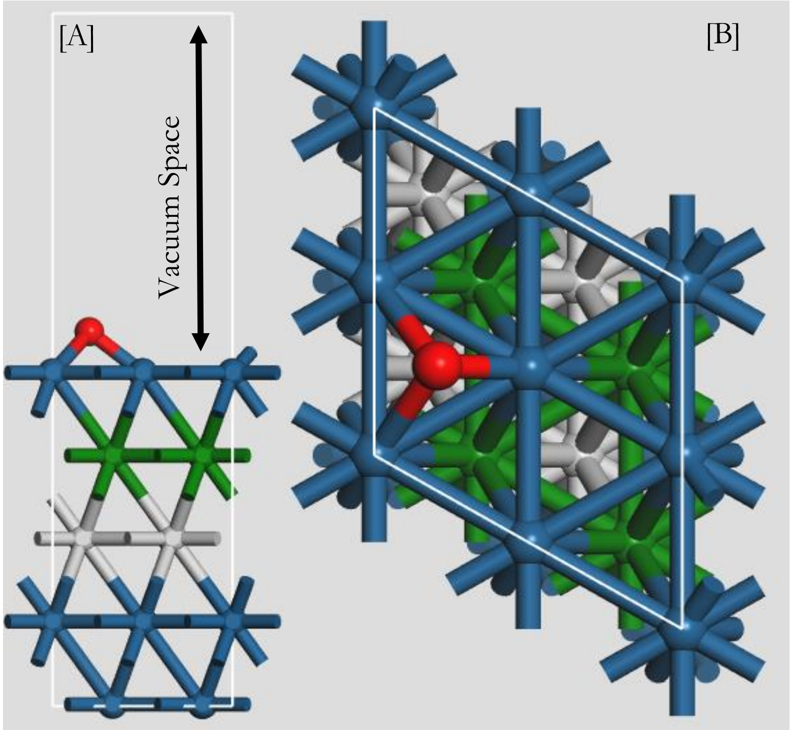

Figure 4-1: Pt(111) 5 layered slab with a 14 Å vacuum using a lattice parameter of 3.976 Å with O adsorbed in an fcc hollow, second and third Pt layer have been coloured green and silver: [A] – Side view, [B] –Top view.cc

By varying the number of atomic layers present the adsorption energies were calculated using Equation 4-2:

$$E_{adsorption} = E_{Pt(111)+O} - E_{clean\ Pt(111)\ slab} - \frac{1}{2}E_{O_2(g)} \qquad 4\text{-}2$$

Where $E_{Pt(111)+O}$ is the zero point energy of the slab with adsorbates present, $E_{clean\ Pt(111)\ slab}$ is the energy of the slab with no adsorbates and $E_{O_2(g)}$ is the energy of the gas components with the reference gas system based on the components shown in Table 2-2 for 0.25 ML. As a reference the adsorption energy was considered converged for a 12 layered slab as this is substantially larger, by 7 layers, than similar Pt DFT studies [26], [85]. The results of the adsorption energy can be seen in Figure 4-2 along with the desired convergence criteria. As can be seen in Figure 4-2 the adsorption energy oscillates as the atomic layers increase with the accuracy criteria of < 10 meV being met after a 5 layered (20 atoms) atomic slab was used. The computational time required to obtain the adsorption energies were also determined and plotted against the number of atoms present in the unit cell. Due to the increasing computational demand, which can reach 246 min/atom when considering a 49 atom, 48 Pt and 1 O, unit cell, selecting at least a 5 layered slab yields both a reasonably accurate adsorption energy while maintaining a computational time of 70.3 min/atom.

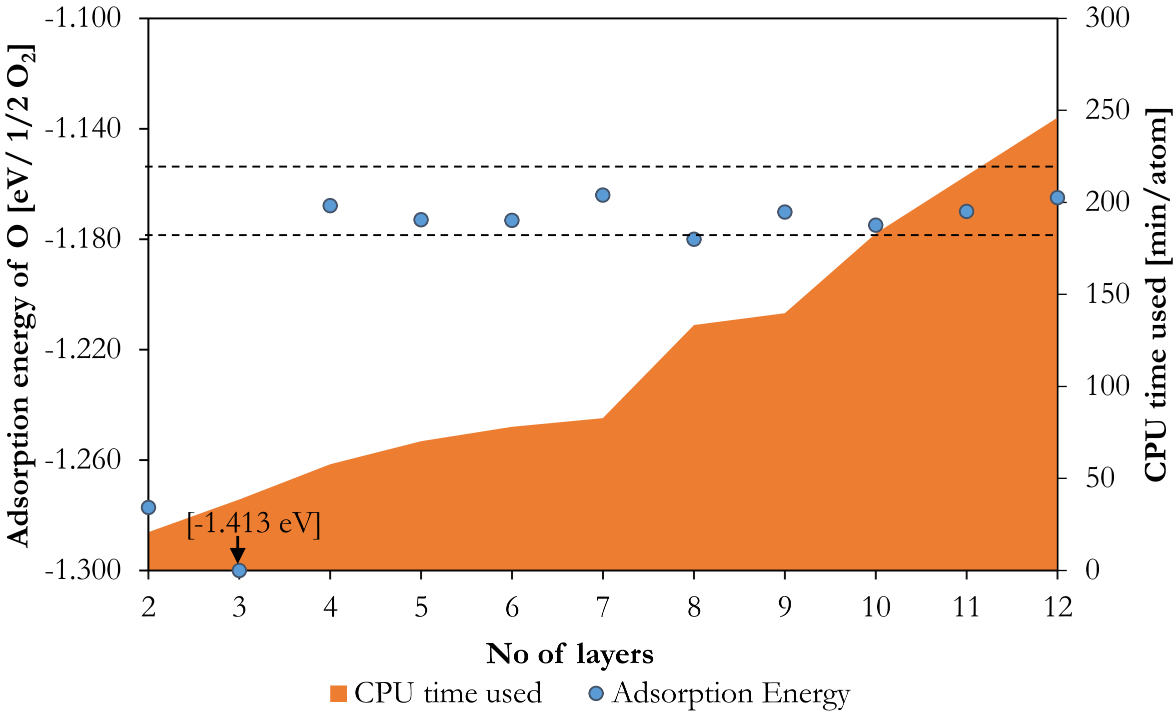

Figure 4-2: Adsorption energy of atomic O as a function of atomic layers on a Pt(111) - p(2x2) slab using a 14 Å vacuum space measured between 2 and 12 layers (4 to 48 Pt atoms with 1 adsorbed O atom) with the top 2 slab layers relaxed. The dotted line is ± 10 meV converged adsorption energy of O referenced to a 12-layer slab.

The next parameter optimized was that of the vacuum spacing using a 6 layered Pt(111) – p(2x2) with a k-point grid of 10x10x1 and a cut-off energy of 400 eV. The vacuum space was varied from 10 to 14 Å with a 20 Å vacuum space calculated as a converged energy reference point, this tests typical vacuum spaces used in Pt theoretical studies of 10 and 12 Å [26], [85]. The results of the vacuum space can be seen in Figure 4-3.

The relative adsorption energy difference between a 10 Å vacuum and a 20 Å vacuum is less than 1 meV and as a result there is no significant convergence improvement as the vacuum space is increased. There is however a strong increase in computational time. To minimize this, a vacuum space over 10 Å would not be advisable, as seen in Figure 4-3. This conforms with other DFT studies involving Pt adsorption which typically use lower vacuum spacing around 10 Å. Considering this result with that of the layer optimization it can be seen that a reliable model for Pt(111) would correspond to a 5 layered slab with a 10 Å vacuum spacing as this minimizes computational time while maintaining calculation accuracy.

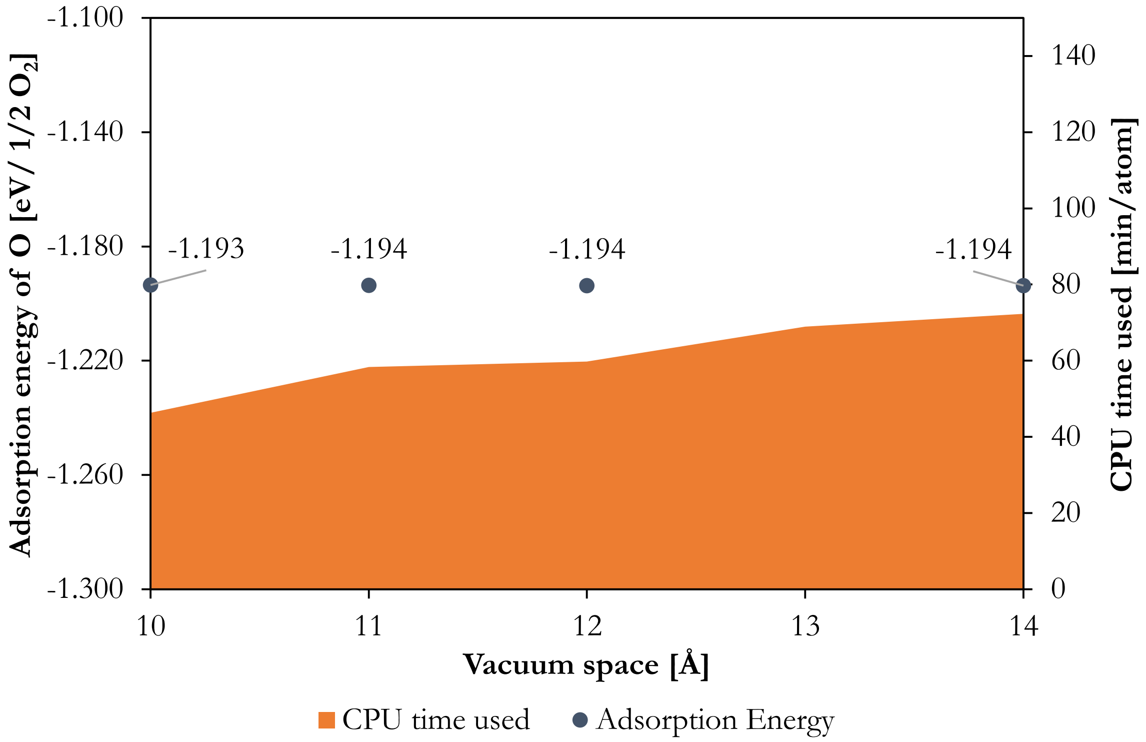

Figure 4-3: Adsorption energy of atomic O as a function of vacuum spacing on a Pt(111) - p(2x2) using a 6 layered slab with the top 2 layers relaxed using a 400 eV cut-off energy and a 10x10x1 k-point grid. Converged energy calculated at 20 Å $E_{adsorption}$ = - 1.194 eV.

An additional criterion to be considered in an optimised cell is the number of layers allowed to relax in the system. Additional relaxed layers increase the number of free moving atoms which require convergence during the geometry optimisation, increasing computational time, but may not change the relative adsorption energy. In this study the number of relaxed atomic layers was tested to achieve an adsorption energy convergence of less than 10 meV. This was done using a 5 layered Pt(111)-p(2x2) surface with a 10 Å vacuum with an fcc adsorbed O species using a 10x10x1 k-point grid over a range of 2 to 4 relaxed top layers, keeping all other layers fixed. The results can be seen in Table 4-1:

Table 4-1: Effect on the energy upon adsorption of O on a 5 layered Pt(111)-p(2x2) surface relaxing 2 to 4 layers using 400 eV with a 10x10x1 k-point grid and a 10 Å vacuum.

Number of Relaxed layers (relaxed Pt atoms)	$\Delta E^{*}_{adsorption}$ [eV/ ½ O_2]	$\Delta E^{**}_{difference}$ [meV/ ½ O_2]	CPU time used [min/atom]
2 (8)	-1.173	-	54.6
3 (12)	-1.173	0	57.8
4 (16)	-1.178	-5	59.9

* $E_{adsorbed\ slab} - E_{clean\ slab} - E_{gas\ reference}$

** Taken with reference to 2 relaxed layers

The number of relaxed slabs tends to have no significant effect on the adsorption energy, in order to minimise the computational time a 2 relaxed layer system was selected which agrees with other model work that use 0-2 relaxed layers [26], [41]. The choice to maintain at least 2 relaxed layers is to allow for any observations on surface deformation that could occur, which may not have a significant adsorption energy effect but could change the preferred adsorption site.

4.2.2. Adsorption site preference for O-containing species

4.2.2.1. PAW-PBE model

The adsorption site of each adsorbate needs to be determined to ensure that we achieve a minimal adsorption energy and to identify the most likely initial starting geometries for testing at higher coverages. In order to determine the preferred adsorption site, the energy for each adsorbate was investigated by placing the adsorbate in the fcc, hcp, bridge and atop sites which are then allowed to relax to their lowest energy position. This was performed using the optimized 5 layered Pt(111)-(2x2) slab with the top two layers relaxed using a cut-off energy of 400 eV and a k-point grid of 10x10x1 with a 10 Å vacuum. The initial starting positions for each adsorbate can be seen in Figure 4-4 and the final energy in each site given in Table 4-2:

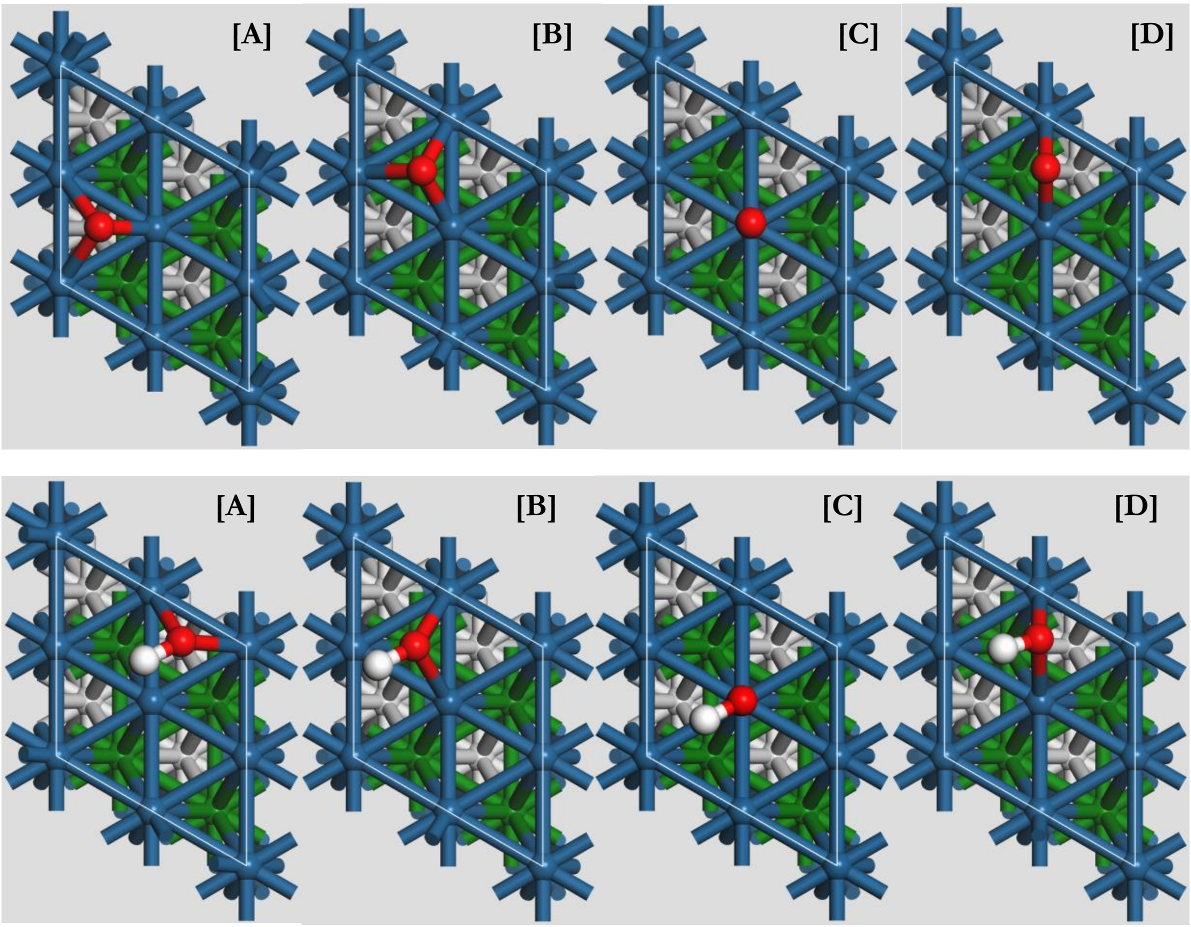

Figure 4-4: Initial adsorption geometry, for the preferred adsorbate adsorption site on the Pt(111) surface testing: A - fcc, B - hcp, C - atop and D – bridge with Pt – blue/green/silver, O – red and H - white.

The geometry optimization and vibrational analysis indicates that O adsorbed on the bridge and atop sites tend to fall into the fcc hollow indicating these 2 sites are unstable. In the case of OH, adsorption on fcc and hcp adsorption tends to move towards the bridge site and are therefore not stable adsorption sites. The preferred adsorption site for O can be taken as the fcc site while for

OH the site corresponds to atop adsorption as these provide the lowest adsorption energies, conforming with what was seen in similar DFT studies [26], [27], [85] and experimental work [41]. To ensure these were stable adsorptions a vibrational analysis was performed and each adsorbate was found to have real vibrations reported in Table 4-3.

Table 4-2: Adsorption energy for optimized geometry for stable O and OH adsorption sites on Pt(111) using PAW-PBE with preferred sites illustrated in bold.

	Adsorption energy [eV]			
Adsorption Site	fcc	hcp	atop	bridge
O	**- 1.18**	- 0.75	-	-
OH	-	-	**- 0.59**	- 0.57

Table 4-3: Vibrations for Pt(111) O - fcc and OH - atop adsorption.

Vibration	1	2	3	4	5	6
O [cm^{-1}]	450	370	369	-	-	-
OH [cm^{-1}]	3644	920	518	156	107	81

The values can be compared to EELS experimental values for O and OH [66] which yielded Pt – O stretching for atomic oxygen of 490 cm^{-1}, corresponding to the 1st vibration of O – fcc, and broad O-H stretching frequencies around 3476 cm^{-1} [41], corresponding to the 1st vibration of OH – atop. It should be noted that the EELS O-H stretching was found on a near full monolayer covered Pt(111) while our O-H reported here is for 0.25 ML and tends to be slightly overestimated using the PBE model.

4.2.2.2. Dispersion models

The method used to determine the adsorption sites was repeated using PAW-optPBE and PAW-optB88 using the same optimised slab as before. In these cases, the geometry optimizations were repeated using the new models starting from the same initial positions as for the PAW-PBE. The preferred adsorption sites were found to remain unchanged for both components, when compared to the PBE model, with the optPBE and optB88 only changing the total energy. This could have been expected as the enhancement factor functions as an empirical adjustment to the energy and not the calculation method. The results for the total energy and vibrational frequencies can be seen in Table 4-4.

Table 4-4: Total energy and vibrations for the optimized geometries for O - fcc and OH - atop adsorption sites using optPBE and optB88.

		Vibration [cm^{-1}]					
Adsorbate - *model*	Adsorption energy [eV]	1	2	3	4	5	6
O-*optPBE*	-1.30	446	364	364	-	-	-
O-*optB88*	-1.43	455	380	380	-	-	-
OH-*optPBE*	-0.62	3545	739	709	368	198	191
OH-*optB88*	-0.81	3558	745	704	382	215	187

A similar trend, as observed for the gas components, is seen in the model approximation of the adsorption sites, the total energy is shifted by an amount attributed to the enchantment factor with optB88 predicting lower energies (stronger adsorption) than optPBE. In comparison to the PBE model both optPBE and optB88 tend to have closer vibrational approximations to experimental for O-H stretching. In addition, there is no substantial shift in the vibrational analysis between the two dispersion models that would indicate a preference for one dispersion model over another, as the frequencies correspond well with the experimental values.

An important consideration to each of these dispersion models is how these models affect our effective computational speed. To identify this effect the number of electronic energy self-consistent field (SCF) iterations required to reach convergence, and the average time taken per iteration, were obtained and referenced relative to the PBE model which can be seen in Table 4-5:

Table 4-5: Computational demands of the dispersion models relative to the PAW-PBE model using a 5 layered Pt slab with an adsorbate present in a 10 Å vacuum using 400 eV cut-off energy and a 10x10x1 k-point grid.

Model used	Relative number of SCF iterations	Relative CPU time
PBE	1	1
optPBE	9	1.6
optB88	13	2.0

For the same system an optPBE model requires significantly more convergence iterations, 9 times more, with a relative time increase of 60 % compared to the PBE model. The time is further increased when considering the optB88 which effectively requires twice the computational time per iteration, with 13 times as many iterations required, while still yielding the same final geometry. This highlights a potential route for optimizing computational time when using a dispersion model by first optimizing with the non-dispersion model (PBE) and then calculate the energy using the final geometry with the dispersion model (optPBE/optB88).

4.2.3. Higher coverage adsorbate configuration and co-adsorption

The preferred adsorption sites have been identified for Pt(111) at 0.25 ML but as the coverage increases there are multiple preferred adsorption sites available for co-adsorption. Considering 0.50 ML coverage in a 2x2 cell with O and OH, atomic O can adsorb in the fcc site adjacent to the atop OH adsorption or in the non-adjacent fcc site illustrate in Figure 4-5.

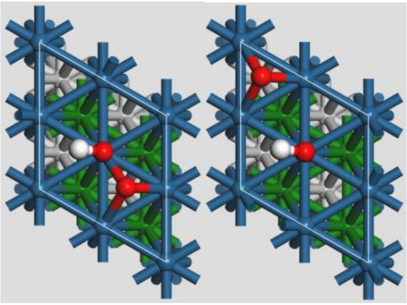

Figure 4-5: Co-adsorption 0.50 ML coverage on P(111) - p(2x2) with O and OH illustrating O-fcc adjacent (left) and O-fcc non adjacent (right) adsorption.

In this research we are focusing on the dominant adsorption configurations on the surface, these are the surfaces which result in the lowest Gibbs free energy upon adsorption. This requires testing all possible adsorption configurations on the surface using the reference gases, see Table 2-2 and Table 2-3, to determine the lowest energy upon adsorption. Due to the symmetry in a recurring slab model it is only worth testing individual unique adsorption locations, taking into account the preferred adsorption sites determined earlier. As the coverages being investigated in this research include 0.25, 0.50, 0.75 and 1.00 ML with O, OH and O/OH co-adsorption there were 22 unique possible unique geometries on the Pt(111) – p(2x2) surface.

In this section we will only illustrate lowest energy final geometries for the 14 adsorbate stoichiometries given in Table 2-2 and Table 2-3, for all unique initial geometries tested along with the electronic energies see Appendix . Each geometry was optimised using all 3 models; PBE, optPBE and optB88, and it was observed that the lowest energy geometry was the same for all models with all three models giving identical bond lengths and angles, with the values for PBE given in Figure 4-6 and Figure 4-7. In order to analyse these geometries we will consider several physical dimensions on the surface namely: the shortest adsorption distance (A), the distance between two surface Pt atoms (S), an interlayer distance (L), distance between adjacent adsorbates (D), hydrogen bond length (B) and the OH bond angle (°). The choice of reporting a layer distance is to highlight observed deformations between the surface and second Pt layer.

Adsorption of O on Pt(111), Figure 4-6, tends to have several geometry effects on the surface. When considering the adsorption distance (A) the shortest and longest observed bond distances were 2.034 to 2.050 Å taken at 0.50 ML and 1.00 ML respectively. The lowest adsorption length, seen at 0.50 ML coverage, conforms with the saturation coverage of O at 0.50 ML where we would expect the closest bond lengths, as this reflects strong adsorbate-surface interactions. As the coverage of O increases on the surface we can observe the repulsive interactions of O by the increasing inter adsorbate distance (D), from 0.50 Å to 0.75 ML by 0.015 Å (adsorbates moving away from each other). At 1.00 ML it may seem as if there is an attractive interaction but this is not the case, the reason for the closer distances is due to crowding on the surface. To compensate for the increased O specie coverage, the adsorbates have position themselves equidistant from each other which results in apparent closer distances than that of 0.75 ML.

The restructuring of the catalyst surface can also be seen by looking at the interlayer distance (L) and the surface distance (S). The inter layer distance (L) compresses as more O is adsorbed onto the surface, when compared to 0.25 ML, this follows with what is expected for O adsorption due to the high electronegativity of O causing the top Pt layer to compensate by encroaching on the second layer. This effect increases as more O is adsorbed onto the surface as (L) decreases by 0.165 Å at 1.00 ML, compared to 0.25 ML. Looking at the surface distances (S) Pt atoms are drawn towards the high electronegative oxygen adsorption, we can see that adsorbing 0.50 ML O tends to draw the centre Pt atom closer to the adsorbed pair by 0.017 Å. Increasing the coverage further to 0.75 ML as the centre Pt atom is drawn more towards the centre of the unit cell by 0.096 Å. At 1.00 ML coverage the central Pt atom has been placed in the centre of the 4O adsorbates with (S) equal to 2.811 Å.

In summary we can say that increasing the coverage of O on Pt(111) tends to have a compressive effect on the top layer with only a slight surface deformation, seen around 0.25 and 0.50 ML coverage due to the high electronegativity of O of 3.44 [77]. Increasing coverage of O tends to force adsorbates to place themselves as far away from other O adsorbates reaching equidistance placement on the Pt(111) surface at 1.00 ML.

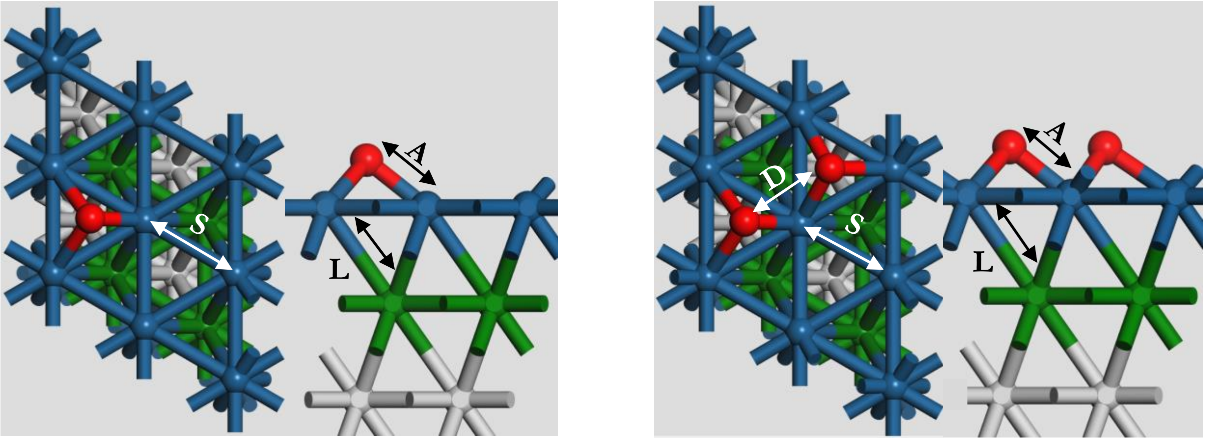

0.25 ML - O

Adsorption length (A)	2.049 Å
Surface distance (S)	2.724 Å
Layer distance (L)	2.907 Å

0.50 ML – 2O

Adsorption length (A)	2.034 Å
Surface distance (S)	2.707 Å
Layer distance (L)	2.839 Å
Adsorbate distance (D)	2.811 Å

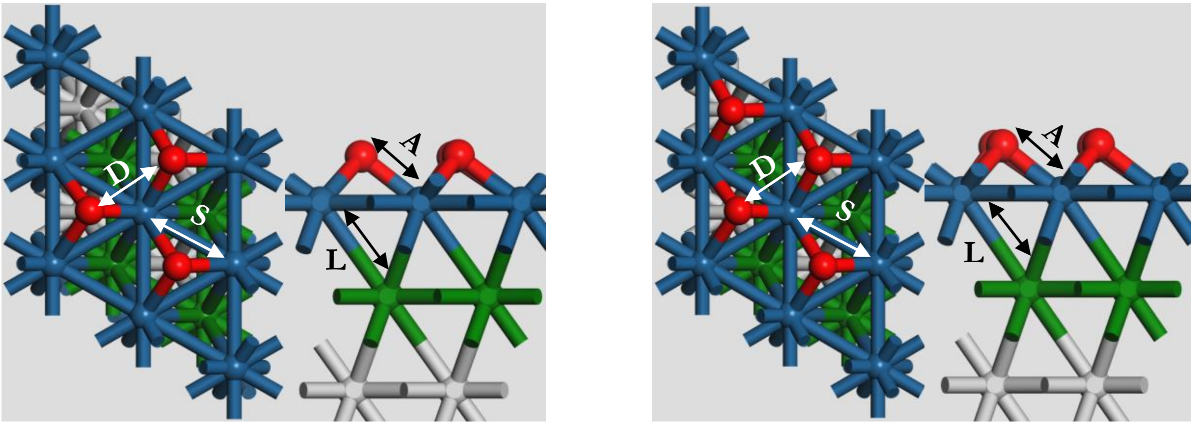

0.75 ML - 3O

Adsorption length (A)	2.037 Å
Surface distance (S)	2.813 Å
Layer distance (L)	2.775 Å
Adsorbate distance (D)	2.826 Å

1.00 ML – 4O

Adsorption length (A)	2.050 Å
Surface distance (S)	2.811 Å
Layer distance (L)	2.742 Å
Adsorbate distance (D)	2.811 Å

Figure 4-6: Optimized geometries on Pt(111) - p(2x2) for O using a 5 layered slab with 2 relaxed layers using a cut-off energy of 400 eV with a 10 Å vacuum and a 10x10x1 k-point grid with a top view and side view illustrated.

The next adsorbate geometries to be reported and analysed is that of OH on Pt(111). There are some similar trends observed to that of O adsorption although, the orientations of the H atom causes some interesting formations on the surface which will be easier to discuss after viewing the final geometries on the surface, see Figure 4-7.

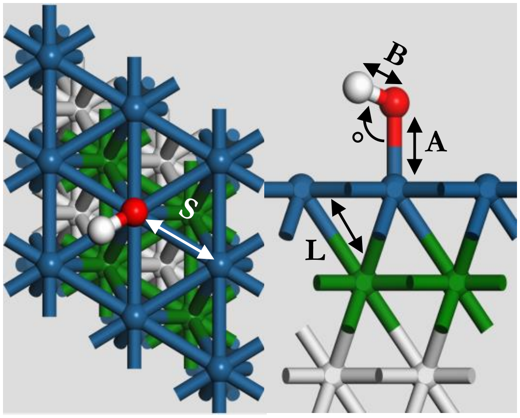

0.25 ML - OH

Adsorption length (A)	1.992 Å
Hydrogen bond (B)	0.980 Å
Surface distance (S)	2.813 Å
Layer distance (L)	2.784 Å
Bond angle (°)	106.4 °

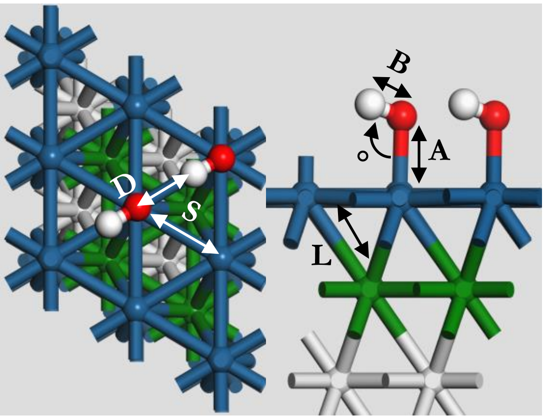

0.50 ML – 2OH

Adsorption length (A)	1.994 Å
Hydrogen bond (B)	0.992 Å
Surface distance (S)	2.816 Å
Layer distance (L)	2.868 Å
Adsorbate distance (D)	1.891 Å
Bond angle (°)	106.4 °

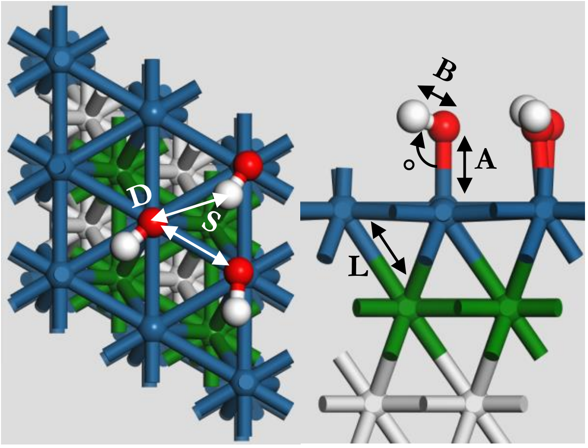

0.75 ML - 3OH

Adsorption length (A)	1.973 Å
Hydrogen bond (B)	0.998 Å
Surface distance (S)	2.815 Å
Layer distance (L)	2.813 Å
Adsorbate distance (D)	2.156 Å
Bond angle (°)	105.8 °

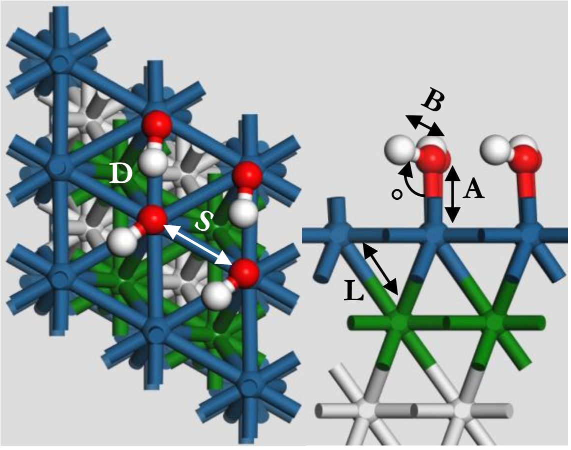

1.00 ML – 4OH

Adsorption length (A)	1.982 Å
Hydrogen bond (B)	1.003 Å
Surface distance (S)	2.811 Å
Layer distance (L)	2.751 Å
Adsorbate distance (D)	1.773 Å
Bond angle (°)	105.2 °

Figure 4-7: Optimized geometries on Pt(111) - p(2x2) for OH using a 5 layered slab with 2 relaxed layers using a cut-off energy of 400 eV with a 10 Å vacuum and a 10x10x1 k-point grid with a top view and side view illustrated.

Due to the top adsorption site preference of OH there is far less surface deformation seen, in that (S) tends to remain relatively unchanged as the coverage of OH is increased on Pt(111). There is also less of a compressive effect on (L) when compared to O, this is expected due to the atop adsorption and O-H bond lessening the electronegativity effect that O has on the surface. The adsorbate bond length (A) tends to be reduced on the Pt(111) surface for high coverage, 0.75 ML and 1.00 ML, with the lowest bond length seen at 0.75 ML of 1.973 Å which corresponds to the saturation coverage seen on Pt(111) of 0.75 ML [41]. In addition the 0.25 ML bond length agrees with similar experimental work reporting low coverage (0.25 ML) bond lengths of 2.001 Å [87].

The Pt-O-H bond angle (°) tends to agree with similar theoretical angles of 104 ° [36], [41], [87]. It can be seen though that the angle tends to drop as the coverage increases and the hydrogen atom tends to position itself between the adsorbed O species. This observation is supported by the hydrogen bond distance (B). At 0.25 ML the hydrogen bond distance is reported as 0.980 Å, which agrees with similar studies which reported 0.981 Å [36], [87]. At 0.50 ML the hydrogen bond distance has increased by 0.012 Å, an effect which is heightened at 1.00 ML with an increase of 0.023 Å, when compared to 0.25 ML. The tendency for the H atom to bend towards the next nearest neighbour O adsorbate is the cause for this increasing hydrogen bond length as it is a form of stabilization. At coverage of 0.75 ML and 1.00 ML there is a possible appearance of the stabilizing honeycomb structure of OH reported in literature [41] although, this cannot be confirmed with a p(2x2) cell. At 0.75 ML the H atom has placed itself directly between the next two adsorbed O species, placing itself directly over the hollow site. Due to the non-linear orientation of hydrogen on over the hollow site at 0.75 ML the inter adsorbate distance is increased by 0.256 Å, when compared to 0.50 ML. At 1.00 ML however, the inter adsorbate distance drops by 0.118 Å due to the linear orientation of the H atom over the bridge site.

In summary it can be said that increasing OH coverage on Pt(111) tends to have less deformation of the surface than single O adsorption although, there is still some compression of the top layer towards the second layer. There is however, deformation of the OH adsorbates as coverage increases, particularly for the O-H bond distance (B) and inter adsorbate distance (D). Increasing the coverage causes the H atom to tend to position itself closer to the next nearest adsorbed O by increaseing (B) while reducing (D), reorienting itself to be between two adsorbed O species at 0.50 and 1.00 ML. At 0.75 ML the hydrogen places itself over the hollow site to give the shortest distance between both nearest O species as these are equidistant from the hydrogen upon adsorption.

Overall for single specie adsorbate geometries, only O or OH present, the surface tends to undergo limited deformation and adsorbates tend to remain in their preferred adsorption site, either fcc or top site. When specifically considering OH adsorption it can be seen that there is a tendency for hydrogen to tilt towards the next nearest oxygen, this result mirrors that observed in experimentation of the possible formation of OH islands and/or honeycomb ring structures.

When considering co-adsorption there tends to be more significantly altered geometries and surface deformations, see Figure 4-8. Due to the different adsorbates on a co-adsorbed surface the definitions of our reported values needs to be further refined; the inter adsorbate distance (D) reported will focus primarily on the distance of the hydrogen to the nearest O neighbour, to serve as an indication to potential hydrogen bonding. The layer distance (L) will primarily focus on the distances linked to the surface centred Pt atom while the adsorption distance (A) will still be the distance to the closest Pt atom.

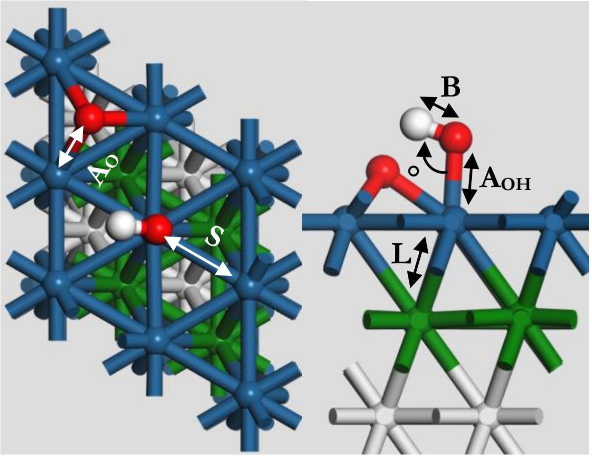

0.50 ML – O/OH

Adsorption length (A_O)	2.048 Å
Adsorption length (A_{OH})	1.994 Å
Hydrogen bond (B)	0.980 Å
Surface distance (S)	2.820 Å
Layer distance (L)	2.832 Å
Bond angle (°)	107.3 °

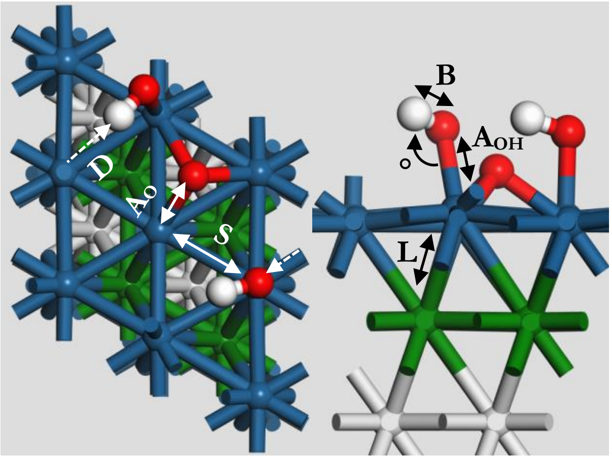

0.75 ML – O/2OH

Adsorption length (A_O)	2.020 Å
Adsorption length (A_{OH})	2.023 Å
Hydrogen bond (B)	0.992 Å
Surface distance (S)	2.816 Å
Layer distance (L)	2.697 Å
Adsorbate distance (D)	1.983 Å
Bond angle (°)	102.7 °

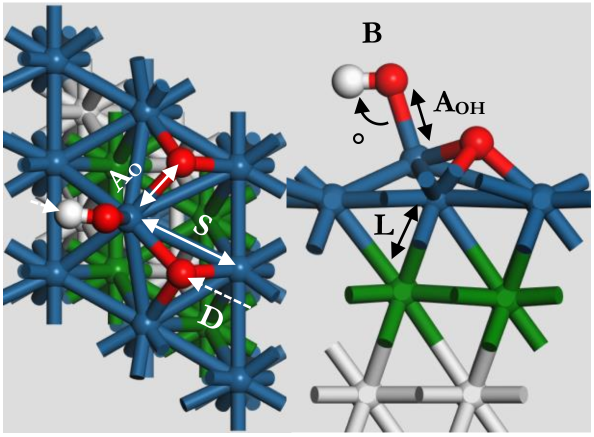

0.75 ML – 2O/OH

Adsorption length (A_O)	2.068 Å
Adsorption length (A_{OH})	1.986 Å
Hydrogen bond (B)	0.983 Å
Surface distance (S)	3.330 Å
Layer distance (L)	3.359 Å
Adsorbate distance (D)	2.684 Å
Bond angle (°)	106.0 °

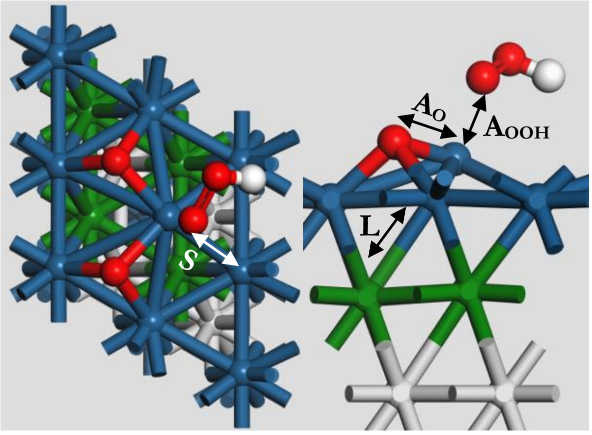

1.00 ML –3O/OH – 2O/OOH

Adsorption length (A_O)	2.097 Å
Adsorption length (A_{OOH})	2.026 Å
Surface distance (S)	2.634 Å
Layer distance (L)	3.408 Å

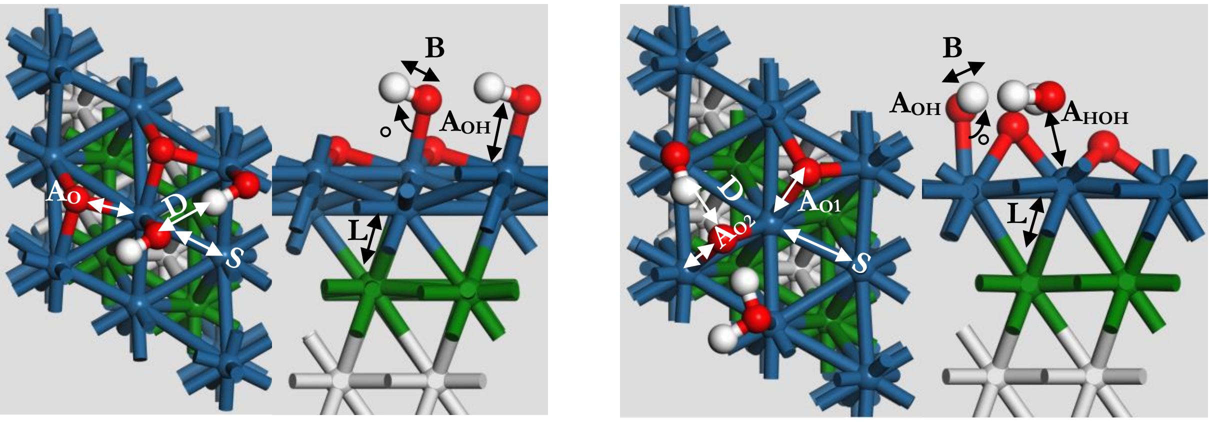

1.00 ML – 2O/2OH

Adsorption length (A_{O})	2.056 Å
Adsorption length (A_{OH})	2.003 Å
Hydrogen bond (B)	0.992 Å
Surface distance (S)	2.681 Å
Layer distance (L)	3.241 Å
Adsorbate distance (D)	1.894 Å
Bond angle (°)	104.6 °

1.00 ML –O/3OH – 2O/OH/H_2O

Adsorption length (A_{O1})	1.987 Å
Adsorption length (A_{O2})	2.044 Å
Adsorption length (A_{OH})	2.042 Å
Adsorption length (A_{HOH})	2.161 Å
Hydrogen bond (B)	0.992 Å
Surface distance (S)	3.026 Å
Layer distance (L)	2.738 Å
Adsorbate distance (D)	1.783 Å
Bond angle (°)	99.0 °

Figure 4-8: Optimized geometries on Pt(111) - p(2x2) for O/OH co-adsorption using 5 layered slab with 2 relaxed layers using a cut-off energy of 400 eV with a 10 Å vacuum and a 10x10x1 k-point grid with top and side views illustrated.

When considering co-adsorption there tends to be more severe deformation on the Pt surface. This can be observed by considering the surface distance (S) and layer distance (L). However, at 0.50 ML there appears to be no major surface deformation. This is most likely due distance of the fcc O adsorbate and the atop OH adsorbate limiting interactions. Once coverage reaches 0.75 ML the surface begins to experience larger deformation than in the single species case. Considering 2O/OH the layer distance increases for the centre Pt atom by 0.527 Å while the surface distance increases by 0.510 Å. This surface deformation can also be observed at 1.00 ML with O/3OH, 2O/2OH and 3O/OH. When compared to single species adsorption, Figure 4-6 and Figure 4-7, the degree to which the surface has restructured is heightened with the largest deformation in single species adsorption decreasing the layer distance to 2.742 Å (O adsorption), while in co-adsorption the layer has increased to 3.359 Å. The total surface compression between the single species adsorption layer was thus 0.140 Å (difference between highest and lowest (L) in O or OH adsorption) while with co-adsorption the surface decompression was 0.662 Å (difference between 2O/OH and O/2OH).

In addition to the observable surface deformations present during co-adsorption there is also new species formation. When exposed to O/3OH the surface tends towards forming H_2O, 2.161 Å above the surface, leaving the surface with a 0.75 ML coverage with 2O/OH. An interesting observation here is that the adsorption location of one O species has shifted to bridge adsorption, with a bond length of 2.004 Å due to the species formation. When the surface is exposed to

3O/OH there is a tendency to instead form OOH, 2.026 Å above the surface. This leaves the surface at 0.50 ML coverage with 2O species adsorbed in the lowest energy configuration seen for single adsorption of 2O. In summary, we can say that when there is excessive OH adsorbed onto the surface in the presence of O the Pt(111) surface tends to form H_2O, when we reach high coverages of O in the presence of OH then the surface tends to form OOH.

These 14 geometries (8 single species adsorbates and 6 co-adsorbed) form the lowest energy formations on the surface giving the final geometries the surface will tend towards as coverage increases. As temperature and pressure are varied so will the preferred coverage and these are the possible surface formations that can be expect on the Pt(111) surface, which will be used to generate the phase diagram for Pt(111). However, it should be noted that the co-adsorption lowest energy geometries were obtained by optimising O and OH starting in the lowest energy (0.25 ML) preferred adsorption sites, namely fcc site and top site. There may exist lower energy co-adsorption configurations for O and OH in different adsorption sites not tested in this study. The electronic energies for each of these adsorptions, relative to reactions given in Table 2-2 and Table 2-3, are given in Table 4-6. As has been mentioned the geometries for the dispersion models did not vary but as the energies did alter the optB88 adsorption energy results have been included in the adsorption table to illustrate the increased stabilisation estimated by dispersion models.

Table 4-6: Adsorption energy, including zero point energy contributions, for the lowest configuration on a Pt(111) surface for PBE/optB88.

Coverage [ML]	Adsorbates	$E^{elec}_{adsorption}$ (PBE) [eV]	$E^{elec}_{adsorption}$ (optB88) [eV]
0.25	O	-1.18	-1.43
	OH	-0.59	-0.81
0.50	2O	-1.78	-2.27
	2OH	-1.56	-1.94
	O/OH	-1.75	-2.21
0.75	3O	-1.55	-2.29
	3OH	-2.21	-2.83
	2O/OH	-1.70	-2.42
	O/2OH	-2.02	-2.69
1.00	4O	-0.57	-1.58
	4OH	-3.12	-4.03
	O/3OH	-2.20	-3.08
	2O/2OH	-1.80	-2.81
	3O/OH	-1.38	-2.28

4.3. Pt(100) model optimisation

4.3.1. Slab thickness, vacuum spacing and relaxed layer optimization

To fully represent a Pt nanoparticle the Pt(100) surface needs to be optimized in the same manner as that used for the Pt(111) surface. In order to achieve an acceptable adsorption energy accuracy with low computational time the slab thickness, vacuum spacing and number of relaxed layers needs to be optimized.

The atomic layers were optimized using a Pt(100) – p(2x2) unit cell with an initial 14 Å vacuum spacing using a cut-off energy of 400 eV. The k-point grid was set to a 10x10x1 grid with a k-point spacing of 0.01778 Å^{-1} with a smearing width of 0.1 eV. The convergence criteria were based on O adsorption energy set to converge to less than 10 meV with the same energy and force convergences as for Pt(111). In order to optimize the number of atomic layers the slab thickness was varied from 2 (8 Pt atoms) to 12 (48 Pt atoms) with the top two layers allowed to relax. A representation of the Pt(100) slab can be seen in Figure 4-9:

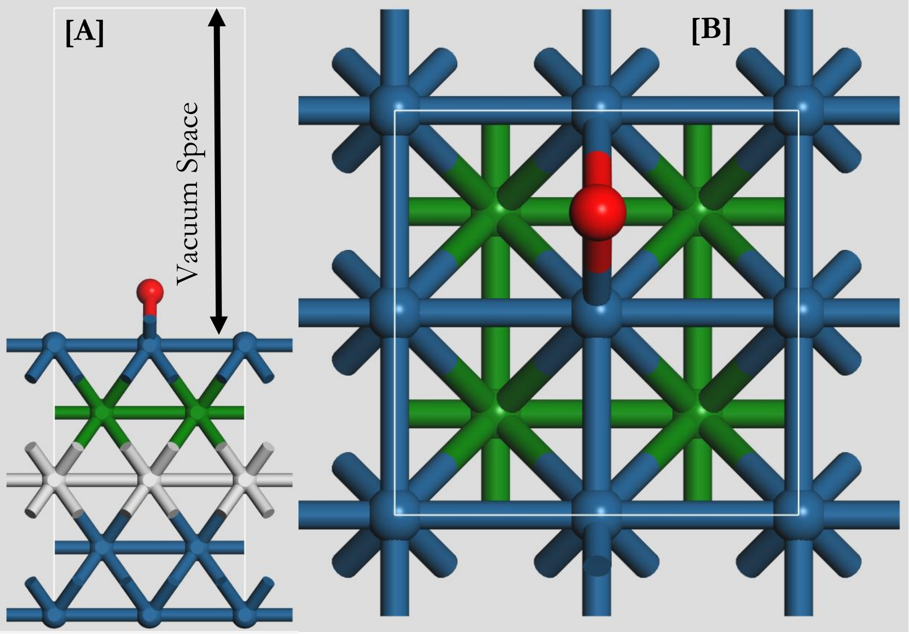

Figure 4-9: Pt(100) 5 layered slab with a 10 Å vacuum using a lattice parameter of 3.976 Å with O adsorbed on the bridge site, second and third layer Pt layer have been coloured green and silver: [A] - Side view, [B] - Top view.

The adsorption energy were calculated using Equation 4-1 and the same reference gas system as for the Pt(111) surface, shown in Table 2-2 and Table 2-3. The adsorption energy were considered converged for a 12 layered slab again, as this is 7 layers larger than similar Pt DFT studies [26], [85]. The results of the adsorption energies can be seen in Figure 4-10 along with the desired convergence criteria. The optimisation resulted in the adsorption energy once again oscillating when the size of the slab increased. To maintain a low computational time while maintaining adsorption energy accuracy a 5 layered Pt(100) slab was selected.

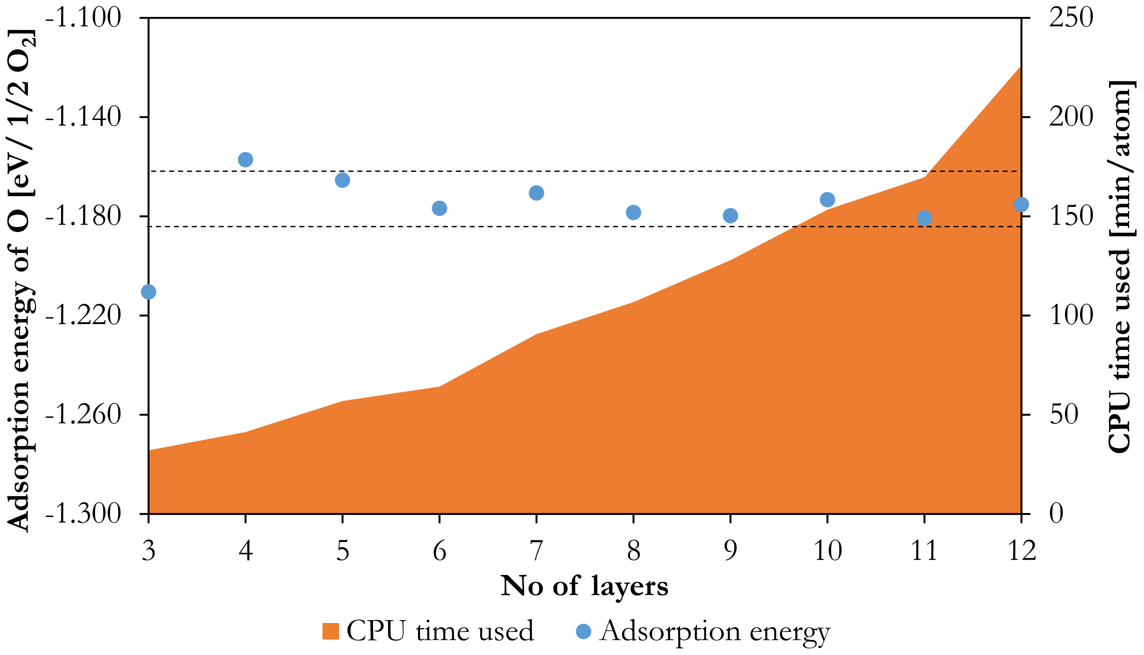

Figure 4-10: Adsorption energy of atomic O as a function of atomic layers on a Pt(100) – p(2x2) slab using 14 Å vacuum space measured between 2 and 12 layers with the top 2 slab layers relaxed. The dotted line is ± 10 meV converged adsorption energy of O referenced to a 12-layered slab.

Following the Pt layers, the vacuum spacing was optimized using a 5 layered Pt(100) – p(2x2) with a 400 eV cut-off energy and a k-point grid of 10x10x1. As before the vacuum spacing was varied between 10 and 14 Å with a 20 Å used to calculate a converged adsorption energy, see Figure 4-11. The energy convergence for Pt(100) followed a similar trend to that of Pt(111), in that there is no significant change in adsorption energy when comparing a 10 Å to a 20 Å vacuum. As a result, utilizing a 10 Å vacuum space was found to be sufficient for the adsorption energy calculations.

The next optimization considered was that of the number of relaxed layers. The optimization of the relaxed slabs was done using the optimal slab layers and vacuum spacing resulting in a 5 layered Pt(100) – p(2x2) surface with a 10 Å vacuum with an fcc adsorbed O species using a 10x10x1 k-point grid and 400 eV cut-off energy. The number of layers relaxed was varied between 2 relaxed layers up to 4 relaxed layers, see Table 4-7.

The number of relaxed layers tends to have no significant effect on the adsorption energy, similar to that observed for the Pt(111) surface. This implied that once again selecting 2 relaxed layers would provide sufficiently converged energies while minimizing the total computational time needed. The choice to maintain at least 2 relaxed layers is similar to that for the Pt(111) surface, it allows any significant deformations on the surface to be observed.

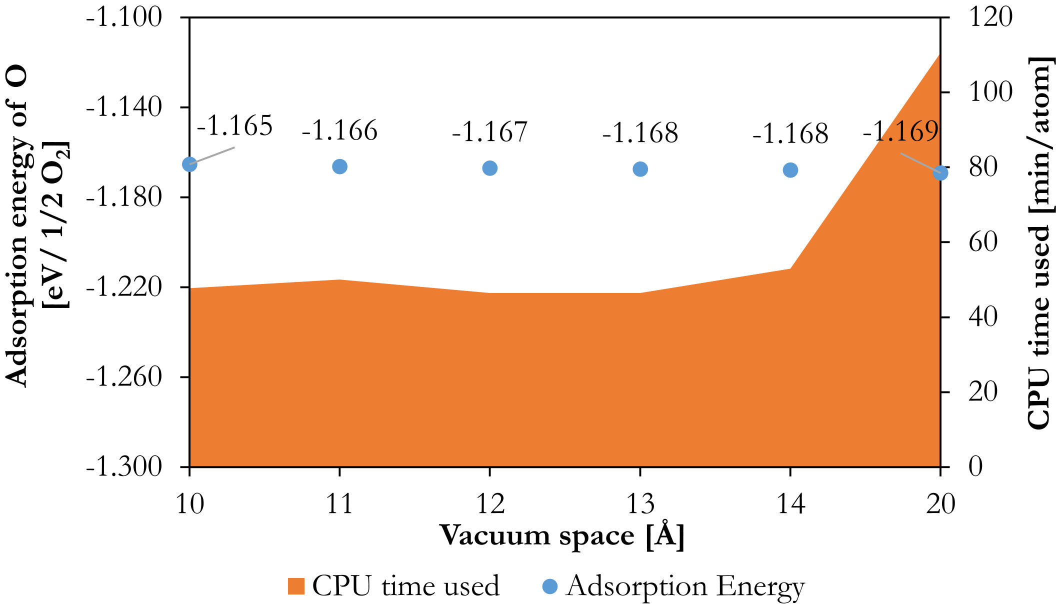

Figure 4-11: Adsorption energy of atomic O as a function of vacuum spacing on a Pt(100) - p(2x2) using a 5 layered slab with the top 2 layers relaxed using 400 eV cut-off energy and a 10x10x1 k-point grid. Converged energy calculated at 20 Å yields $E_{adsorption} = -1.169$ eV.

Table 4-7: Effect on the energy upon adsorption of O on Pt(100) - p(2x2) surface relaxing 2 to 4 layers using 400 eV with a 10x10x1 k-point grid and a 10 Å vacuum.

Number of Relaxed layers (relaxed Pt atoms)	$\Delta E^{*}_{adsorption}$ [eV]	$\Delta E^{**}_{difference}$ [meV]	CPU time used [min/atom]
2 (8)	-1.165	-	53.5
3 (12)	-1.168	-3	56.7
4 (16)	-1.173	-8	58.9

* $E_{adsorbed\ slab} - E_{clean\ slab} - E_{gas\ reference}$

** Taken with reference to 2 relaxed layers

4.3.2. Adsorption site preference for O-containing species

As with the Pt(111) surface the individual preferred adsorption sites for the Pt(100) surface needs to be determined for each adsorbate. For Pt nanoparticles there is more focus given to the dominant (111) surface, as a result there is substantially less research into optimal adsorption sites for the (100) surface for comparisons. In order to ensure that the dominant adsorption site is used each adsorbate was tested in each of the available adsorption sites namely the hollow, bridge and atop sites and allowed to relax to the lowest energy position. The site optimization was done using the optimized 5 layered Pt(100) – p(2x2) slab with the top two layers relaxed using a 400 eV cut-off energy and a k-point grid of 10x10x1 with a 10 Å vacuum. As with the Pt(111) surface each of the starting geometries will be presented here for the Pt(100), see Figure 4-12, with the energies reported in Table 4-8.

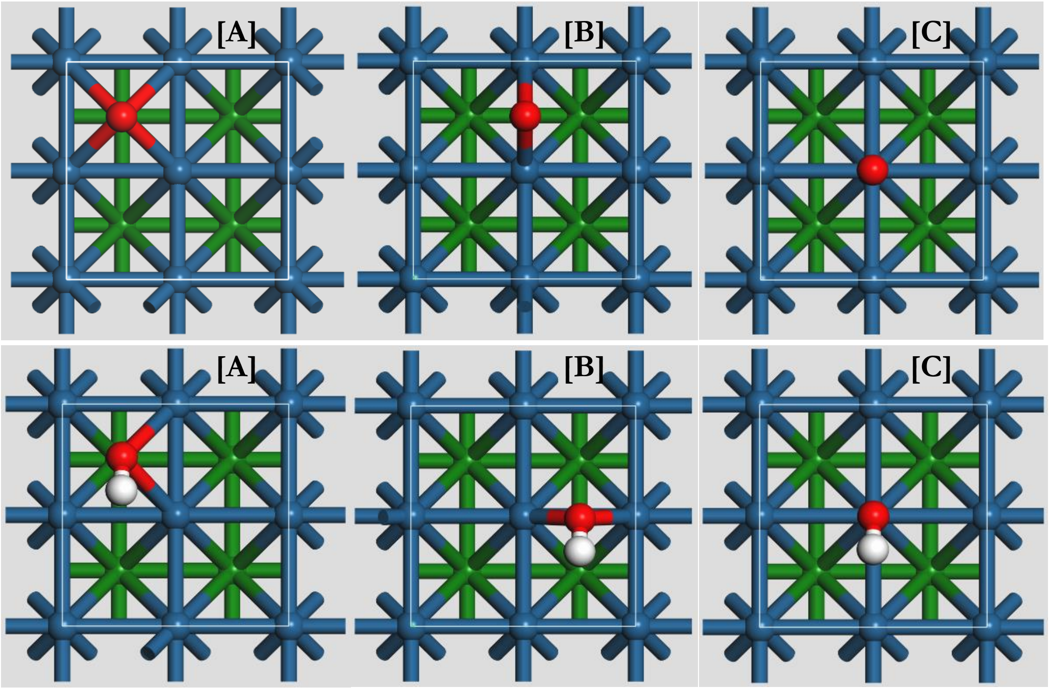

Figure 4-12: Initial adsorption geometry for the preferred adsorption site on the Pt(100) surface testing: [A] - hollow, [B] - bridge and [C] - atop site with Pt – blue/green, O – red and H – white.

Table 4-8: Adsorption energy for optimized geometry for stable O and OH adsorption sites on Pt(100) using PAW-PBE with preferred sites illustrated in bold.

	Adsorption energy [eV]		
Adsorption Site	hcp	bridge	Atop
O	-	**-1.16**	-0.11
OH	-	**-1.15**	-0.68

Table 4-9: Vibrations for Pt(100) O - bridge and OH - bridge adsorption.

Vibration	1	2	3	4	5	6
O [cm^{-1}]	337	216	173	-	-	-
OH [cm^{-1}]	3648	896	533	147	88	39

The geometry of the Pt(100) surface indicate that both O and OH tend to favour the bridge site adsorption with the hollow site not yielding a stable adsorption site. Taking these results into consideration, the initial preferred adsorption sites for O and OH will be bridge site adsorption.

4.3.3. Higher coverage adsorbate configuration

All possible adsorption coverages were tested on the Pt(100) surface using the preferred adsorption sites previously determined. Due to the symmetry in adsorption sites of both O and OH on Pt(100) there are several unique adsorption sites that require testing, although substantially more than that of Pt(111) due to the bridge site adsorption. Taking each coverage of 0.25, 0.50, 0.75 and 1.00 ML with O, OH and O/OH a total of 57 possible unique configurations on the surface are possible. Due to the sheer number of possible geometries possible only the geometries for lowest adsorption energy surfaces for the 14 adsorbate stoichiometries, given in Table 2-2 and Table 2-3, are reported, a full list for every initial geometry tested and electronic energies can be seen in Appendix B. The optimisation for each geometry were performed using the PAW-

PBE/optPBE/optB88 models and it was found that the lowest energy geometry remained the same and that the same bond lengths and angles were determined. This follows the trend seen when investigating the Pt(111) surface. In order to analyse the Pt(100) surface the same approach was used as for the Pt(111). This implies that the following surface dimensions will be reported: the shortest adsorption distance between adsorbate and Pt atom(A), the distance between two surface Pt atoms (S), an interlayer distance (L), distance between adjacent adsorbates (D), hydrogen bond length (B) and the OH bond angle (°). There is some variation for the Pt(100) in that the interlayer distance (L) will report the distance between the centre Pt atom and the third Pt layer, the reason for this is that the distance between the top layer and third layer is comparative to the lattice parameter for Pt. This allows for some indication as to how the surface deformation is affecting the perceived lattice parameter near the adsorbates.

Single species adsorption for O, see Figure 4-13, tends to follow may similar trends to those seen for Pt(111). There are some exceptions, the first is the preference for bridge adsorption, as has been mentioned, which tends to maintain an adsorption length (A) of 1.952 Å at 0.25 ML and remains relatively unchanged at 1.00 ML reaching 1.951 Å. The distance between adjacent adsorbates (D) increases, as with Pt(111), between 0.50 ML and 0.75 ML by 0.010 Å due to repulsion. At 1.00 ML the adsorbates again place themselves equidistance from any adjacent adsorbate at 2.812 Å. This is once again expected due to the repulsive interactions of O adsorbates.

As for the Pt structure, there tends to be minimal deformation between surface Pt atoms at all tested coverages with the largest deviation in surface distance (S) seen when comparing 0.25 ML and 1.00 ML, which remained effectively unchanged due to the small deviation of 0.006 Å. There is however, an effect on the interlayer distance (L) in that the distance increases as coverage increases. This is expected as the negativity of O will draw the Pt atoms closer to the adsorbates. This effect appears to be strongest at 0.75 ML coverage were the interlayer distance increased from 3.871 Å, at 0.25 ML, to 4.051 Å. A reason for the weaker effect at 1.00 ML could be due to the repulsive interactions between the adsorbates weakening the decompression effect.

In contrast OH adsorbates, Figure 4-13, tend to not have a strong decompressing or compressing effect on the interlayer distance (L) as coverage increases. There is also a tendency for less surface distance (S) deformation as the OH switches between atop and bridge site adsorption as coverage increases maintaining a surface distance around 2.811 Å. When OH switches to bridge site adsorption at 0.50 and 0.75 ML we see the largest deviation in the O-H (B) bond. At 0.50 ML the O-H bond increases to 0.990 Å which is further increased to 1.005 Å at 0.75 ML. Once again we can see a tendency for the H atom to tilt towards the next nearest O adsorbate however, on the Pt(100) surface this formation does not seem to reflect the honey-comb structure suspected for Pt(111) but still appears to have some favoured orientation.

In summary for O adsorption there is a repulsive interaction between adsorbates, as seen on Pt(111), with increasing bond lengths or equidistance lengths at full coverage. The Pt(100) surface tends to have less deformation than that of Pt(111), potentially due to the bridge site adsorption of the O adsorbates, although there is a decompressing effect observed between the top 3 layers. In contrast OH adsorbates tend not to have strong compressing or decompressing effects on the top 3 layers nor major surface deformation. There is however an extension of the O-H bond length as coverage increases with the H atom once again tending towards the next nearest O adsorbate as observed by increasing O-H bond lengths (B) and decreasing inter adsorbate distances (D). The same analysis can be done for co-adsorption of O and OH on Pt(100) however, as with Pt(111), due to the increased number of surface interactions first viewing both the single adsorbate and co-adsorbate surfaces will be beneficial prior to discussion, see Figure 4-14.

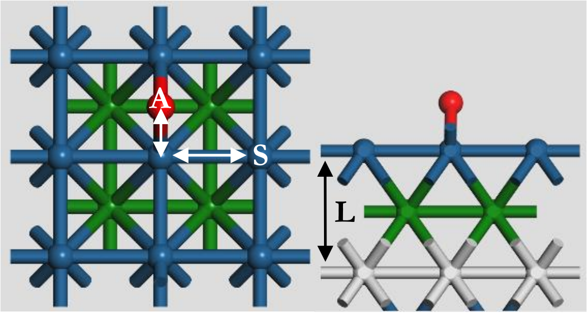

0.25 ML - O

Adsorption length (A)	1.952 Å
Surface distance (S)	2.817 Å
Layer distance (L)	3.871 Å

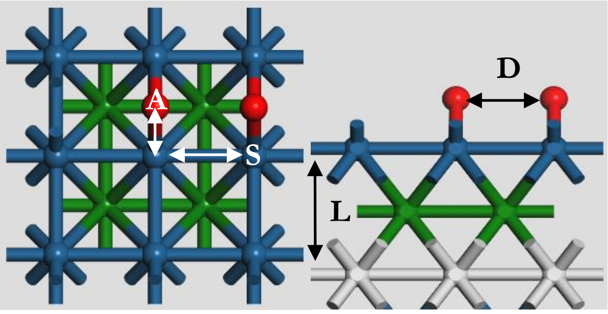

0.50 ML – 2O

Adsorption length (A)	1.947 Å
Surface distance (S)	2.811 Å
Layer distance (L)	4.000 Å
Adsorbate distance (D)	2.812 Å

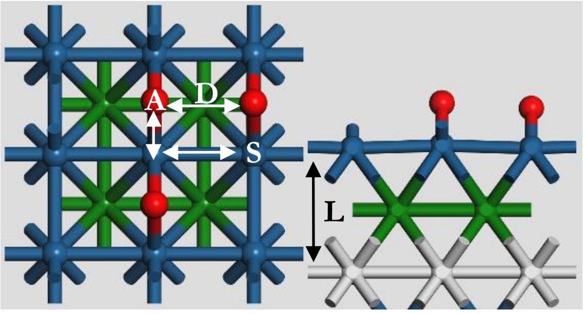

0.75 ML – 3O

Adsorption length (A)	1.950 Å
Surface distance (S)	2.813 Å
Layer distance (L)	4.051 Å
Adsorbate distance (D)	2.826 Å

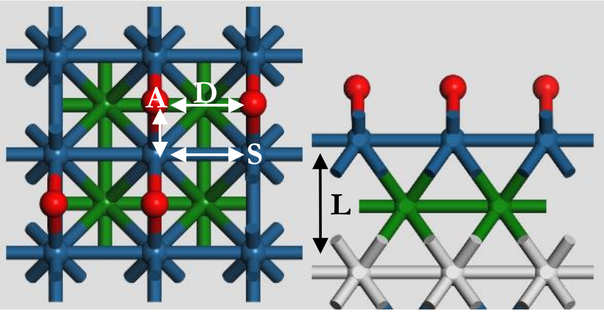

1.00 ML – 4O

Adsorption length (A)	1.951 Å
Surface distance (S)	2.811 Å
Layer distance (L)	4.020 Å
Adsorbate distance (D)	2.812 Å

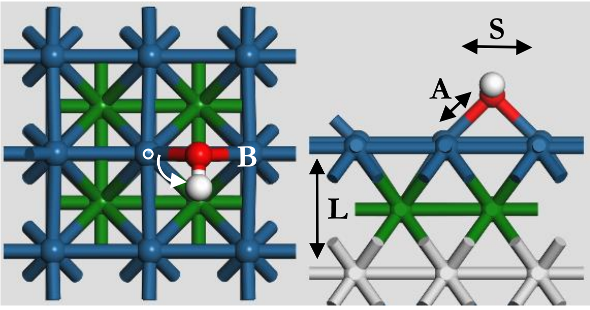

0.25 ML - OH

Adsorption length (A)	2.102 Å
Hydrogen bond (B)	0.984 Å
Surface distance (S)	2.978 Å
Layer distance (L)	4.024 Å
Bond angle (°)	104.6 °

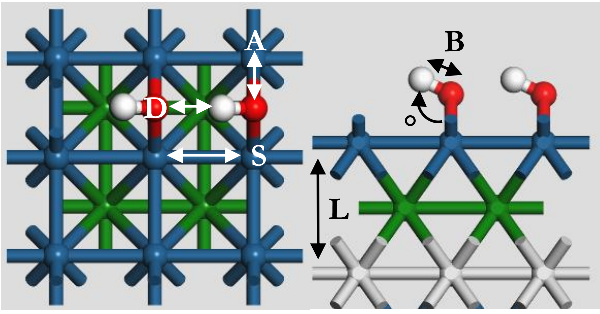

0.50 ML – 2OH

Adsorption length (A)	2.119 Å
Hydrogen bond (B)	0.990 Å
Surface distance (S)	2.812 Å
Layer distance (L)	3.981 Å
Adsorbate distance (D)	1.938 Å
Bond angle (°)	105.8 °

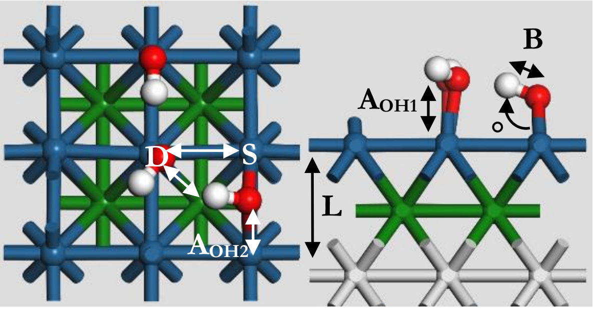

0.75 ML - 3OH

Adsorption length (A_{OH1})	2.023 Å
Adsorption length (A_{OH2})	2.101 Å
Hydrogen bond (B)	1.005 Å
Surface distance (S)	2.811 Å
Layer distance (L)	3.993 Å
Adsorbate distance (D)	1.892 Å
Bond angle (°)	102.7 °

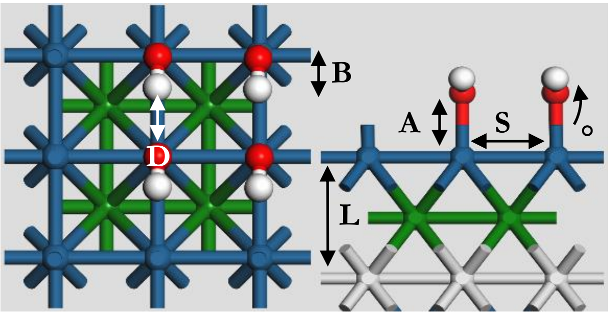

1.00 ML – 4OH

Adsorption length (A)	1.971 Å
Hydrogen bond (B)	0.993 Å
Surface distance (S)	2.811 Å
Layer distance (L)	3.995 Å
Adsorbate distance (D)	1.891 Å
Bond angle (°)	108.0 °

Figure 4-13: Optimized geometries on Pt(100) - p(2x2) for O and OH using a 5 layered slab with 2 relaxed layers using a cut-off energy of 400 eV with a 10 Å vacuum and a 10x10x1 k-point grid with a top view and side view illustrated.

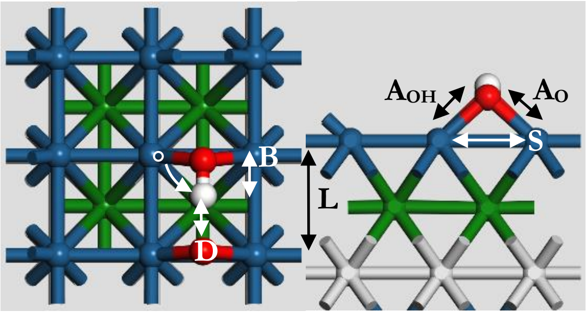

0.50 ML – O/OH

Adsorption length (A_O)	1.983 Å
Adsorption length (A_{OH})	2.071 Å
Hydrogen bond (B)	1.024 Å
Surface distance (S)	2.965 Å
Layer distance (L)	3.989 Å
Adsorbate distance (D)	1.608 Å
Bond angle (°)	102.6 °

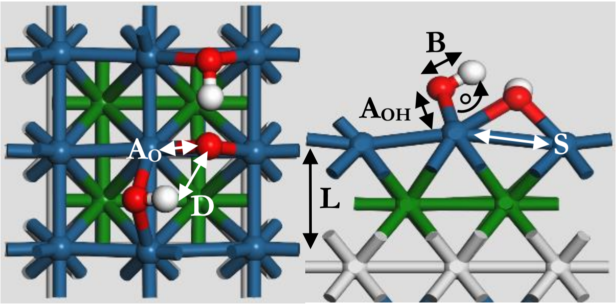

0.75 ML – O/2OH

Adsorption length (A_O)	2.047 Å
Adsorption length (A_{OH})	2.090 Å
Hydrogen bond (B)	0.994 Å
Surface distance (S)	3.033 Å
Layer distance (L)	4.197 Å
Adsorbate distance (D)	2.137 Å
Bond angle (°)	100.0 °

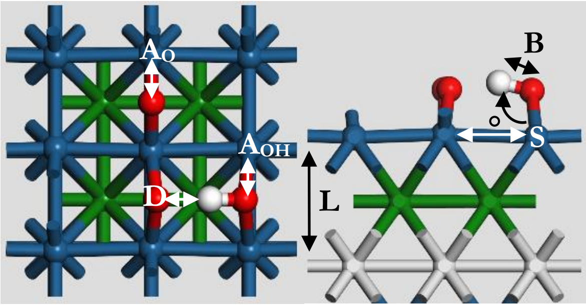

0.75 ML – 2O/OH

Adsorption length (A_O)	1.987 Å
Adsorption length (A_{OH})	2.067 Å
Hydrogen bond (B)	1.039 Å
Surface distance (S)	2.852 Å
Layer distance (L)	4.050 Å
Adsorbate distance (D)	1.549 Å
Bond angle (°)	103.3 °

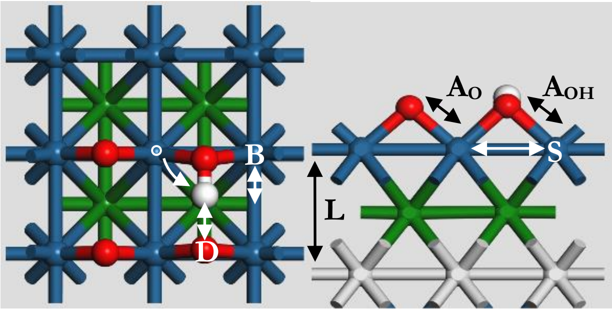

1.00 ML – 3O/OH

Adsorption length (A_O)	1.934 Å
Adsorption length (A_{OH})	2.060 Å
Hydrogen bond (B)	1.038 Å
Surface distance (S)	2.815 Å
Layer distance (L)	4.019 Å
Adsorbate distance (D)	1.561 Å
Bond angle (°)	102.6 °

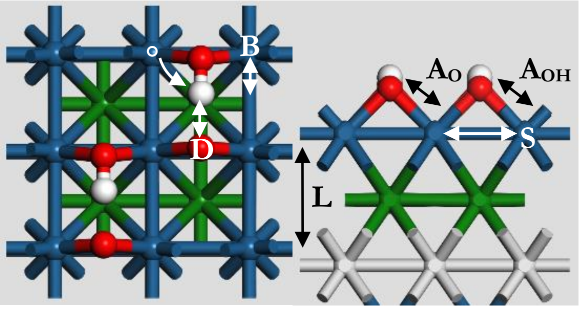

1.00 ML – 2O/2OH

Adsorption length (A_O)	1.970 Å
Adsorption length (A_{OH})	2.064 Å
Hydrogen bond (B)	1.024 Å
Surface distance (S)	2.823 Å
Layer distance (L)	4.010 Å
Adsorbate distance (D)	1.600 Å
Bond angle (°)	102.4 °

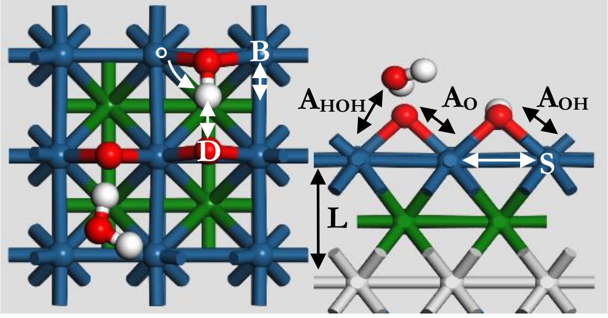

1.00 ML – O/3OH – 2O/OH/H_2O

Adsorption length (A_O)	1.991 Å
Adsorption length (A_{OH})	2.053 Å
Adsorption length (A_{HOH})	2.914 Å
Hydrogen bond (B)	1.040 Å
Surface distance (S)	2.838 Å
Layer distance (L)	4.036 Å
Adsorbate distance (D)	1.535 Å
Bond angle (°)	104.5 °

Figure 4-14: Optimized geometries on Pt(100) - p(2x2) for O/OH co-adsorption using a 5 layered slab with 2 relaxed layers using a cut-off energy of 400 eV with a 10 Å vacuum and a 10x10x1 k-point grid with a top and side view illustrated.

Co-adsorption of O and OH on Pt(100) has one major effect across all coverages that can be seen, that being that the preferred adsorption site for both adsorbates still pertains to bridge site adsorption. At all co-adsorption coverages, the interlayer distance between the top 3 layers increases however, at high coverage (above 0.75 ML) the surface distance between Pt atoms remains relatively unchanged. The largest surface deformation can be seen at 0.50 ML and 0.75 ML – O/2OH coverages with a distance of 2.956 Å and 3.033 Å respectively. As only these two coverages tend towards major deformation it is reasonable to claim that, in comparison to Pt(111), the Pt(100) surface has less deformation in general. As with the Pt(111) surface the adsorbates on Pt(100) tend to form additional species at 1.00 ML with dominant OH coverage in the presence of O tending to form H_2O, leaving a 0.75 ML coverage and a water species 2.914 Å above the surface but with no OOH formation. Additionally at all co-adsorbed coverages the H atom still tends towards the next nearest O adsorbate however, as with single species adsorption, there does not appear to be a honeycomb structure potential on Pt(100). The bond distance for O-H on Pt(100) tends to be much larger than on Pt(111), Figure 4-8. A potential reason for this could be from O and OH bridge site adsorption allowing the hydrogen to rest directly over a hollow site or it could be due to increased adsorbate interaction potential on Pt(100) for hydrogen bonding. In summary it can be noted that the deformation seen on the Pt(100) is not as severe as that of the Pt(111) surface. The reason for this may be due to the preference for both species to have bridge site adsorption. As the species are further apart from each other there may be less of a repulsive interaction that can cause surface deformation. Although the Pt(100) and Pt(111) surface differ in deformation there is a similarity at full co-adsorption coverage with O/3OH in that there is a preference for H_2O formation resulting in a 0.75 ML coverage.

As with the Pt(111) surface these 14 optimised geometries for the Pt(100) surface will form the lowest energy structures for adsorption configuration at various pressures and temperatures. Combining this with the geometries for the Pt(111) surface a full Pt nanoparticle phase diagram can be generated for both Pt(100) and Pt(111) using each of these lowest energy geometries. The electronic energies and vibrations for each of these geometries for both Pt(111) and Pt(100) can be found in Appendix C. However, as with Pt(111) the co-adsorption geometries are based on the lowest energy preferred adsorption sites, namely bridge site adsorption. There may exist lower energy co-adsorption configurations for O and OH having non-bridge site adsorption not tested in this study. As with Pt(111) the adsorption energies for each coverage is given in Table 4-10.

Table 4-10: Adsorption energy, including zero point energy contributions, for the lowest configuration on a Pt(100) surface for PBE/optB88.

Coverage [ML]	Adsorbates	$E_{adsorption}^{elec}$ (PBE) [eV]	$E_{adsorption}^{elec}$ (optB88) [eV]
0.25	O	-1.16	-1.37
	OH	-1.15	-1.35
0.50	2O	-2.41	-2.87
	2OH	-2.60	-2.98
	O/OH	-2.67	-3.07
0.75	3O	-2.61	-3.29
	3OH	-3.08	-3.64
	2O/OH	-2.93	-3.58
	O/2OH	-3.02	-3.65
1.00	4O	-2.84	-3.77
	4OH	-3.22	-4.02
	O/3OH	-3.50	-4.31
	2O/2OH	-3.63	-4.51
	3O/OH	-3.31	-4.22

5. DETERMINING THE EFFECT OF TRANSLATION

5.1. Introduction

Having the optimized model and geometries, we can now use the method and approach for generating the phase diagrams previously outlined but, before we can generate these figures the question of what type of translation barriers are present needs to be answered. As mentioned, there are 3 types of translation barrier that need to be considered; high, moderate and low, each resulting in a different approach required to calculate the thermodynamic contributions. In this section how the contributions were calculated will be outlined along with the results, which will lead to what was chosen for constructing the phase diagrams.

5.2. Translation barrier

The translation barriers were calculated using the optimised slab models and the PAW-PBE model. In order to determine the translations contributions, W_x needs to be found in order to be able to use Equations 2-23 and 2-24 to solve for the translational vibrations. To determine W_x the initial and final geometry for the proposed translation were obtained. Following this a 10 image Nudged Elastic Band calculation was performed in VASP to find the transition state for the translation. The transition state geometry was then optimised, using the energy and force convergence of 10^{-5} eV and 0.01 eV.Å^{-1} as before, and confirmed as a transition state via vibrational analysis, resulting in an imaginary frequency in the direction of the diffusion coordinate. The difference in energy between this transition state and initial state was then taken as the translation barrier.

As an initial investigation the translation barriers for single adsorbate species (O and OH) were considered at 0.25 ML and 0.50 ML on both Pt(111) and Pt(100). The movement on the Pt(111) surface was considered from one stable adsorption site to the next nearest stable adsorption site, which corresponds to an fcc → hcp move for O and atop → bridge for OH, while on Pt(100) this followed bridge → bridge site translation. At coverages of 0.50 ML an additional consideration needs to be given if the adsorbate translates towards a nearby adsorbate or away from a nearby adsorbate. As an illustration if we consider OH on Pt(100), the nearest bridge site can be located adjacent to another adsorbate (A → C) or across the atop site (A → B), see Figure 5-1.

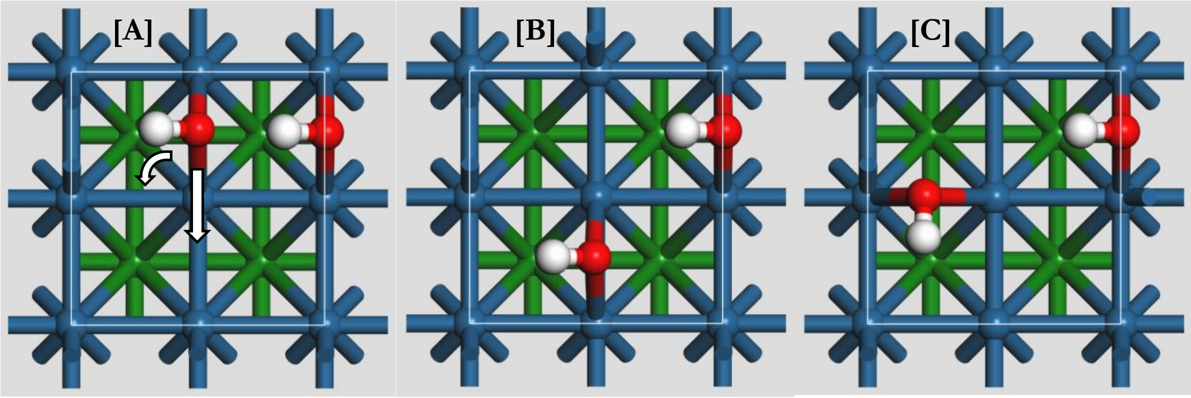

Figure 5-1: Translation locations for OH on Pt(100) at 0.50 ML coverage. [A] – Optimized initial geometry, [B] - atop translation (W_B = 3.49 eV), [C] - adjacent bridge translation (W_C = 1.41 eV).

Although it is possible for both forms of translation to occur, our focus at present is to determine if translation contributions are significant. To determine the significance of translation it is useful to consider the lowest energy pathway, resulting in the minimum barrier that needs to be overcome, which in the case of OH on Pt(100) at 0.50 ML is that of adjacent bridge translation (A → C). As a result, each translation barrier reported is the lowest energy translation barrier found. These minimum translation barriers for O and OH are reported for Pt(111) and Pt(100), see Figure 5-2. However, the translation barrier is only useful when considering the temperature range within which we operate, as translation becomes free when $k_B T \gg W_x$. To appreciate the effect of temperature within the system Figure 5-2 also contains the temperature range at which the energy available to the adsorbate ($k_B T$) approaches that of W_x.

Considering the results displayed in Figure 5-2, the translation barrier increases as the coverage on the surface increases. The increase in translation barrier is expected to become more severe for 0.75 ML and higher, due to repulsive interactions. As the barrier increases the adsorbates are better represented by a 2D lattice gas, i.e. pure vibrational contributions. For these reasons determining the translation barriers at higher coverages (> 0.50 ML) will not justify the computational time, as the thermodynamic contributions will be best described as a 2D lattice gas. At the lowest tested coverage (0.25 ML) a temperature over 1000 °C would be required for the adsorbate thermal energy to reach that of W_x. This implies that the adsorbates, at temperatures below 1000 °C, will typically be well described as a 2D lattice gas. However, a hindered translator model could still describe the energies of the adsorbates, at 0.25 ML, as only around 1000 °C do the models deviate.

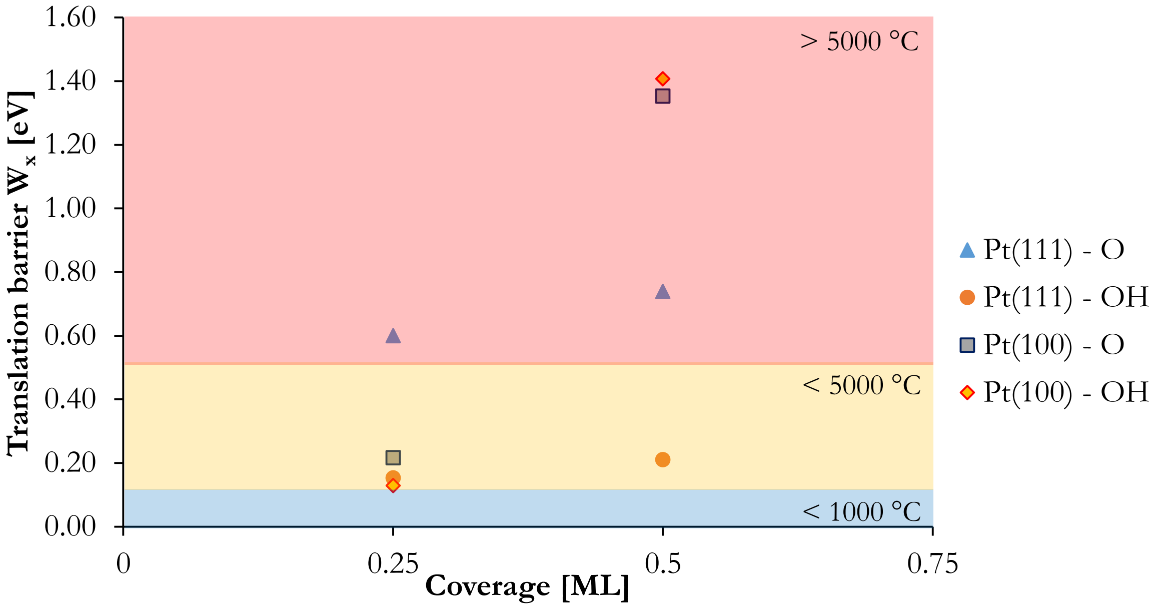

Figure 5-2: Translation barriers for single adsorbate translation in 0.25 ML and 0.50 ML O and OH on Pt(111)/Pt(100). A colour palette has been applied to show the temperature range required for $k_B T \sim W_x$.

The next step in translation determination is therefore to see what the impact a hindered translation model will have on the calculated adsorption energies. As previously mentioned a hindered translator model should describe higher coverage adsorptions as W_x increases. To determine the relative adsorption energies and hindered translator model energies, each adsorption energy was calculated using the reference adsorption, Equation 4-1, with the relative energies for the PAW-PBE reference gas system (Table 2-2) taken from Table 3-1 and Table 3-5. The finite temperature corrections to the adsorption energies were then calculated to obtain the Gibbs free energy upon adsorption, following from Equation 2-12, for both a 2D lattice gas model and a hindered translator model. The relative adsorption Gibbs free energy was calculated at a typical fuel cell temperatures of 80 °C and at elevated temperatures of 200 and 400 °C. The results for 0.25 ML for Pt(111) can be seen in Figure 5-3 for a 2D lattice gas and a hinder translator.

The translation contributions to the free energy for a hindered translator model increases the stability of adsorption by reducing the Gibbs free energy, as seen in Figure 5-3,. However, the difference between considering the adsorbate as a hindered translator, compared to considering the adsorbate as a 2D lattice gas, is minimal for O and OH on Pt(111) at 0.25 ML. It can therefore be said that for O and OH, approximating the adsorption by considering the adsorbates as a 2D lattice gas will be sufficient when constructing the phase diagrams on the Pt(111) surface as W_x is sufficiently larger than the energy available to each adsorbate. It can be noted though that for OH on Pt(111) around 400 °C the energies between a 2D lattice gas and hindered translator start to deviate, which is expected as from Figure 5-2, as OH tends to have a lower translation barrier than O. When considering temperatures above 400 °C it may be preferable to consider OH adsorbates at low coverages (< 0.25 ML) as hindered translators, at higher coverages the increasing translation barrier will tend more towards a 2D lattice gas model.

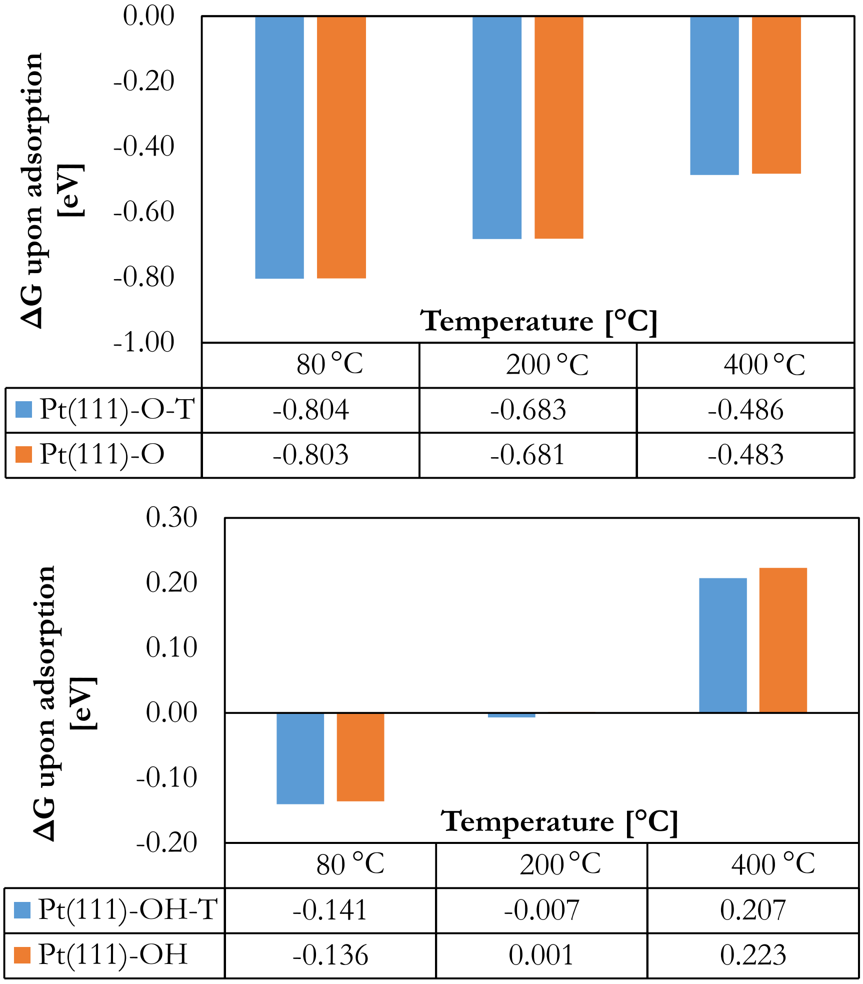

	80 °C	200 °C	400 °C
🟦 Pt(111)-O-T	-0.804	-0.683	-0.486
🟧 Pt(111)-O	-0.803	-0.681	-0.483

	80 °C	200 °C	400 °C
🟦 Pt(111)-OH-T	-0.141	-0.007	0.207
🟧 Pt(111)-OH	-0.136	0.001	0.223

Figure 5-3: Adsorption free energy for O (top) and OH (bottom) on Pt(111) calculated as a hindered translator (T) and as a 2D lattice gas at 80, 200 and 400 °C at 0.25 ML.

The same calculations were performed for the Pt(100) surface which tended to show the same results for O and OH, see Figure 5-4. Once again considering the adsorbates as a hindered translators does not change the adsorption results for O or OH on Pt(100) substantially.

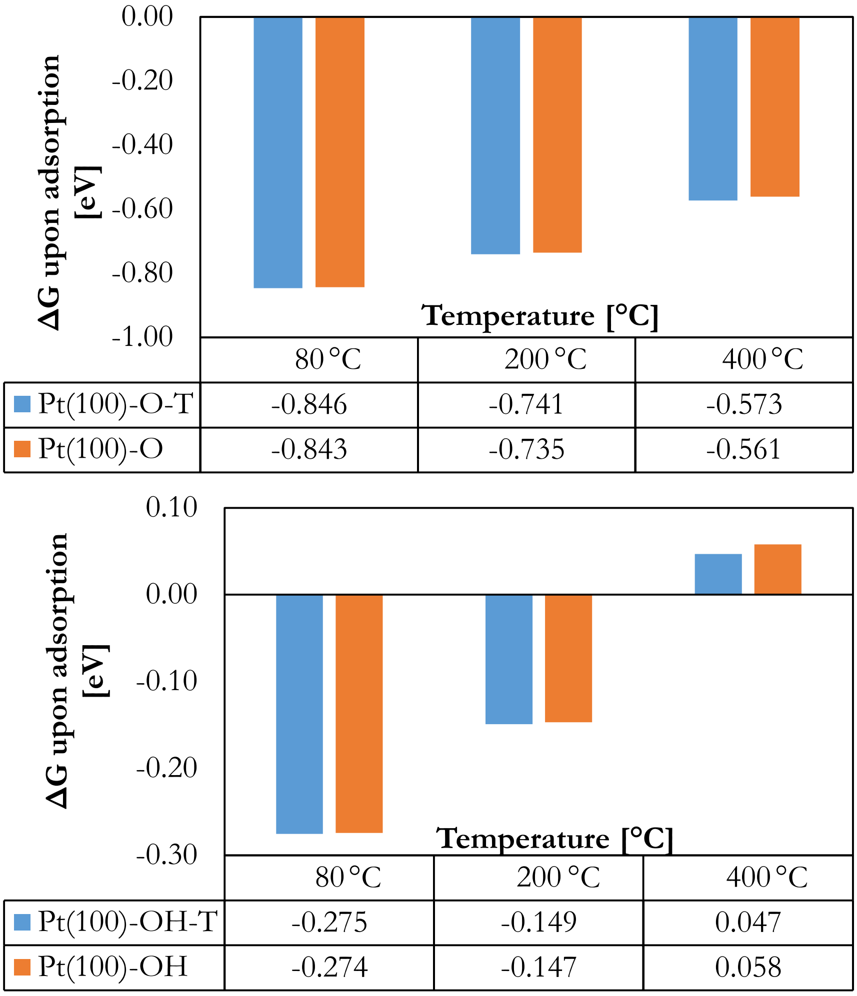

	80 °C	200 °C	400 °C
■ Pt(100)-O-T	-0.846	-0.741	-0.573
■ Pt(100)-O	-0.843	-0.735	-0.561

	80 °C	200 °C	400 °C
■ Pt(100)-OH-T	-0.275	-0.149	0.047
■ Pt(100)-OH	-0.274	-0.147	0.058

Figure 5-4: Adsorption energy for O (top) and OH (bottom) on Pt(100) calculated as a hindered translator (T) and as a 2D lattice gas at 80, 200 and 400 °C at 0.25 ML.

It can be noted however, that the OH trend seen on Pt(111) at 400 °C also appears on the Pt(100) surface as the Gibbs free energy for the two models is not the same, but is not substantially different. The same conclusion can be drawn here i.e. for low coverage OH (< 0.25 ML) the adsorbates are better represented as a hindered translator only when the temperature begins to exceed 400 °C.

The overall difference in the results obtained, when explicitly considering contributions from translation using the hinder translator model, appear not to be significant in the context of this research. As our focus is to determine coverages at temperatures ranges operable for low temperature direct methane to methanol formation all adsorbates on the surface will be analysed at temperatures lower than 400 °C. To save on computational time adsorbate will be treated as 2D lattice gases on the surface, as higher coverages lead to an increase in the translation barrier and the energies of the system are similar for both a hindered translator model and 2D lattice gas for the adsorbates of interest.

6. PHASE DIAGRAMS FOR PT NANOPARTICLE

6.1. Introduction

The optimised model and lowest energy geometries make it now possible to generate the desired phase diagrams to investigate the effect temperature and pressure have on the coverage on Pt(111) and Pt(100), with the adsorbates treated as a 2D lattice gas. In this section the approach used to generate the diagrams will be briefly explained and the results discussed for both the Pt(111) and Pt(100) surface for O/OH adsorbates. In addition to the phase diagram for the PAW-PBE model the PAW-optB88 dispersion model will also be used to generate a phase diagram, which was selected over the PAW-optPBE.

6.2. PAW-PBE model

6.2.1. Pt(111) phase diagram

To determine the adsorption phase diagrams, the energy at zero Kelvin for each of the optimized geometries was calculated using the VASP software and the PAW-PBE model, as outlined in the previous sections. These energies were correct to elevated temperatures and pressures using the thermodynamic contributions to enthalpy and entropy given in Equations 2-12 to 2-22, considering the adsorbates as a 2D lattice gas. This implies that for the enthalpy contributions all degrees of freedom of the adsorbed state are treated as vibrational modes. The same considerations are given to entropy contribution. In addition each adsorption site is considered unique and due to the nature of surface adsorbate systems the degeneracy number, g, was considered to be 1.

For each of the possible adsorbate stoichiometries on the surface, see Table 2-2 and Table 2-3, the change in Gibbs free energy upon adsorption was calculated for each of the optimized geometries, see Figure 4-6, which were referenced to the chemical potential of the gas phase references.

$$E_{adsorption}(T,P) = G_{adsorbate}(T) - n_{H_2O}\mu_{H_2O} - n_{O_2}\mu_{O_2} \qquad 6\text{-}1$$

The adsorption energy for each adsorption possible was then plotted against the chemical potentials. This multi-adsorption energy plot gives an indication of all potential adsorptions but, the only adsorption configurations of interest are those that correspond to the most stable configurations present at each chemical potential, which would result in the lowest possible adsorption energy. Viewing the adsorption plot then from below would thus generate the desired phase diagram, Figure 6-1.

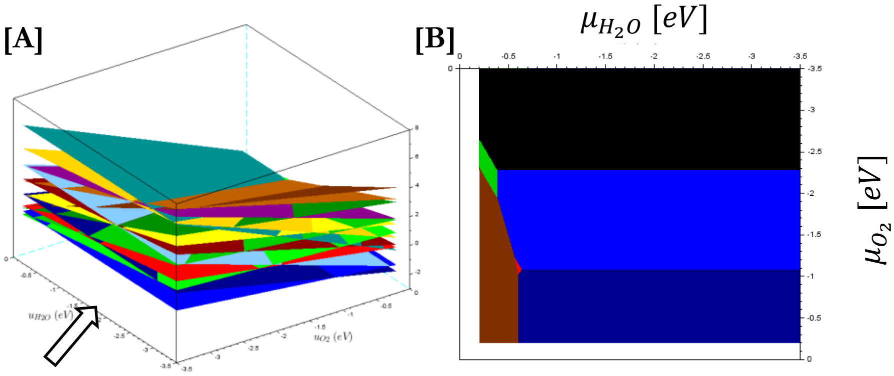

Figure 6-1: Phase diagram generation for Pt(111). [A] - All possible adsorbate configuration adsorption energies, [B] - Viewing A from arrow indication.

The phase diagram can now be populated to indicate what adsorbates are present and the relative chemical potentials can be related to specific temperatures and corresponding partial pressures, see Figure 6-2.

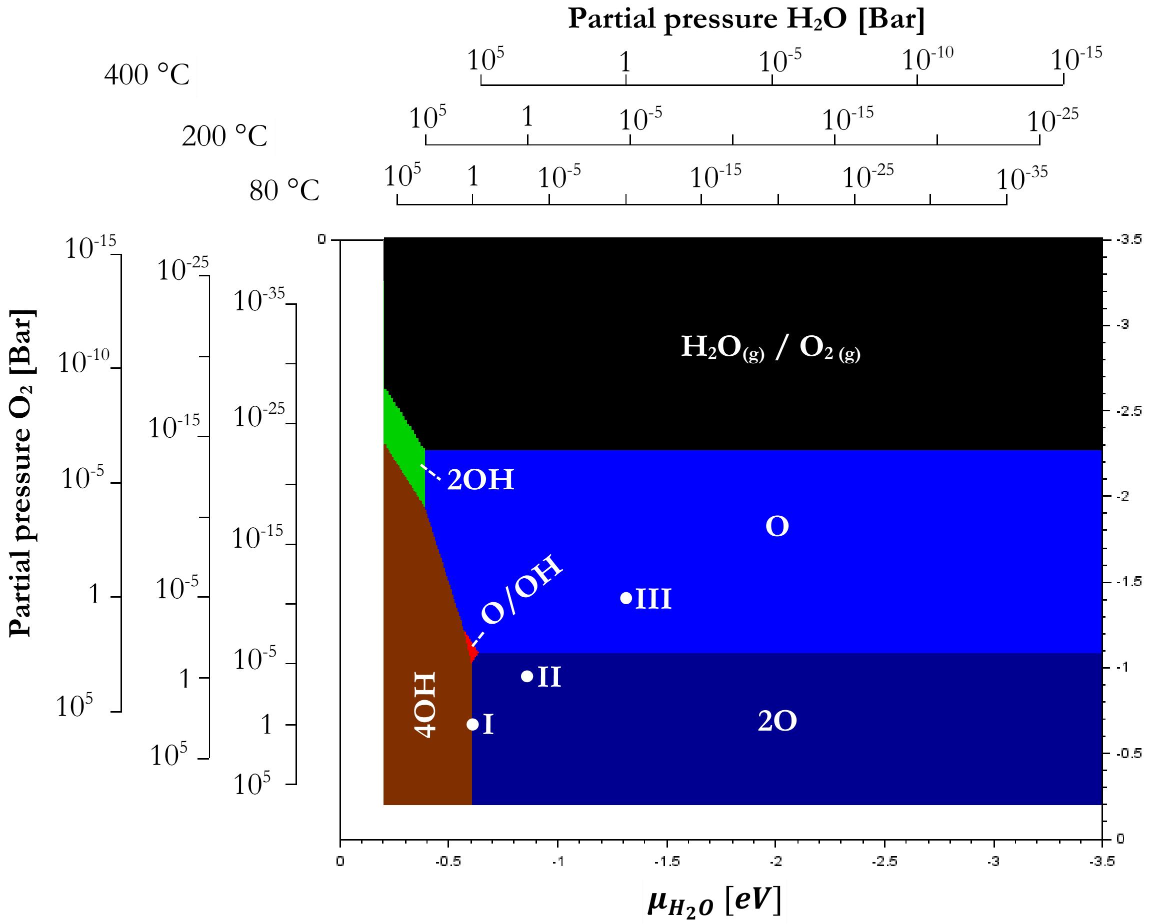

Figure 6-2: Phase diagram for O and OH adsorption on Pt(111)-p(2x2), PAW-PBE, with relevant partial pressures of O_2 and H_2O at various temperatures. Adsorbates present on surface are shown in the coloured areas. As a guide for $P_{H_2O} = P_{O_2} = 1$ bar, I – 80 °C, II – 200 °C and III – 400 °C

There is a lot of information presented in Figure 6-2. As a guide a sample reading will be taken by considering equal partial pressures of O_2 and H_2O, taken at 1 bar. Initially at 80 °C, I in Figure 6-2, the lowest energy adsorbate configuration on the Pt(111) surface corresponds to a coverage of 0.50 ML with 2O present per (2x2) surface unit cell on the surface, see Figure 4-6 for the geometry. As the temperature is increased to 200 °C, II, keeping both partial pressures at 1 bar the same surface adsorbate configuration is still dominant with 0.50 ML coverage with 2O adsorbates. At 400 °C, III, the coverage drops to 0.25 ML with only a single O present when considering a p(2x2) cell. These correspond to the experimentally observed saturation coverages on Pt mentioned in previous studies [26], [27].

An observation from the Pt(111) phase diagram is that there is not a strong tendency for co-adsorption on the surface with mostly single adsorbate species present for the thermodynamically most favourable configurations. There is a single co-adsorbed, 0.50 ML coverage of O/OH obtainable, but across a very limited range of chemical potentials. When considering single species, O only has obtainable coverages of 0.25 ML and 0.50 ML, which agrees with known saturation coverages. In contrast OH can obtain coverages of 0.25 ML, 0.50 ML and fully saturated 1.00 ML.

As seen in Figure 6-2, a variety of temperatures can be used to obtain full coverage with OH, provided that the partial pressures chosen generate the chemical potential required, as a chemical potential at a fixed temperature requires a specific partial pressure. The effect that temperature has on the required partial pressure can be seen in the phase diagram. If we consider full coverage with OH, then increasing the temperatures has the effect of requiring higher pressures of H_2O and O_2 in order to remain at the same phase and vice versa. Taking this understanding forward, the required partial pressure for a fully saturated surface phase can be determined for any temperature provided the required chemical potential is known.

Our focus on full coverage is linked back to the direct methane to methanol route, higher coverage increases the selectivity of methanol but, as seen on the Pt(111) surface, full coverage is only obtainable with OH. This leaves no adsorbed O for reacting. If we shift our temperatures and pressures to have adsorbed O species present, then the coverage shifts to at most 0.50 ML which would then able undesired side reactions to take place. As a result, if we only consider the Pt(111) surface then direct methane to methanol conversion is not feasible here. However, as a Pt nanoparticle exposes two dominant surface facets before making any conclusions considerations need to be given to Pt(100).

6.2.2. Pt(100) phase diagram

Applying the same approach as for the Pt(111) surface the phase diagram for Pt(100)-p(2x2) was generated using the PAW-PBE model, see Figure 6-3 at end of this section. The Pt(100) surface, compared to Pt(111), has a fair amount more co-adsorbate geometries possible, see Figure 4-13 and Figure 4-14 for the optimized geometries. This could be due to the increased area per adsorbate on Pt(100), as the surface is less densely packed than Pt(111). These include full coverage with 2O/2OH, 0.75 ML coverage O/2OH or 2O/OH with water formation and 0.50 ML O/OH. The increase in co-adsorption potential on the surface could be due to O and OH bridge site adsorption which tends to form less surface deformation than the bridge/fcc adsorption seen on Pt(111), see Figure 4-13 and Figure 4-14. This bridge site adsorption also allows for full coverage with O. However, the relative partial pressures required to create a fully saturated surface with O tend to be on the more severe side, requiring pressures around 10^5 bar at 80 °C. It may be tempting to force the conditions that create a fully saturated surface with just O species on Pt(100) although, if we consider both Figure 6-2 and Figure 6-3 we can see that at the conditions that fully cover Pt(100) will only result in 0.50 ML O coverage on Pt(111).

If we consider the same conditions as for Pt(111) of 80 °C, 200 °C and 400 °C keeping the partial pressures at 1 bar, the Pt(100) surface tends to move from fully saturated 2O/2OH to 0.50 ML O/OH followed by 0.50 ML O. In the context of methanol formation this surface has a lot more promise as we can achieve a fully covered surface, increasing selectivity, with adsorbed O present for potential reaction. In addition, at the conditions that could achieve a fully saturated Pt(100) surface with 2O/2OH the Pt(111) surface could be fully saturated with OH. This would result in a Pt nanoparticle that has no free active sites with O present on the Pt(100) surface. There are some observable restrictions present though. The first is that full coverage tends to sit at high chemical potential values for H_2O and O_2. The result is that for full coverage at partial pressures around 1 bar the operating temperature needs to be fairly low (around or less than 80 °C). The second restriction is that the reaction would occur on the Pt(100) surface, which is less dominant than the Pt(111) surface, see Figure 1-6. Despite these restrictions, as it stands, the potential for direct conversion is present for Pt nanoparticles when considering both the Pt(100) and Pt(111) surface.

6.3. Dispersion model

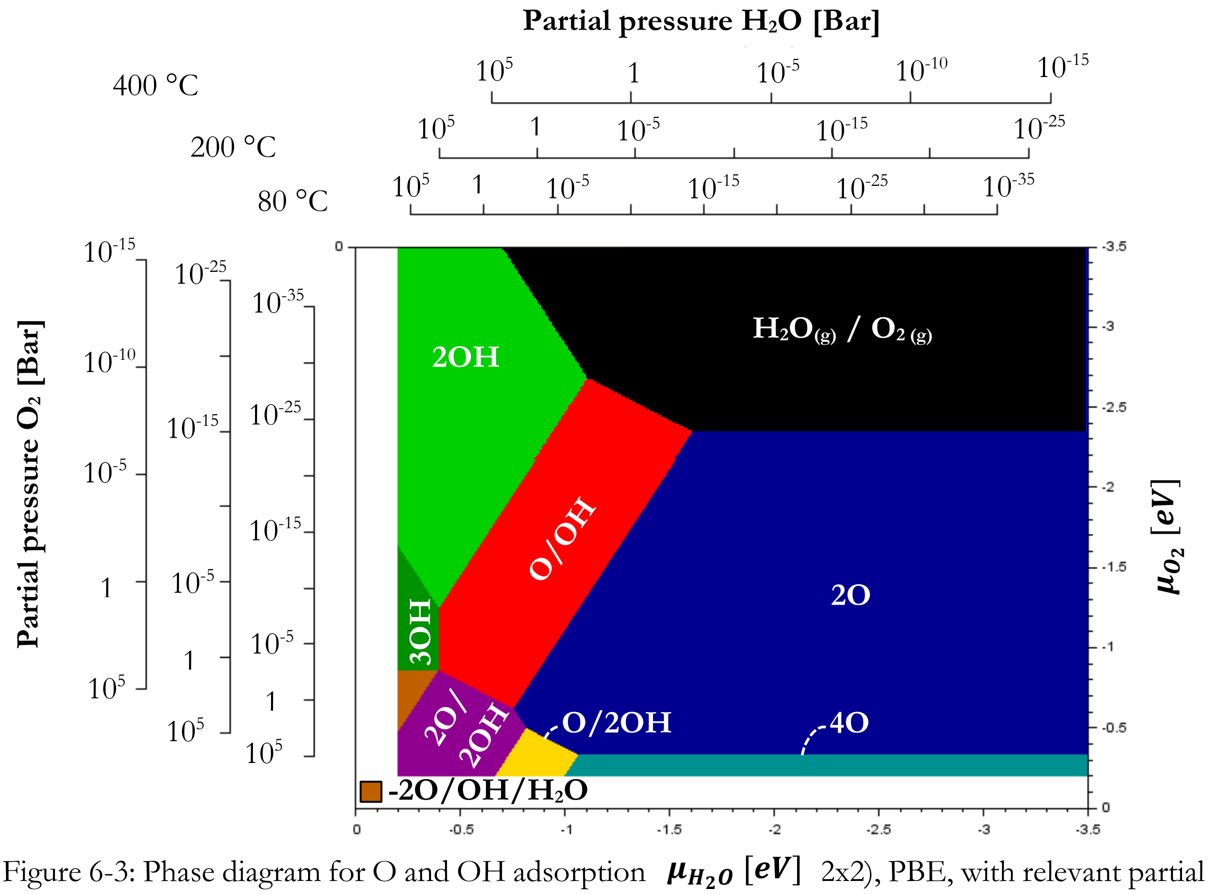

Figure 6-3: Phase diagram for O and OH adsorption 2x2), PBE, with relevant partial pressures of O_2 and H_2O at various temperatures. Adsorbates present on surface are shown in the coloured areas.

6.3.1. Selection of a single dispersion model

The phase diagrams generated up till now utilize the PAW-PBE model which, as mentioned in previous sections, may not account for dispersion forces such as van der Waals. The next step is therefore to regenerate the diagrams using either the optPBE or optB88 model. Due to the computational demands of dispersion models, as reported in Table 4-5, only a single dispersion model can be selected. Until now equal consideration during optimization has been given to both models. As has been shown both the optPBE and optB88 predict the characteristics of the gas molecules with similar accuracy, Table 3-1 and Table 3-5, while also maintaining similar vibrational frequencies within 20 cm^{-1} of each other and during the geometry optimization do not change the lowest energy geometry for each adsorbate combination. As has been reported by Hensley et al. [54], summarised in Figure 2-3, the drawback is that the optPBE model predicts O adsorption in better agreement with experiments, while underestimating OH adsorption. In contrast, optB88 model provides better description of OH adsorption, but overestimates the bonding energy of O.

As both models are able to determine all geometry properties and neither yields a geometry that could eliminate it as a possibility (such as predicting full O coverage at experimentally observed saturation coverages of 0.50 ML), the final factor that will be used to select an appropriate model will be based on the adsorbates present on the phase diagrams generated thus far.

As shown in Figure 6-2 and Figure 6-3 a combination of both OH and O adsorbates is predicted to be thermodynamically favourable on the surfaces. However, at low temperatures and increasing partial pressures above 1 bar OH is dominant on the Pt(111) surface and is repeatedly present on Pt(100) at full coverage co-adsorptions. As this research is interested in finding full coverage, low temperature, operating conditions the model selected will be that of the optB88 to ensure that the adsorption energies of OH are being reasonably approximated, as this adsorbate is present in abundance. The choice of utilizing the optB88 model does imply though that O adsorption is being modelled as stronger than what is experimentally observed which should be kept in mind when the phase diagrams for optB88 are interpreted.

6.3.2. Pt(111) dispersion phase diagram

Taking the same approach as used to generate the Pt(111) phase diagram, Figure 6-2, the phase diagram was recalculated utilizing the PAW-optB88 model for Pt(111)-p(2x2), see Figure 6-4.

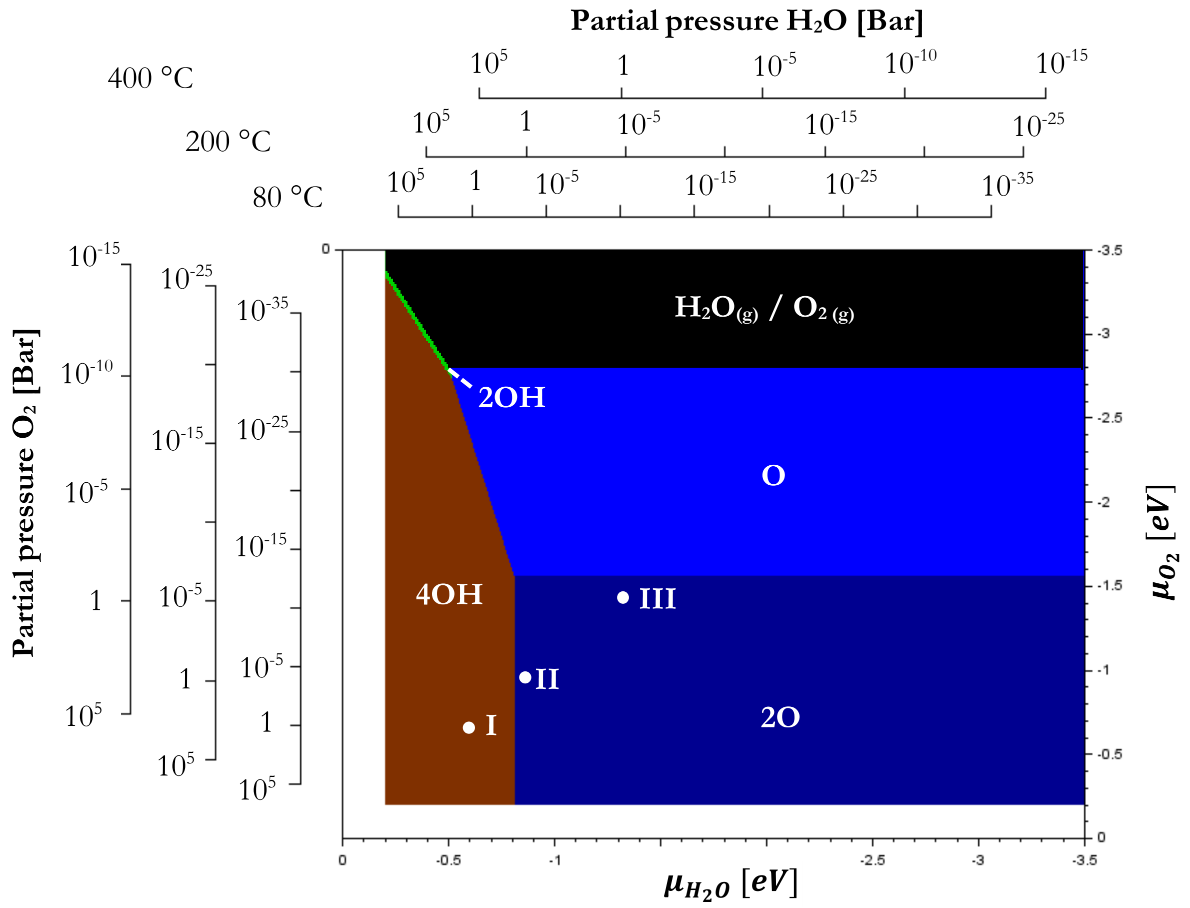

Figure 6-4: Phase diagram for O and OH adsorption on Pt(111)-p(2x2), PAW-optB88, with partial pressures of O_2 and H_2O at various temperatures. Adsorbates present are shown in the coloured areas. As a guide for $P_{H_2O} = P_{O_2}$=1 bar, I – 80 °C, II - 200 °C and III – 300 °C.

There are some notable differences seen when considering the new dispersion phase diagram for Pt(111). The first is that most of the lowest energy configurations found previously are still present, with the exception of O/OH co-adsorption. This is not a largely unexpected result as the operable range to acquire O/OH, as shown in Figure 6-2, was very restricted and introducing an enhancement factor would greatly increase the energies of the nearby 4OH adsorption energies which could remove the O/OH co-adsorption coverage altogether as it becomes less preferable than 4OH. The second observation is that Figure 6-4, when compared to Figure 6-2, appears to have the same general shape, but with all the energies shifted towards lower chemical potentials of both O_2 and H_2O. This results in the same adsorption configurations on the surface being obtainable at higher temperatures and pressures.

If we consider the same conditions as those for Figure 6-2 of 80 °C, 200 °C, and 400 °C with O_2 and H_2O partial pressures of 1 bar, a slightly varied surface is seen. At 80 °C, I, the surface is fully saturated with 4OH which then moves into 0.50 ML with O at II and III. However, this phase diagram has been generated using the optB88 model. This means that I is expected to be a reliable representation of the adsorption energy, as there is only OH present, while at II and III there is only O present on the surface, the stability of which is expected to be overestimated with the optB88 approach. Due to the presence of only single adsorbate species on Pt(111) a reasonably interpretation of the Pt(111) surface can be made by considering both Figure 6-2 and Figure 6-4. The conditions that will result in full coverage on Pt(111) are best approximated by the dispersion phase diagram, as there is only adsorption of OH which is well described by PAW-optB88. In addition the most likely initial coverage at I would more likely tend towards the dispersion phase diagram, 4OH, as OH adsorption is substantially underestimated by the PBE model, more so than O adsorption [54]. However, when we look at O coverage, II and III, then the conditions described by the dispersion model will overestimate the adsorption energy and give misleading chemical potentials. As the PAW-PBE model predicts O adsorption more reliably, the conditions described by the PAW-PBE phase diagram are expected to give a more accurate prediction of the chemical potentials required to obtain a surface with only O.

6.3.3. Pt(100) dispersion phase diagram

To complete the Pt nanoparticle dispersion picture the phase diagram for the Pt(100) surface needs to be generated using the PAW-optB88 model. The same procedure was used in generating this final phase diagram as for the previous diagrams, and can be seen in Figure 6-5.

Similar observations are seen for the dispersion phase diagram of Pt(100) as for Pt(111). The first is once again the tendency for the same lowest energy geometries to be present with the same configurations. In this case no configuration has disappeared, as O/OH had for Pt(111), however it can be seen when comparing Figure 6-3 and Figure 6-5 that any phase close to a phase with more OH present has been "compressed". This can be viewed when comparing the O/OH band which has neighbouring coverages of 2OH, 3OH and 2O/2OH on both the PAW-PBE and PAW-optB88 phase diagrams. In the latter the difference in the maximum and minimum chemical potential range for H_2O which can generate this phase has been reduced. This is due to the enhancement factor for optB88 giving more stability to the OH adsorption. The second observation is again that the general shape of the phase diagram has remained unchanged, with all the configurations shifting to lower chemical potentials, allowing for the same phase to be generated at identical pressures as the PBE phase diagram but at higher temperatures.

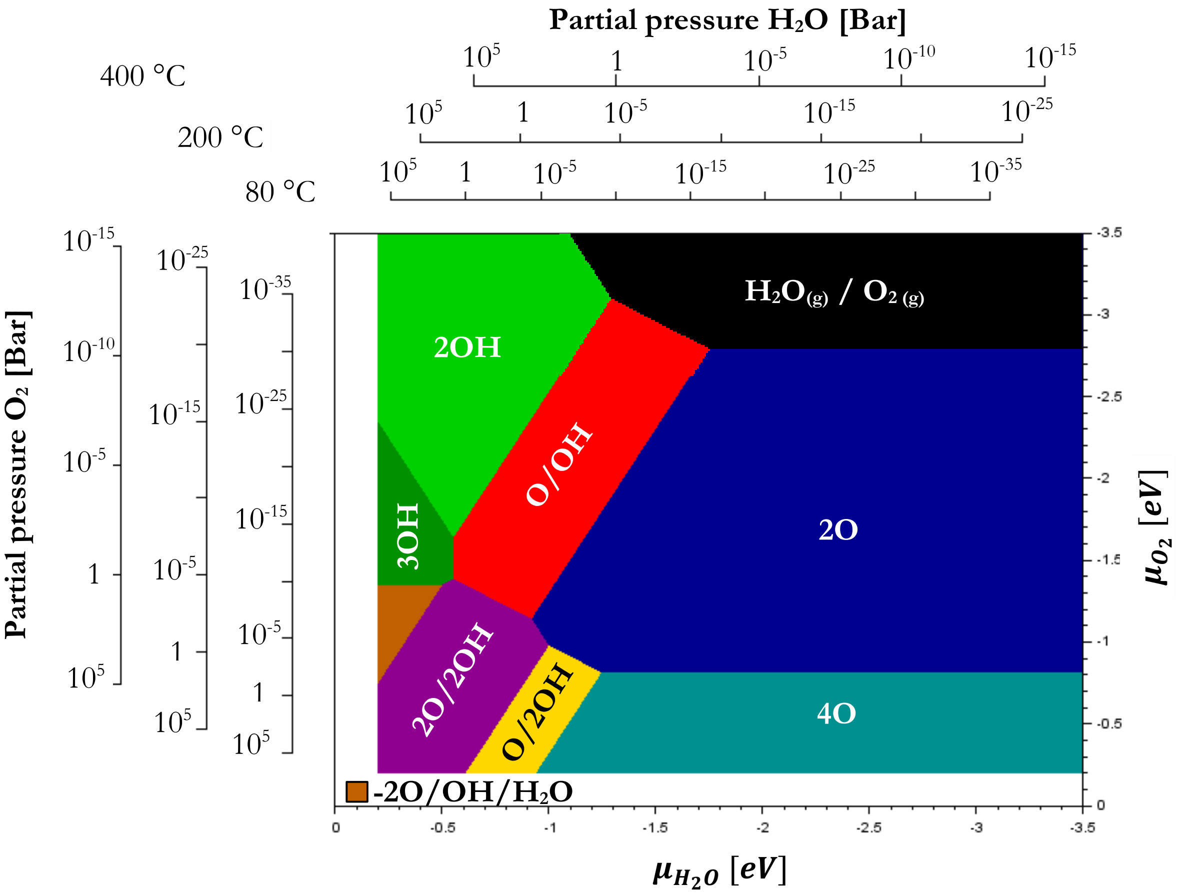

Figure 6-5: Phase diagram for O and OH adsorption on Pt(100)-p(2x2), optB88, with relevant partial pressures of O_2 and H_2O at various temperatures. Adsorbates present on surface are shown in the coloured areas.

The dispersion phase diagram appears to offer more favourable conditions to generate full coverage with O but this is again misleading. As has been previously mentioned, the PAW-optB88 model incorrectly predicts a stronger adsorption for O by a fairly large amount when compared to experiments, as shown in Figure 2-3. It can be claimed again that the conditions that result in only O coverages are better approximated by the PAW-PBE phase diagram, Figure 6-3, than the dispersion phase diagram. As for the dispersion diagram, the conditions that would contribute to coverage with just OH species are better approximated by the PAW-optB88 model. However, the best model for the conditions that result in co-adsorption phases is not as clear cut as it is for single adsorbate species phases. An advantage that can be used is the knowledge that O adsorption is being overestimated in the PAW-optB88 case. This implies that the conditions shown in Figure 6-5 that result in OH coverage will be well approximated and more dominant than adjacent co-adsorption regions which contain an adsorbed O species. It will however be difficult to determine which conditions result in the co-adsorption phases without experimental observations. The most reliable conclusion that can be made is that for any co-adsorption region, the chemical potential required will be within the range between those given for the PAW-PBE and PAW-optB88 phase diagrams, except for any region shown with only single species present.

The inclusion of a dispersion model in the context of direct methane to methanol formation does not change the conclusions drawn from the PBE phase diagram. There still exists a fully covered Pt nanoparticle combination with 4OH on Pt(111) and 2O/2OH on Pt(100), when both surfaces are exposed to the same chemical potential. Should dispersion contributions be significant, then the conditions offered by the optB88 phase diagram are potentially more accurate than that of the PBE model which offer higher temperatures that can be used to achieve the same phase result. This allows for increased reaction rates on the catalyst surface, while still favouring the methanol formation route due to the absence of free active sites for side reactions. However, which model offers the most accurate chemical potential ranges for co-adsorption cannot be selected without experimental observations identifying which phases are present at the relevant chemical potentials on Pt. These phase diagrams do however indicate the possible phases which can be achieved on both surfaces and give an initial operating chemical potential range that could generate these reported phases.

7. CONCLUSIONS

7.1 General conclusions

The focus of this research was to determine the obtainable coverages on the dominant Pt(111) and Pt(100) surfaces with O and OH adsorbates. For each coverage, the adsorption energies were calculated using an optimized Pt slab model generated with an optimized lattice parameter of 3.976 Å representing a (2x2) surface unit cell for each surface which consisted in both cases of a 5 layered slab with the top two layers relaxed, a 10 Å vacuum space using a cut-off energy of 400 eV and a k-point grid of 10x10x1.

The preferred adsorption sites for O and OH were found to be the fcc hollow site and atop site, respectively, on the Pt(111) surface, while on Pt(100) both adsorbates preferred bridge site adsorption. The bridge site adsorption on Pt(100) resulted in less surface deformation than that of the Pt(111) surface, in addition co-adsorption tends to result in more deformation of the surface than single species adsorption.

The adsorbates were found to be best approximated by a 2D lattice gas as the translation barrier for 0.25 ML O and OH were found to be 0.60 and 0.15 eV respectively on Pt(111) with lower barriers on Pt(100) of 0.22 and 0.13 eV. However, at temperatures reaching 400 °C OH adsorbates may need to be represented using a hindered translator model.

When considering the adsorbates as a 2D lattice gas, the PAW-PBE model identified coverages obtainable on Pt(111) pertaining mostly to single adsorbate species. The highest coverage obtainable allowed for full coverage with OH while O remains limited to 0.25 ML and 0.50 ML. In contrast, the Pt(100) surface tends to favour several types of co-adsorption including full coverage with O/OH at equal concentrations and full single species coverage of O. However, the conditions required to fully saturate a surface with O are extreme, requiring pressures in excess of 10^5 bar for O_2 at 80 °C. In addition, any chemical potential combination of O_2 and H_2O which saturates Pt(100) with O leaves Pt(111) only partially covered with 0.50 ML O. However, at chemical potentials between -0.22 and -0.60 eV for O_2 and H_2O it could be possible to fully saturate a Pt nanoparticle, with OH on Pt(111) and O/OH on Pt(100).

When the research was expanded to include dispersion contributions, such as van der Waals, the PAW-optB88 model was chosen, as this model more accurately describes OH adsorption on Pt, which is dominant at higher coverages on both surfaces. The general trend seen when using the dispersion model was a shift in the phases towards lower values of chemical potential for both O_2 and H_2O, while maintaining the same preferred adsorption configurations, sites, bond lengths and vibrations. As the same geometries are achieved, computational time for Pt modelling can be reduced by first optimising structures with the PBE functional and then implementing a dispersion model. With the PAW-optB88 model, the chemical potential range is shifted for full coverage of OH on Pt(111) and O/OH on Pt(100) to -0.22 and -0.80 eV with O_2 and H_2O respectively. However, PAW-optB88 reportedly overestimates the adsorption of O while OH adsorption is more accurately predicted. This implies that the chemical potential range required for full coverage of O on Pt(100) is better approximated by the PAW-PBE phase diagram.

These phase diagrams in the presence and absence of empirically included van der Waals contributions represent the coverages that are obtainable on a Pt nanoparticle. Taking this back to the context of methane to methanol formation operating at a chemical potential of -0.22 and -0.88 eV allows for full coverage on both Pt(111) and Pt(100) with O exposed to react with methane on Pt(100) increasing methanol selectivity. However, to maintain uniform lower partial pressures, around 1 bar, the temperature would need to be around the temperature of Pt fuel cells, 80 °C, with increasing temperature increasing the required partial pressure.

7.2 Recommendations

The potential for full adsorbate coverage on Pt nanoparticles with O exposed for reacting with methane has several promising implications. The next step in the evolution of direct methane to methanol formation would be to test the conditions given in this theoretical research e.g. exposing a Pt catalyst to O_2 and H_2O at chemical potentials of -0.22 and -0.80 eV, with focus given to identifying which adsorbate species are present on the surface. This will not only advance research in methanol formation, but will also serve as an analysis into the accuracy of the dispersion models used to predict co-adsorption, as it has been reported that the PAW-optB88 functional over-predicts O adsorption interactions while PAW-optPBE under-predicts OH adsorption.

In addition, it would be beneficial to expand this research to a larger unit cell such as a (3x3) surface unit cell. This will increase the testable coverages and potentially enable investigation of the honeycomb OH adsorption structure reported by LEED imaging for OH adsorbed on Pt(111).

This research tends to indicate that co-adsorption with O and OH results in the reaction surface being the Pt(100) surface; although this surface is present on a Pt nanoparticle, it exposes less surface area than Pt(111). A final recommendation that can be taken from this research is to investigate possible doping or synthesis techniques that could promote a tendency to form larger Pt(100) surfaces over Pt(111).

REFERENCES

[1] British Petroleum, "BP Statistical Review of World Energy About this review," London, 2016.

[2] You, J., Dou, L., Yoshimura, K., Kato, T., Ohya, K., Moriarty, T., Emery, K., Chen, C., Gao, J., Li, G., and Yang, Y., "A polymer tandem solar cell with 10.6% power conversion efficiency," *Nature Communications*, vol. 4, pp. 1410–1446, 2013.

[3] Liu, H., Song, C., Zhang, L., Zhang, J., Wang, H., and Wilkinson, D. P., "A review of anode catalysis in the direct methanol fuel cell," *Journal of Power Sources*, vol. 155, pp. 95–110, 2006.

[4] Antolini, E., Lopes, T., and Gonzalez, E. R., "An overview of platinum-based catalysts as methanol-resistant oxygen reduction materials for direct methanol fuel cells," *Journal of Alloys and Compounds*, vol. 461, no. 1–2, pp. 253–262, 2008.

[5] Green, D. W. and Perry, R. H., *Perry's Chemical Engineers' Handbook*, 8th ed. University of Kansas: McGraw-Hill, 2008.

[6] Shoji, S., Sadahisa, O., Mitsuo, I., and Asa, H., "Generator control system for a hybrid vehicle driven by an electric motor and an internal combustion engine," 5,786,640, 1998.

[7] Wilson, G. R., Edwards, T., Corporan, E., and Freerks, R. L., "Certification of alternative aviation fuels and blend components," *Energy & Fuels*, no. 27, pp. 962–966, 2013.

[8] British Petroleum, "BP Energy Outlook 2030," *South Africa*, no. March, 2012.

[9] Reed, T. B. and Lerner, R. M., "Methanol: A Versatile Fuel for Immediate Use," *Science*, vol. 182, no. 4119. pp. 1299–1304, 1973.

[10] Foster, N. R., "Direct catalytic oxidation of methane to methanol — a review," *Applied catalysis*, vol. 19, pp. 1–11, 1985.

[11] Hamnett, A., "Mechanism and electrocatalysis in the direct methanol fuel cell," *Catalysis Today*, vol. 38, no. 4, pp. 445–457, 1997.

[12] Antonucci, P. L. and Cretı, P., "Investigation of a direct methanol fuel cell based on a composite Nafion ® -silica electrolyte for high temperature operation," *Solid State Ionics*, vol. 125, pp. 431–437, 1999.

[13] Nørskov, J. K., Ressmeisl, J., Logadottir, A., Lindqvist, L., Kitchin, J. R., Bligaard, T., and Jonsson, H., "Origin of the overpotential for oxygen reduction at a fuel cell cathode," *J. Phys. Chem. B*, vol. 108, pp. 17886–17892, 2004.

[14] Raudaskoski, R., Turpeinen, E., Lenkkeri, R., Pongrácz, E., and Keiski, R. L., "Catalytic activation of carbon dioxide: Use of secondary carbon dioxide for the production of synthesis gas and for methanol synthesis over copper-based zirconia-containing catalysts," *Catalysis Today*, vol. 144, no. 3–4, pp. 318–323, 2009.

[15] Ono, Y., Adachi, H., and Senoda, Y., "Selective conversion of methanol into aromatic hydrocarbons over zinc-exchanged ZSM-5 zeolites," *Journal of the Chemical Society, Faraday Transactions*, vol. 84, no. 4, pp. 1091–1099, 1988.

[16] Mitsubishi Gas Chemical, "MGC Mitsubishi Gas Chemical Methanol," 2017. [Online]. Available: http://www.mgc-a.com/methanol/global/index.html. [Accessed: 01-Aug-2017].

[17] Burch, R., Squire, G. D., and Tsang, S. C., "Direct conversion of methane into methanol," *Journal of the Chemical Society, Faraday Transactions 1: Physical Chemistry in Condensed Phases*, vol. 85, no. 10, p. 3561, 1989.

[18] Fratesi, G., Gava, P., and Gironcoli, S. De, "Direct Methane-to-Methanol Conversion : Insight from First-Principles Calculations," *Journal of Physical Chemistry B*, vol. 111, pp. 17015–17019, 2007.

[19] Gesser, H. D. and Hunter, N. R., "The Direct Conversion of Methane to Methanol by Controlled Oxidation," *Chemical Reviews*, vol. 85, no. 4, pp. 235–244, 1985.

[20] Tomkins, P., Ranocchiari, M., and Bokhoven, J. A. Van, "Direct conversion of methane to methanol under mild conditions over Cu-Zeolites and beyond," *Accounts of Chemical Research*, vol. 50, pp. 418–425, 2017.

[21] Palkovits, R., Antonietti, M., Kuhn, P., Thomas, A., and Schüth, F., "Solid catalysts for the selective low-temperature oxidation of methane to methanol," *Angewandte Chemie - International Edition*, vol. 48, no. 37, pp. 6909–6912, 2009.

[22] Periana, R. A., Taube, D. J., Evitt, E. R., Loffle, D. G., Wentrcek, P. R., Voss, G., and Masuda, T., "A mercury-catalyzed, high-yield system for the oxidation of methane to methanol," *American Association for the Advancement of Science*, vol. 259, no. 5093, pp. 340–343, 1993.

[23] Tang, P., Zhu, Q., Wu, Z., and Ma, D., "Methane activation: the past and future," *Energy Environ. Sci.*, vol. 7, no. 8, pp. 2580–2591, 2014.

[24] Latimer, A. A., Aljama, H., Kakekhani, A., Yoo, J. S., Kulkarni, A., Tsai, C., Garcia-Melchor, M., Abild-Pedersen, F., and Nørskov, J. K., "Mechanistic insights into heterogeneous methane activation," *Phys. Chem. Chem. Phys.*, vol. 19, no. 5, pp. 3575–3581, 2017.

[25] Kondratenko, E. V, Peppel, T., Seeburg, D., Kondratenko, V. A., Kalevaru, N., Martin, A., and Wohlrab, S., "Methane conversion into different hydrocarbons or oxygenates : current status and future perspectives in catalyst development and reactor operation," *Catalysis Science & Technology*, vol. 7, pp. 366–381, 2017.

[26] Tang, H., Van Der Ven, A., and Trout, B. L., "Phase diagram of oxygen adsorbed on platinum (111) by first-principles investigation," *Physical Review B - Condensed Matter and Materials Physics*, vol. 70, no. 4, p. 045420 (1-10), 2004.

[27] Karp, E. M., Campbell, C. T., Studt, F., Abild-Pedersen, F., and Norskov, J. K., "Energetics of oxygen adatoms, hydroxyl species and water dissociation on Pt(111)," *Journal of Physical Chemistry C*, vol. 116, no. 49, pp. 25772–25776, 2012.

[28] Bechstedt, F., *Principles of Surface Physics*. Berlin: Springer-Verlag Berlin Heidelberg, 2003.

[29] Stekolnikov, A. A. and Bechstedt, F., "Shape of free and constrained group-IV crystallites: Influence of surface energies," *Physical Review B - Condensed Matter and Materials Physics*, vol. 72, no. 12, pp. 1–9, 2005.

[30] Song, H., Kim, F., Connor, S., Somorjai, G. A., and Yang, P., "Pt Nanocrystals: Shape Control and Langmuir - Blodgett Monolayer Formation," *The Journal of Physical Chemistry B*, vol. 109, no. 1, pp. 188–193, 2005.

[31] Miracle-Sole, S., "Wulff shape of equilibrium crystals," *Condensed Matter Statistical Mechanics*, no. 1, pp. 1–15, 2013.

[32] Tripković, V., Cerri, I., Bligaard, T., and Rossmeisl, J., "The influence of particle shape and size on the activity of platinum nanoparticles for oxygen reduction reaction: A density functional theory study," *Catalysis Letters*, vol. 144, no. 3, pp. 380–388, 2014.

[33] Van Helden, P., Ciobîcə, I. M., and Coetzer, R. L. J., "The size-dependent site composition of FCC cobalt nanocrystals," *Catalysis Today*, vol. 261, pp. 48–59, 2016.

[34] Arblaster, B. J. W., "Crystallographic Properties of Platinum," *Platinum Metal Rev*, vol. 1, no. iii, pp. 12–21, 1997.

[35] Eichler, A., Mittendorfer, F., and Hafner, J., "Precursor-mediated adsorption of oxygen on the (111) surfaces of platinum-group metals," *Physical Review B*, vol. 62, no. 7, pp. 4744–4755, 2000.

[36] Ford, D. C., Xu, Y., and Mavrikakis, M., "Atomic and molecular adsorption on Pt(111)," *Surface Science*, vol. 587, no. 3, pp. 159–174, 2005.

[37] Han, B. C., Miranda, C. R., and Ceder, G., "Effect of particle size and surface structure on adsorption of O and OH on platinum nanoparticles: A first-principles study," *Physical Review B - Condensed Matter and Materials Physics*, vol. 77, no. 7, pp. 1–9, 2008.

[38] Gland, J. L., Sexton, B. A., and Fisher, G. B., "Oxygen interactions with Pt(111) surfaces," *Surface Science*, vol. 95, no. 2–3, pp. 587–602, 1980.

[39] Steininger, H., Lehwald, S., and Ibach, H., "Adsorption of oxygen on Pt(111)," *Surface Science*, vol. 123, no. 1, pp. 1–17, 1982.

[40] Jacob, T., Merinov, B. V., and Goddard, W. A., "Chemisorption of atomic oxygen on Pt (111) and Pt / Ni (111) surfaces," *Chemical Physics Letters*, vol. 385, pp. 374–377, 2004.

[41] Bedurftig, K., Volkening, S., Wang, Y., Wintterlin, J., Jacobi, K., and Ertl, G., "Vibrational and structural properties of OH adsorbed on Pt(111)," *Journal of Chemical Physics*, vol. 111, no. 24, pp. 11147–11154, 1999.

[42] Michaelides, A. and Hu, P., "A density functional theory study of hydroxyl and the intermediate in the water formation reaction on Pt," *Journal of Chemical Physics*, vol. 114, no. 1, pp. 513–519, 2001.

[43] Seitsonen, A. P., Zhu, Y., Bedu, K., and Over, H., "Bonding mechanism and atomic geometry of an ordered hydroxyl overlayer on Pt (111)," *Journal American Chemical Society*, vol. 123, no. 30, pp. 7347–7351, 2001.

[44] Jones, R. and Gunnarsson, O., "The density functional formalism, its applications and prospects," *Reviews of Modern Physics*, vol. 61, no. 3, pp. 689–740, 1989.

[45] Greeley, J., Nørskov, J. K., and Mavrikakis, M., "Electronic structure and catalysis on metal surfaces," *Reviews of Modern Physics*, vol. 53, pp. 319–348, 2002.

[46] Kohn, W., *Density functional theory*, vol. 337. 1993.

[47] Perdew, J. P., Burke, K., and Ernzerhof, M., "Generalized gradient approximation made simple," *Physical Review Letters*, vol. 77, no. 18, pp. 3865–3868, 1996.

[48] Hammer, B., Hansen, L. B., and Norskov, J. K., "Improved adsorption energetics within density-functional theory using revised Perdew-Burke-Ernzerhof functionals," *Phys.Chem.Chem.Phys.*, vol. 59, no. 11, pp. 7413–7421, 1999.

[49] Perdew, J. P. and Wang, Y., "Accurate and simple analytic representation of the electron-

gas correlation energy," *Physical Review B*, vol. 45, no. 23, pp. 244–249, 1992.

[50] Payne, M. C., Teter, M. P., Allan, D. C., Arias, T. A., and Joannopoulos, J. D., "Iterative minimization techniques for ab initio total-energy molecular dynamics and conjugate gradients calculations :," *Reviews of Modern Physicsv*, vol. 64, no. 4, pp. 1045–1095, 1992.

[51] Orio, M., Dimitrious, A. P., and Neese, F., "Density functional theory," *Photosynth Res*, vol. 102, pp. 443–453, 2009.

[52] Wellendorff, J., Silbaugh, T. L., Nørskov, J. K., Bligaard, T., Studt, F., and Campbell, C. T., "A benchmark database for adsorption bond energies to transition metal surfaces and comparison to selected DFT functionals," *Surface Science*, vol. 640, pp. 36–44, 2015.

[53] Klimes, J., Bowler, D. R., and Michaelides, A., "Chemical accuracy for the van der Waals density functional," *Journal of Physics: Condensed Matter*, vol. 22, pp. 1–4, 2010.

[54] Hensley, A. J. R., Ghale, K., Rieg, C., Dang, T., Anderst, E., Studt, F., Campbell, C. T., Mcewen, J., and Xu, Y., "DFT-based method for more accurate adsorption energies : An adaptive sum of energies from RPBE and vdW density functionals," *Journal of Physical Chemistry C*, vol. 121, pp. 4937–4945, 2017.

[55] Ernzerhof, P. B., "Physical review letters: Perdew, Burke, and Ernzerhof Reply," *Physical Review Letters*, vol. 115, no. 1997, p. 9007, 1998.

[56] Ernzerhof, M. and Scuseria, G. E., "Assessment of the Perdew – Burke – Ernzerhof exchange-correlation functional," *Journal of Chemical Physics*, vol. 110, no. 11, pp. 5029–5035, 1999.

[57] Dion, M., Rydberg, H., Schroder, E., Langreth, D. C., and Lundqvist, B. I., "Van der Waals density functional for general geometries," *Physical Review Letters*, vol. 92, no. 24, pp. 1–4, 2004.

[58] Cooper, V. R., "Van der Waals density functional : An appropriate exchange functional," *Physical Review B*, vol. 81, pp. 1–4, 2010.

[59] Perdew, J. P., Ruzsinszky, A., Csonka, I., Vydrov, O. A., Scuseria, G. E., Constantin, L. A., Zhou, X., and Burke, K., "Restoring the density-gradient expansion for exchange in solids and surfaces," *Physical Review Letters*, vol. 136406, no. April, pp. 1–4, 2008.

[60] Klimeš, J. and Michaelides, A., "Perspective : Advances and challenges in treating van der Waals dispersion forces in density functional theory Perspective : Advances and challenges in treating van der Waals dispersion," *Journal of Chem*, no. 137, pp. 120901-1-10, 2012.

[61] Kresse, G. and Hafner, J., "Ab initio molecular dynamics for liquid metals," *Physical Review B*, vol. 47, no. 1, pp. 558–561, 1993.

[62] Kresse, G. and Hafner, J., "Ab initio molecular dynamics for open-shell transition metals," *Physical Review B*, vol. 48, no. 17, pp. 48–51, 1993.

[63] Kresse, G. and Furthmiiller, J., "Efficiency of ab-initio total energy calculations for metals and semiconductors using a plane-wave basis set," *Computational Materials Science*, vol. 6, pp. 15–50, 1996.

[64] Blochl, P. E., "Projector augmented-wave method," *Physical Review B*, vol. 50, no. 24, pp. 17953–17979, 1994.

[65] Reuter, K. and Scheffler, M., "Composition , structure , and stability of Ruthenium dioxide

(110) as a function of oxygen pressure," *Physical Review B*, vol. 65, no. July, pp. 1–11, 2001.

[66] Fisher, G. and Sexton, B., "Identification of an adsorbed hydroxyl species on the Pt(111) surface," *Physical Review Letters*, vol. 44, no. 10, pp. 683–686, 1980.

[67] Swart, J. C. W., Van Helden, P., and Van Steen, E., "Surface energy estimation of catalytically relevant fcc transition metals using DFT calculations on nanorods," *Journal of Physical Chemistry C*, vol. 111, no. 13, pp. 4998–5005, 2007.

[68] Hirano, T., *In: MOPAC Manual*, 7 edition. Stewart, J. J. P., ed, 1993.

[69] Sandler, S. I., *Chemical, biochemical, and engineering thermodynamics*, 4th editio. Delaware: John Wiley & Sons, Inc., 2006.

[70] Fernández-ramos, A., Ellingson, B. A., Meana-Pañeda, R., Marques, R. M. J. M. C., and Truhlar, D. G., "Symmetry numbers and chemical reaction rates," *Theoretical Chemistry Account*, vol. 118, pp. 813–826, 2007.

[71] Hill, T. L., *An Introduction to Statistical Thermodynamics*, Dover. New York: Dover Publications, Inc., 1986.

[72] Campbell, C. T. and Sprowl, L. H., "Equilibrium constants and rate constants for adsorbates : two- dimensional (2D) ideal gas , 2D ideal lattice gas , and ideal hindered translator models," *The Journal of Physical Chemistry C*, vol. 120, pp. 10283–10297, 2016.

[73] Sprowl, L. H. and Campbell, C. T., "Hindered translator and hindered rotor models for adsorbates : partition functions and entropies," *The Journal of Physical Chemistry C*, vol. 120, pp. 9719–9731, 2016.

[74] Sun, Q., Reuter, K., and Scheffler, M., "Effect of a humid environment on the surface structure of Ruthenium oxide (110)," *Physical Review B*, no. 67, pp. 1–7, 2003.

[75] Margenau, H., "Van der Waals forces," *Reviews of Modern Physics*, vol. 11, no. I, pp. 1–35, 1939.

[76] Dalgarno, A. and Kingston, A. E., *Van der Waals Forces*. Belfast: Queen's University of Belfast, 1958.

[77] Silberberg, M. S., *Chemistry: The molecular nature of matter and change*, 5th ed. New York: McGraw-Hill, 2009.

[78] Grimme, S., "Semiempirical GGA-type density functional constructed with a long-range dispersion correction," *Journal of computational chemistry*, vol. 27, no. 15, pp. 1787–1799, 2006.

[79] Zhao, Y. and Truhlar, D. G., "Hybrid meta density functional theory methods for thermochemistry , thermochemical kinetics , and noncovalent interactions : The MPW1B95 and MPWB1K models and comparative assessments for hydrogen bonding and van der Waals interactions," *J. Phys. Chem. A*, vol. 108, pp. 6908–6918, 2004.

[80] Grimme, S., Ehrlich, S., and Goerigk, L., "Effect of the damping function in dispersion corrected density functional theory," *Journal of Computational Chemistry*, vol. 32, no. 7, pp. 1456–1465, 2011.

[81] Becke, A. D., "Density-functional thermochemistry. V. Systematic optimization of exchange-correlation functionals," *The Journal of Chemical Physics*, vol. 107, no. 8554, 1997.

[82] Becke, A. D. and Johnson, E. R., "A density-functional model of the dispersion interaction," *Journal of Chemical Physics*, vol. 123, no. 15, 2005.

[83] Jurečka, P., Šponer, J., Černý, J., and Hobza, P., “Benchmark database of accurate (MP2 and CCSD(T) complete basis set limit) interaction energies of small model complexes, DNA base pairs, and amino acid pairs,” *Phys. Chem. Chem. Phys.*, vol. 8, no. 17, pp. 1985–1993, 2006.

[84] Pack, J. D. and Monkhorst, H. J., “Special points for Brillouin-zone integrations,” *Physical Review B*, vol. 16, no. 4, pp. 1748–1749, 1977.

[85] Gambu, T., “A DFT study of the interaction of O with Pt nanorod edge sites: A model for the ORR activity on Pt nanoparticle edges,” MSc thesis, UCT, 2015.

[86] Haynes, W. M., Lide, D. R., and Bruno, T. J., *CRC Handbook of Chemistry and Physics*, 94 edition. CRC Press, 2013.

[87] Shubina, T. E., Hartnig, C., and Koper, M. T. M., “Density functional theory study of the oxidation of CO by OH on Au(110) and Pt(111) surface,” *Phys.Chem.Chem.Phys.*, vol. 6, no. 110, pp. 4215–4221, 2004.

A. APPENDIX – INITIAL GEOMETRIES FOR PT(111)

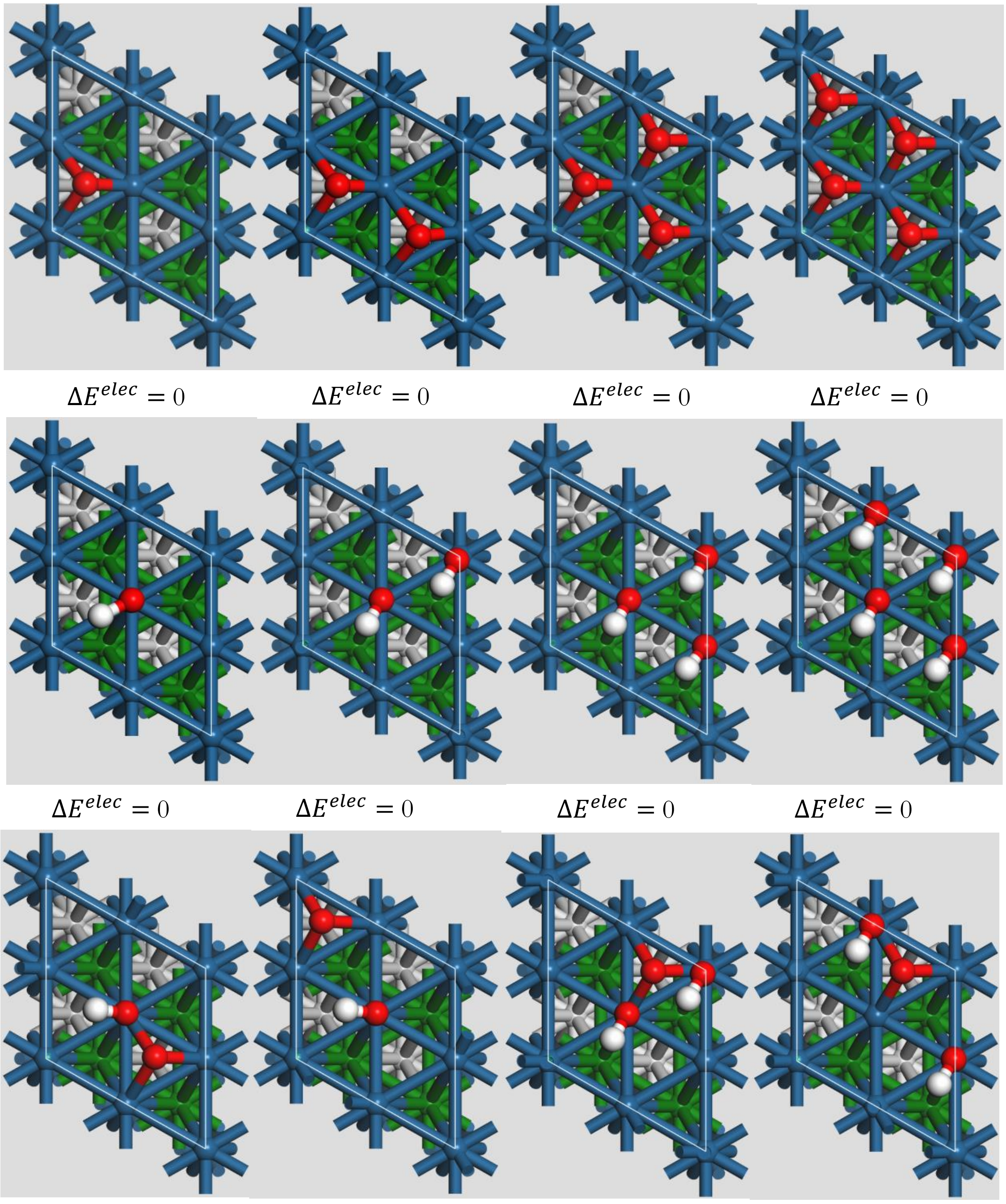

$\Delta E^{elec} = 0$ $\Delta E^{elec} = 0$ $\Delta E^{elec} = 0$ $\Delta E^{elec} = 0$

$\Delta E^{elec} = 0$ $\Delta E^{elec} = 0$ $\Delta E^{elec} = 0$ $\Delta E^{elec} = 0$

$\Delta E^{elec} = 0.53$ eV $\Delta E^{elec} = 0$ $\Delta E^{elec} = 0$ $\Delta E^{elec} = 0.64$ eV

Figure A-1: Geometries tested on Pt(111) for determining the optimized coverages with the final E^{elec} deviation from the lowest energy configuration (LEC) reported as $\Delta E^{elec} = E^{elec} - E^{elec}_{LEC}$.

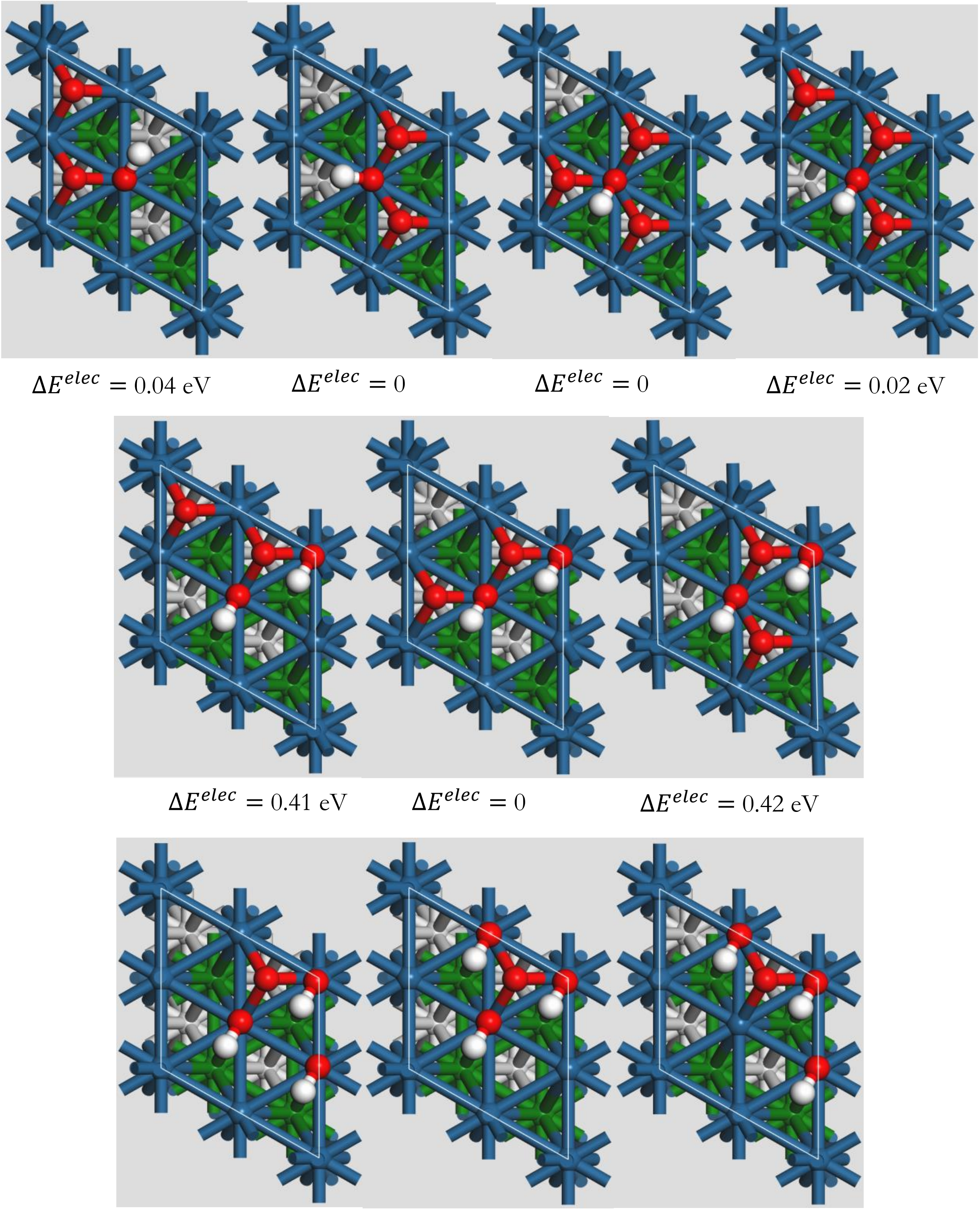

$\Delta E^{elec} = 0.04$ eV $\Delta E^{elec} = 0$ $\Delta E^{elec} = 0$ $\Delta E^{elec} = 0.02$ eV

$\Delta E^{elec} = 0.41$ eV $\Delta E^{elec} = 0$ $\Delta E^{elec} = 0.42$ eV

$\Delta E^{elec} = 0.46$ eV $\Delta E^{elec} = 0$ $\Delta E^{elec} = 0.37$ eV

Figure A-2: Geometries tested on Pt(111) for determining the optimized coverages and ΔE^{elec} continued.

B. APPENDIX – INITIAL GEOMETRIES FOR PT(100)

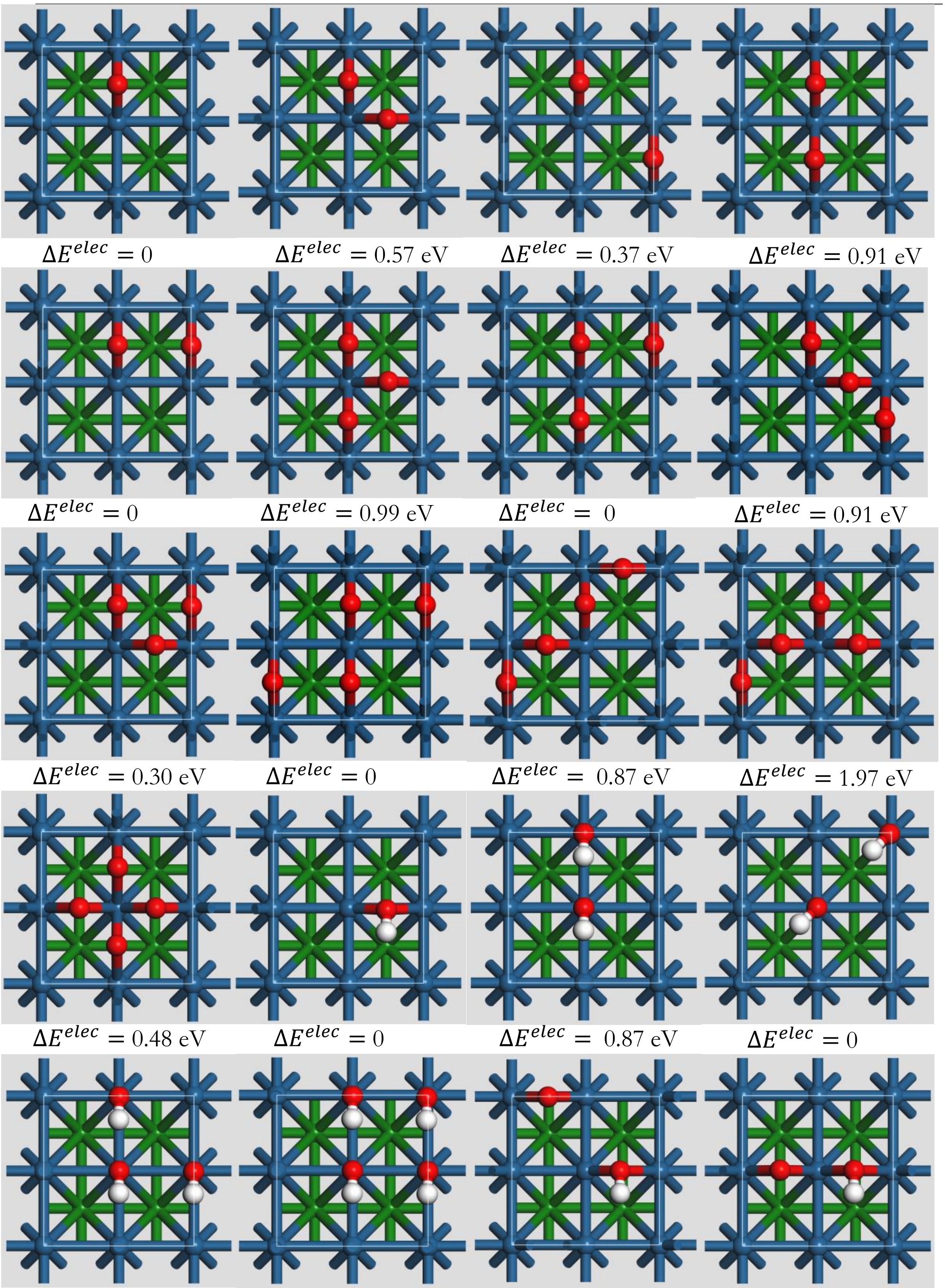

$\Delta E^{elec} = 0$ $\Delta E^{elec} = 0.57$ eV $\Delta E^{elec} = 0.37$ eV $\Delta E^{elec} = 0.91$ eV

$\Delta E^{elec} = 0$ $\Delta E^{elec} = 0.99$ eV $\Delta E^{elec} = 0$ $\Delta E^{elec} = 0.91$ eV

$\Delta E^{elec} = 0.30$ eV $\Delta E^{elec} = 0$ $\Delta E^{elec} = 0.87$ eV $\Delta E^{elec} = 1.97$ eV

$\Delta E^{elec} = 0.48$ eV $\Delta E^{elec} = 0$ $\Delta E^{elec} = 0.87$ eV $\Delta E^{elec} = 0$

$\Delta E^{elec} = 0$ $\Delta E^{elec} = 0$ $\Delta E^{elec} = 0.38$ eV $\Delta E^{elec} = 1.08$ eV

Figure B-1: Geometries tested on Pt(100) for determining the optimized coverages with the final E^{elec} deviation reported as $\Delta E^{elec} = E^{elec} - E^{elec}_{LEC}$.

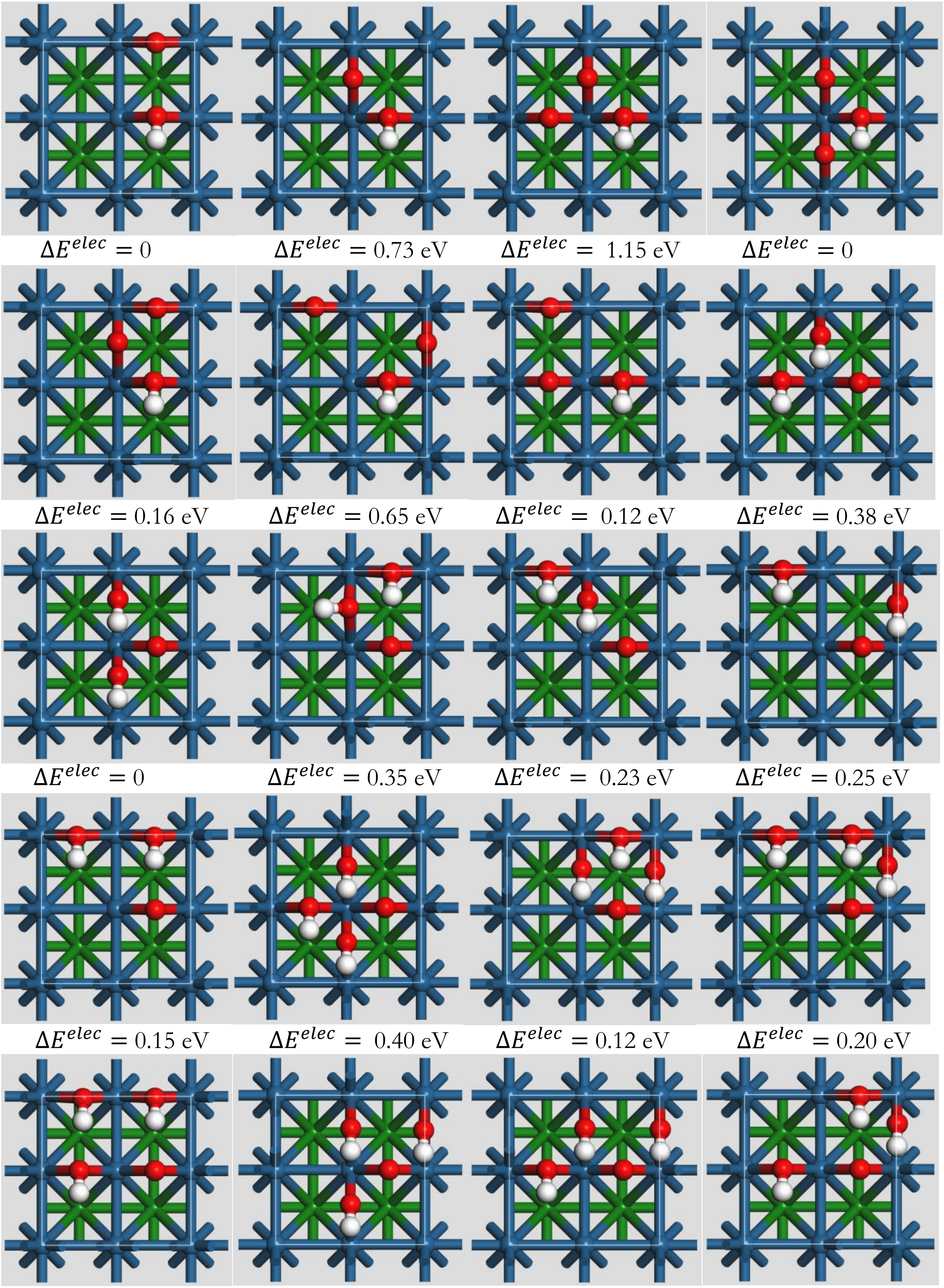

$\Delta E^{elec} = 0$ $\Delta E^{elec} = 0.73$ eV $\Delta E^{elec} = 1.15$ eV $\Delta E^{elec} = 0$

$\Delta E^{elec} = 0.16$ eV $\Delta E^{elec} = 0.65$ eV $\Delta E^{elec} = 0.12$ eV $\Delta E^{elec} = 0.38$ eV

$\Delta E^{elec} = 0$ $\Delta E^{elec} = 0.35$ eV $\Delta E^{elec} = 0.23$ eV $\Delta E^{elec} = 0.25$ eV

$\Delta E^{elec} = 0.15$ eV $\Delta E^{elec} = 0.40$ eV $\Delta E^{elec} = 0.12$ eV $\Delta E^{elec} = 0.20$ eV

$\Delta E^{elec} = 0.04$ eV $\Delta E^{elec} = 0.90$ eV $\Delta E^{elec} = 0.04$ eV $\Delta E^{elec} = 0$

Figure B-2: Geometries tested on Pt(100) for determining the optimized coverages and ΔE^{elec} continued.

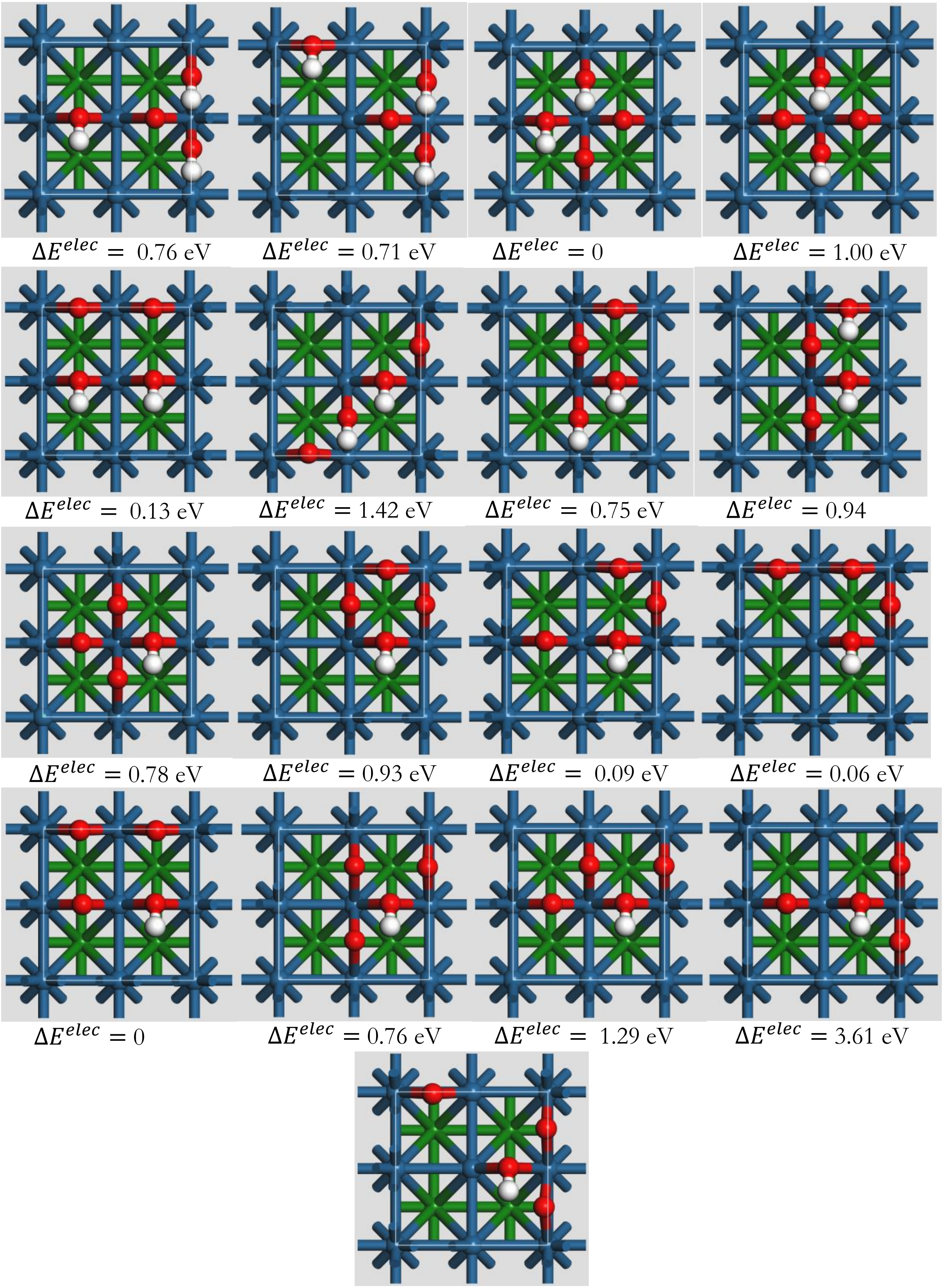

$\Delta E^{elec} =$ 0.76 eV $\Delta E^{elec} =$ 0.71 eV $\Delta E^{elec} = 0$ $\Delta E^{elec} =$ 1.00 eV

$\Delta E^{elec} =$ 0.13 eV $\Delta E^{elec} =$ 1.42 eV $\Delta E^{elec} =$ 0.75 eV $\Delta E^{elec} =$ 0.94

$\Delta E^{elec} =$ 0.78 eV $\Delta E^{elec} =$ 0.93 eV $\Delta E^{elec} =$ 0.09 eV $\Delta E^{elec} =$ 0.06 eV

$\Delta E^{elec} = 0$ $\Delta E^{elec} =$ 0.76 eV $\Delta E^{elec} =$ 1.29 eV $\Delta E^{elec} =$ 3.61 eV

$\Delta E^{elec} =$ 1.24 eV

Figure B-3: Geometries tested on Pt(100) for determining the optimized coverages and ΔE^{elec} continued.

C. APPENDIX – ELECTRONIC ENERGY AND VIBRATIONS

Table C-1: Electronic energy for the 14 lowest energy configurations for Pt(111) and Pt(100) using the PAW-PBE model.

Coverage [ML]	Adsorbates	$E^{elec}_{Pt(111)+adsorbate}$ [eV]	$E^{elec}_{Pt(100)+adsorbate}$ [eV]
0	Clean	-116.0087	-113.8804
0.25	O	-122.0994	-119.9616
	OH	-125.9800	-124.4349
0.50	2O	-127.6188	-126.1298
	2OH	-136.3662	-135.2776
	O/OH	-132.0742	-130.8636
0.75	3O	-132.3093	-131.2448
	3OH	-146.4129	-145.1595
	2O/OH	-136.9437	-136.0436
	O/2OH	-141.7415	-140.6156
1.00	4O	-136.2441	-136.3891
	4OH	-156.7273	-154.7010
	O/3OH	-151.3257	-150.4966
	2O/2OH	-146.4470	-146.1467
	3O/OH	-141.5359	-141.3469

Table C-2: Electronic energy and vibrations for O_2 and H_2O in the gas phase using the PAW-PBE model.

Energy [eV]		
	O_2	H_2O
	-9.8350	-13.8817

Vibrations [cm^{-1}]		
	O_2	H_2O
1	1565	3818
2		3699
3		1579

Table C-3: Vibrations [cm^{-1}] of the lowest energy configurations for single adsorbate species adsorption on Pt(111) using the PAW-PBE model.

	Adsorbates present on Pt(111)-p(2x2)							
Vibration No:	O	2O	3O	4O	OH	2OH	3OH	4OH
1	450	483	488	495	3644	3402	3503	3170
2	370	474	478	426	920	3389	3273	3165
3	369	430	445	426	518	1122	3250	3165
4		420	444	425	156	1042	1140	3140
5		396	425	411	107	601	1099	1183
6		380	425	410	81	530	1057	1149
7			385	409		513	725	1147
8			385	361		398	542	1137
9			365	360		243	527	725
10				359		136	525	716
11				302		86	492	690
12				299		73	369	542
13							313	513
14							219	513
15							162	510
16							148	474
17							127	308
18							113	291
19								290
20								235
21								221
22								219
23								164
24								162

Table C-4: Vibrations [cm^{-1}] of the lowest energy configurations for co-adsorbate species adsorption on Pt(111) using the PAW-PBE model.

	Adsorbates present on Pt(111)-p(2x2)					
Vibration No:	O/OH	2O/OH	O/2OH	O/3OH	2O/2OH	3O/OH
1	3649	3624	3469	3395	3415	3300
2	926	1025	3324	2524	3390	1408
3	517	530	1160	2333	1175	941
4	454	482	1083	1610	1100	610
5	375	454	566	1194	533	494
6	370	429	531	1099	513	471
7	152	404	519	1005	505	438
8	137	393	504	862	491	432
9	120	355	411	584	485	398
10		203	386	550	459	386
11		124	377	522	427	341
12		62	267	496	416	239
13			185	460	404	148
14			114	443	306	101
15			64	421	273	61
16				363	152	
17				326	132	
18				293	123	
19				239		
20				158		
21				136		

Table C-5: Vibrations [cm^{-1}] of the lowest energy configurations for single adsorbate species adsorption on Pt(100) using the PAW-PBE model.

	Adsorbates present on Pt(100)-p(2x2)							
Vibration No:	O	2O	3O	4O	OH	2OH	3OH	4OH
1	377	525	607	609	3648	3441	3558	3389
2	216	519	564	600	896	3411	3342	3383
3	173	480	526	572	533	953	3159	3374
4		474	521	568	147	940	1080	3373
5		231	492	527	88	891	1004	1108
6		171	480	520	39	822	966	1082
7			228	492		403	894	1024
8			167	491		399	600	1006
9			137	212		315	534	660
10				205		311	481	548
11				176		224	468	545
12				171		176	427	534
13							329	516
14							220	511
15							210	454
16							141	290
17							112	230
18							94	221
19								218
20								215
21								152
22								140
23								134
24								125

Table C-6: Vibrations [cm^{-1}] of the lowest energy configurations for co-adsorbate species adsorption on Pt(100) using the PAW-PBE model.

	Adsorbates present on Pt(100)-p(2x2)					
Vibration No:	O/OH	2O/OH	O/2OH	O/3OH	2O/2OH	3O/OH
1	2730	2452	3415	3789	2705	2500
2	1129	1190	2071	3412	2695	1190
3	1016	1074	1252	2426	1141	1102
4	490	590	1120	1573	1139	593
5	449	552	921	1188	1072	577
6	445	500	891	1081	1063	559
7	370	488	494	627	547	556
8	258	461	476	578	532	501
9	212	373	428	547	528	485
10		254	407	494	526	463
11		198	395	487	455	421
12		136	325	466	443	258
13			290	383	411	207
14			236	313	409	186
15			218	277	283	177
16				254	254	
17				221	190	
18				194	173	
19				101		
20				89		
21				85		

EBE Faculty: Assessment of Ethics in Research Projects

Any person planning to undertake research in the Faculty of Engineering and the Built Environment at the University of Cape Town is required to complete this form before collecting or analysing data. When completed it should be submitted to the supervisor (where applicable) and from there to the Head of Department. If any of the questions below have been answered YES, and the applicant is NOT a fourth year student, the Head should forward this form for approval by the Faculty EIR committee: submit to Ms Zakiya Chikte (Zakiya.chikte@uct.ac.za); New EBE Building, Ph 021 650 5739).

Please note – It is important to keep a signed copy of this form as students must include a copy of the completed form with the dissertation/thesis when it is submitted for examination.

Name of Principal Researcher/Student: PIERRE CILLIERS **Department:** CHEMICAL ENGINEERING

If a Student: **Degree:** MASTERS IN CHEMICAL ENGINEERING **Supervisor:** ERIC VAN STEEN

If a Research Contract indicate source of funding/sponsorship:

Research Project Title: LATERAL INTERACTIONS OF O-CONTAINING SPECIES ON Pt SURFACES
→CHANGED TO: PHASE DIAGRAM FOR THE CO-ADSORPTION OF O AND OH ON Pt(100) AND Pt(111)

Overview of ethics issues in your research project:

Question 1: Is there a possibility that your research could cause harm to a third party (i.e. a person not involved in your project)?	YES	NO ✓
Question 2: Is your research making use of human subjects as sources of data? If your answer is YES, please complete Addendum 2.	YES	NO ✓
Question 3: Does your research involve the participation of or provision of services to communities? If your answer is YES, please complete Addendum 3.	YES	NO ✓
Question 4: If your research is sponsored, is there any potential for conflicts of interest? If your answer is YES, please complete Addendum 4.	YES	NO ✓

If you have answered YES to any of the above questions, please append a copy of your research proposal, as well as any interview schedules or questionnaires (Addendum 1) and please complete further addenda as appropriate.

I hereby undertake to carry out my research in such a way that

- there is no apparent legal objection to the nature or the method of research; and
- the research will not compromise staff or students or the other responsibilities of the University;
- the stated objective will be achieved, and the findings will have a high degree of validity;
- limitations and alternative interpretations will be considered;
- the findings could be subject to peer review and publicly available; and
- I will comply with the conventions of copyright and avoid any practice that would constitute plagiarism.

Signed by:

	Full name and signature	Date
Principal Researcher/Student:	PIERRE CILLIERS Signed	8-5-2017

This application is approved by:

Supervisor (if applicable):		3·5·17
HOD (or delegated nominee): Final authority for all assessments with NO to all questions and for all undergraduate research.		8-5-2017
Chair : Faculty EIR Committee For applicants other than undergraduate students who have answered YES to any of the above questions.		